UNIVERSITY OF
CAMBRIDGE

Magnetic structures and proximity effects in rare-earth/transition metal ferromagnetic and superconductor systems

T. D. C. Higgs
Queens' College

Dissertation submitted for the
degree of *Doctor of Philosophy*

December 2017

Abstract

The antiferromagnetic coupling between a rare-earth (RE) and a transition metal (TM) ferromagnet can be exploited to engineer normal state and superconducting functional devices. RE/TM ferromagnetic multilayers were previously used as spin-mixers to generate spin-triplet supercurrents. This was possible due to magnetic inhomogeneity present in the devices, however the precise nature of the inhomogeneity was not understood. Here we present a comprehensive study of the Ni/Gd/Ni system using a powerful element-specific measurement technique: x-ray magnetic circular dichroism. In order to analyse the experimental results we present a novel model based on the Stoner-Wohlfarth model, which shows that significant inhomogeneity exists at the Ni/Gd interfaces due to the competition between the exchange energies within the system and the Zeeman energy of the applied magnetic field. The experiment and model together provide a complete overview of the Ni/Gd/Ni system due to the breadth of temperatures and thicknesses studied. The knowledge gained from this work is then applied to designing and testing new spin valves based on the intrinsic inhomogeneity at the RE/TM interface, and both Ni/Gd- and Gd/Ho-based devices show reversible magnetic switching behaviour which alters the superconducting critical temperature.

This dissertation is the result of my own work and includes nothing which is the outcome of work done in collaboration except as declared in the Preface and specified in the text.

It is not substantially the same as any that I have submitted, or, is being concurrently submitted for a degree or diploma or other qualification at the University of Cambridge or any other University or similar institution except as declared in the Preface and specified in the text. I further state that no substantial part of my dissertation has already been submitted, or, is being concurrently submitted for any such degree, diploma or other qualification at the University of Cambridge or any other University or similar institution except as declared in the Preface and specified in the text.

It does not exceed the prescribed word limit for the relevant Degree Committee.

Some important results in this thesis have been published as the following:

- **T. D. C. Higgs**, S. Bonetti, H. Ohldag, N. Banerjee, X. L. Wang, A. J. Rosenberg, Z. Cai, J. H. Zhao, K. A. Moler, and J. W. A. Robinson. *Magnetic coupling at rare earth ferromagnet/transition metal ferromagnet interfaces: A comprehensive study of Gd/Ni.* Scientific Reports, **6** (30092), 2016.

Acknowledgements

First and foremost I would like to thank Jason Robinson, my supervisor, for taking me on and allowing me to work on such interesting projects. The whole experience has been fantastic and I have learnt so much from it, but none of it would have been possible without the help of a large amount of people, and the EPSRC, who provided my funding. For scientific and practical help across all of the work I did, Niladri Banerjee gets special thanks. Hendrik Ohldag and Stefano Bonetti were instrumental in collecting and interpreting the XMCD data and initiating work on the model. Hendrik especially for training me at SLAC, and supervising my visits there. Without him a large part of this work would not have been possible. Speaking of which, Nadia Stelmashenko also deserves huge thanks for her work in the lab. Not only did she teach me a lot about the workings of a lot of the lab equipment, but she is also vital to most of its operation.

As collaborators, Xiaolei Wang, Kathryn Moler and Aaron Rosenberg were extremely helpful, often contributing far more than we could have hoped for.

Back in the device materials group, David Gustafsson, Prasanta Muduli, Yuanzhou Gu and others deserve thanks for training me on the equipment for which they were each responsible, and the time they invested to keep that equipment operational for everyone. I would also like to thank the undergraduate and Masters students who came to work with me, as well as Jason for giving me the opportunity to supervise them. James (John's Devine-Stoneman!) deserves a mention for being the first of these students, as well as giving us something to talk about at tea time non-stop for several years (University Challenge). As did James, Anand also deserves recognition for choosing to stay with the group despite having first encountered it under my watch. Deserving or not, I'll gladly take credit for that. Still on students, we won't forget Kit, if for nothing else than for being Dutch but still having a bike-based bust up with a pesky bollard. What we'll really remember him for was getting fully involved in the group while he was here. What we'll try to forget him for was thrashing us all at squash. Cai and Patrik were also excellent students, fully applying themselves while they were here.

Still in the DMG, special mentions go to everyone who made it a friendly place to be. And particularly special mentions go to everyone in the pub quiz team. These groups include Dave, Sam, Mario, John, Juliet, Anand, Carla, Mike, Yi, Bence, Chess, Enric, Guillaume, and many others. And last but not least, Ravi and Lana. Where would we be without Ravi's story-telling skills, or Lana's resilience in the face of Southern discrimination. Even if that was mostly my fault.

Outside of work, where would I be without my family, tolerating my determination to hang on to being a student for eight years. Particularly my parents for always supporting me, and doing everything they can to help.

Finally, I must thank the person who has been most involved in the whole of time it has taken me to complete this work: Kelsey. Only the best of people would have made the number of concessions she has during my time as a student. Without her supporting me the whole way the journey would have been much more difficult, and not nearly as much fun.

Contents

List of Figures

Part I

Introduction and motivation

Chapter 1

Introduction

Ferromagnetism and superconductivity are both quantum mechanical effects built around electrons, crystal lattices, and the interactions between them. While ferromagnetism has been studied since antiquity (with varying degrees of success), no naturally occurring elements or minerals exhibit superconductivity near room temperature, so they have only been able to be studied since their discovery just over a century ago. However, rare-earth ferromagnets proved difficult to study for most of history due to their high reactivity and strong tendency to alloy with other materials. Interest has remained high since the 1970s due to their high permanent magnetic moments, and in some cases their unusual intrinsic magnetic structures.

Due to the different origins of the ferromagnetism in the transition metals (TMs) and the rare-earths (REs), when a TM ferromagnet is joined to an RE ferromagnet, the result is not just one bigger ferromagnet - at least not in the case of thin films. The two ferromagnets couple antiparallel to one another at the interface, and this antiparallel coupling in the midst of the parallel coupling in the rest of the sample causes a surprising array of inhomogeneous magnetic textures.

The main two ferromagnets studied in this research are Ni, a transition metal, and Gd, a rare-earth metal*.

Gd, atomic number 64, was discovered by Jean Charles Galissard de Marignac, a Swiss chemist, in 1880. It is named after the Finnish geologist and chemist Johan Gadolin, via the mineral gadolinite. At 293 K (20 °C), Gd has the highest Curie temperature of any of the rare-earths. Its permanent magnetic moment is 7.98 μ_B†, thirteen times that of Ni. It has a melting point of 1312 °C, a density of 7.90 g cm^{-3}, and an hcp crystal structure at room temperature.

Ni, atomic number 28, has been used in alloys for thousands of years, albeit unknowingly. The name comes from medieval German miners blaming a mythological sprite, Nickel, for their being unable to extract copper from what they thought was copper ore. Nickel has the lowest Curie temperature of the transition metal ferromagnets, at 627 K (354 °C), and a melting point of 1728 K. Its permanent magnetic moment is 0.606 μ_B, thirteen times less that of Gd. It has a density of 8.91 g cm^{-3} and an fcc crystal structure.

Superconductivity, by contrast, has not been known about for thousands of years. The only naturally occurring place within reach of humans where temperatures are low enough for elemental superconductors to superconduct, space, is notoriously difficult to get to. Consensus was easily reached in the academic community that it

* Characteristics of other elements studied are given at the end of the section.

† μ_B: Bohr magneton. Defined as $\frac{e\hbar}{2m_e}$.

is easier to bring the cold inside. For the last few centuries, the coldest places on Earth have been inside laboratories.

Since conventional superconductivity relies on a coupling of electrons with antiparallel spin, ferromagnetism was thought to be incompatible with superconductivity. The exchange field of the ferromagnet would break the pair apart because of the electron which had spin opposite to the direction of the exchange field. However, theory and experiments showed that unconventional Cooper pairs with parallel spin could be generated by magnetic textures, and these pairs can penetrate the ferromagnet analogously to the conventional Cooper pairs which penetrate normal metals.

In 2012, Robinson *et al.* showed that the critical current in a Nb/Ni/Gd/Ni/Nb Josephson junction depended on the magnetic configuration of the junction layers, and concluded that some form of magnetic inhomogeneity was acting as a spin-mixer to convert spin-singlet Coopers pairs into spin-triplet pairs. Although the group had a working theory on the structure of the Ni/Gd/Ni stack it is difficult to determine the exact configuration of the multilayered structure from bulk magnetometry alone. Understanding in detail the magnetic configuration of this stack was a main motivation of the research presented here, as well as finding out whether the new knowledge about the system could be used to design and make more effective superconducting spin valves.

We were extremely fortunate to have access to a synchrotron which generates a high enough flux of x-rays to study the magnetic state of the stack, and study each element individually. Only one other group has used an element-specific technique to study the Ni/Gd system (Barth *et al.*), but they only studied one sample. Our results are consistent with theirs, but also extremely comprehensive.

The other materials used in this research were Nb and Ho. Ho, atomic number 67, is named after the Latin name for Stockholm, *Holmia*, the birthplace of one of the discoverers. It has a melting point of 1734 K, a density of 8.79 g cm^{-3}, and an hcp cubic structure. As discussed in more detail in Sec. 7.3.1, the magnetic structure evolves with cooling in zero magnetic field. Above 133 K it is paramagnetic, and is a helical antiferromagnet below. Cooled further to 20 K, the helix structure cants out of plane by 10°. The permanent magnetic moment of holmium is 10.6 μ_B, the highest of any naturally occurring element.[1]

Nb, atomic number 41, was originally named columbium, after Columbia, an historical name for the United States, but after confusion with columbite's similarity to tantalite, was named after one of the children of Tantalus, Niobe. It has a melting point of 2750 K, a density of 8.79 g cm^{-3}, and a bcc crystal structure. It is a Type II superconductor, and has the highest critical temperature of all the elemental superconductors at 9.2 K.

1.1 Overview

This thesis is structured as follows. First, the relevant background knowledge and theory is presented. Chapter 2 covers magnetism, ferromagnetism in particular, the differences between rare-earth ferromagnets and transition metal ferromagnets, and the interplay between the two when interfaced together. Chapter 3 includes superconductivity and the coexistence of ferromagnetism and superconductivity. In the next part, experimental results are presented. Chapter 4 describes the experimental methods used for growing and measuring the samples. In Chapter 5 the x-ray magnetic circular dichroism (XMCD) results obtained from the synchrotron are given in full. These results are analysed in Chapter 6, with the use of a novel and simple model. Chapter 7 presents the work done studying superconducting spin valves; partly using the Ni/Gd results from earlier chapters, but also using the intrinsic magnetic inhomogeneity of Ho in a Ho/Gd system. The final part is dedicated to concluding remarks, a summary, and suggestions for future work to continue from what we have learnt.

Part II

Theory

Chapter 2

Magnetism

2.1 Ferromagnetism

Despite the ancient origins of humans' study or utilisation of ferromagnetism (the use of lodestone as compasses in antiquity, for example), it was only with the advent of quantum mechanics in the early twentieth century that we could realise a detailed explanation of its microscopic origins, rather than simply being able to describe its effects.[2]

2.1.1 Magnetic moments

A classical picture of a magnetic dipole may be described as two magnetic charges with opposite signs, analogous to electric charges, separated by some distance, as shown in Fig. 2.1. The *magnetic moment* of such a dipole is defined as a vector pointing from the negative to the positive magnetic charge. The same effective magnetic moment may be imagined as a charged particle travelling in a closed orbit. The vector nature of the moment is derived from the classical angular momentum of the particle; the cross product of the linear velocity and the radius of the orbit. In the case of an electron, its negative charge changes the sign of the magnetic moment so that the moment points in the opposite direction to the classical angular momentum.[3]

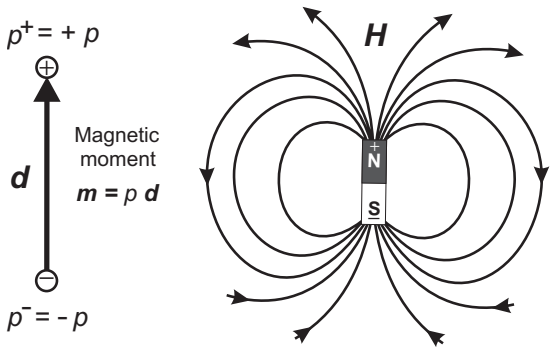

Figure 2.1: Classical definition of a magnetic dipole (left): Two magnetic charges p separated by a distance **d**. Right: the external field produced by N and S poles of a magnet, analogous to the magnetic charges. From Ref. 2.

2.1.2 Dipolar interaction

Although these classical ideas of magnetic dipole moments are useful for visualising individual moments, and how a moment would behave in an externally applied magnetic field, we push them past the boundaries of usefulness when we try to use them to explain long range ferromagnetic ordering.

To begin with, we know that opposites attract, so neighbouring dipoles will naturally align with their respective magnetic moments antiparallel to one another; one north pole would prefer to be near the other south pole, and vice versa. Picturing a large grid of these dipoles, we would obtain alternating north/south poles with half of all the moments pointing in the opposite direction to the other half. This is not consistent with ferromagnetic ordering.

We can also calculate the energy involved in the interaction between two neighbouring dipoles, and if we assume two electrons separated by a distance on the order of tenths of nanometres, the resultant energy corresponds to a temperature (by $E = k_B T$) on the order of 1 K. This implies that at temperatures above 1 K, thermal fluctuations are strong enough to overcome the dipole-dipole interaction, and we would not expect to see long-range order. However, common ferromagnets such as nickel and iron are ferromagnetic up to room temperature and far beyond, so we must seek another explanation for such ferromagnetism; the explanation will require a much stronger interaction.

2.1.3 Phenomenological models

Rather than trying to explain the microscopic origins of ferromagnetism, several theories can be used to describe the behaviour of ferromagnets. The emergence of ferromagnetic ordering with the lowering of temperature is a type of broken symmetry, and a second-order* phase transition, and was described by Ginzberg and Landau as such. According to Landau's theory of phase transitions some order parameter is associated with the phase transition, and in this case it is the magnetisation, **M**, a vector. The magnetisation goes to zero as a ferromagnet is warmed above its critical temperature, the Curie temperature, T_C.

In order to visualise the breaking of symmetry in this model, we can take the Helmholtz free energy of the system:[4]

$$F = E - TS, \tag{2.1}$$

where E is the internal energy of the ferromagnet, T is the temperature, and S is the entropy. We also utilise Weiss' model of the ferromagnet, a model which postulated that a mean field exists throughout the ferromagnet caused by the interaction between the permanent magnetic moment of the atoms. He called this the "molecular field", and so the total field within the ferromagnet would be the sum of this molecular field and any applied field:

$$B = B_0 + b \tag{2.2}$$

The internal energy of the system is given by

$$E = -\int B \mathrm{d}M. \tag{2.3}$$

*Although Cowan[4] argues that since hysteresis is a characteristic specific to *first-order* transitions, it is not easily decided whether the ferromagnetic phase transition is first- or second-order.

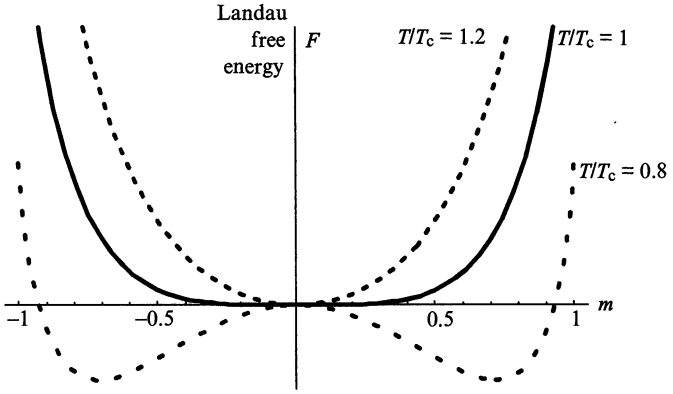

Figure 2.2: Above T_C the single minimum in the free energy is at $m = 0$. Below T_C there are two minima with finite magnetisations. Near T_C the magnetisation is free to move with little cost in energy. From Ref. 4.

The entropy is given by

$$S = -Nk \sum_j p_j \ln p_j \tag{2.4}$$

in which p_j are the probabilities of each of the states a single particle can occupy. For electrons, we assume the two spin states are simply $\pm 1/2$, and write these in terms of the reduced magnetisation, $m = M/M_0$:

$$p_\uparrow = \frac{1+m}{2} \quad \text{and} \quad p_\downarrow = \frac{1-m}{2} \tag{2.5}$$

Assembling the terms of the Helmholtz free energy we arrive at:

$$F = -\frac{Nk}{2} \left\{ T_C m^2 + T \left[2\ln 2 - (1+m)\ln(1+m) - (1-m)\,ln\,(1-m) \right] \right\} \tag{2.6}$$

Above the transition temperature this function has a single minimum at $m = 0$ (in the absence of an external field). As the temperature drops closer to the transition temperature this minimum flattens out and changes in magnetisation cost little energy. Below T_C however, the symmetry must be broken and the system will fall into one of two minima; the minima have equal and opposite magnetisations. Fig. 2.2 shows the emergence of the two minima as the temperature passes through and below T_C. If an external magnetic field is applied, one side of the function would be shifted up with respect to the other, removing this illusion of choice. This is shown in Fig. 2.3.

Because this symmetry breaking is *continuous*, the hysteretical nature of ferromagnetism remains unexplained by this model, but this is explained by the existence of magnetic domains instead. Of course, real-world magnetisations are not two-dimensional, and a real free energy function would extend into three dimensions in the shape of the bottom of a wine bottle, or Mexican hat, depending on one's preferred metaphor.[4]

2.1.4 Microscopic exchange interaction

The Weiss model of ferromagnetism (1907) was briefly mentioned in the previous section, and it was a successful phenomenological model, although it did not attempt to provide an explanation for the existence of the molecular field. Heisenberg

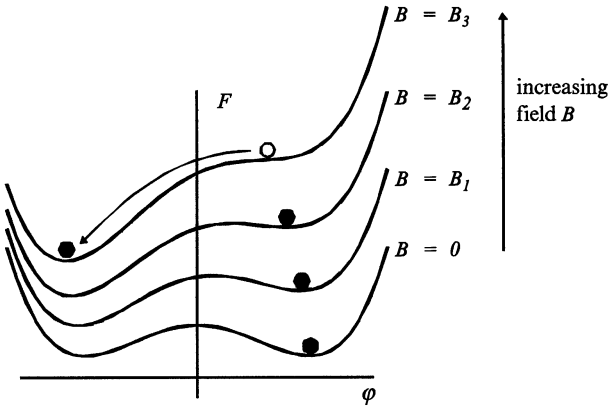

Figure 2.3: As the magnetic field of the system increases, the magnetisation aligned with the field direction is preferred and a global minimum for the system develops. From Ref. 4.

accounted for this in 1928 when he introduced the quantum mechanical exchange interaction between the spins of electrons. This exchange interaction fulfils our earlier criterion of a stronger interaction than the dipole interaction to explain ferromagnetism. It arises due to the identical nature of electrons, their half-integer spin, and the Coulomb repulsion between them.

The symmetrisation postulate for fermions states that if a particle system is antisymmetric under an exchange of any two particles, the particles are called fermions and have half-integer spins. This leads directly to the Pauli exclusion principle, which states that no two fermions can occupy the same quantum state.

We know that electrons are fermions with spin $\pm 1/2$, so a wavefunction describing a two-electron system must be antisymmetric, i.e. it must obey $\psi_a(\mathbf{r}_1)\psi_b(\mathbf{r}_2) = -\psi_a(\mathbf{r}_2)\psi_b(\mathbf{r}_1)$ for electrons $\psi_{a,b}$ at positions $\mathbf{r}_{1,2}$. Such a wavefunction will be made up of a spatial term and a spin term (χ), one of which must be antisymmetric in order for the total to be antisymmetric. In the spin singlet case (Ψ_S), the spin part of the wavefunction will be antisymmetric, so the spatial part will be symmetric, and vice versa in the triplet case (Ψ_T):

$$\Psi_S = \frac{1}{\sqrt{2}} \left(\psi_a(\mathbf{r}_1)\psi_b(\mathbf{r}_2) + \psi_a(\mathbf{r}_2)\psi_b(\mathbf{r}_1)\right) \chi_S \tag{2.7}$$

$$\Psi_T = \frac{1}{\sqrt{2}} \left(\psi_a(\mathbf{r}_1)\psi_b(\mathbf{r}_2) - \psi_a(\mathbf{r}_2)\psi_b(\mathbf{r}_1)\right) \chi_T. \tag{2.8}$$

These states have the following energies:

$$E_S = \int \Psi_S^* \mathcal{H} \Psi_S \mathrm{d}\mathbf{r}_1 \mathrm{d}\mathbf{r}_2 \tag{2.9}$$

$$E_T = \int \Psi_T^* \mathcal{H} \Psi_T \mathrm{d}\mathbf{r}_1 \mathrm{d}\mathbf{r}_2 \tag{2.10}$$

where $\mathcal{H}$ is a Hamiltonian, and * indicates a complex conjugate.

In the spin singlet state, the two electrons are closer to one another spatially so experience a stronger Coulomb repulsion, but the total energy of the state is lowered by the antiparallel spins of the electrons. In the spin triplet state, the

two electrons have the same spin, and by being spatially separated can lower the Coulomb repulsion and therefore the total energy of the state.

So in some instances, as a result of the Pauli exclusion principle and Coulomb repulsion, it can be energetically favourable for two neighbouring electrons to align their spins parallel to one another. Note that the exchange interaction acts only on the electrons' spin angular momentum and not their orbital angular momentum.

2.1.5 Stoner criterion

Despite the success of the previous models in predicting the behaviour of ferromagnets with respect to temperature and the phase transition, they face a contradiction in the form of the band structure of the transition metal ferromagnets. The magnetism in Ni, Co and Fe arises from the electrons in the $3d$ orbitals which are delocalised, and therefore difficult to explain with Heisenberg's assumptions of interacting neighbouring, localised moments. The explanations we have seen so far could not account for the values of the atomic magnetic moments in the transition metals which are not integer-multiples of the Bohr magneton.

In 1983 Stoner published the band magnetism model which considered the behaviour of electrons around the Fermi energy, which in Ni, Co and Fe is in the $3d$ band. Since the $3d$ bands are only partially filled, electrons are free to enter the more excited states within the band. Due to the exchange interaction, having half of the electrons in the band occupy one spin state with the rest in the opposite spin state may not be the lowest possible energy state. If the energy cost of having asymmetrically filled energy levels is more than offset by the exchange energy from having several parallel electron spins, then some electrons will, without the presence of an external magnetic field, asymmetrically occupy the available spin states.[5,6] With more electrons of one spin species than the other, a spontaneous magnetisation has emerged in the metal. A criterion for whether this will happen in a system can be constructed by considering the energies of electrons in each spin state:

$$E_{\uparrow}(\mathbf{k}) = E(\mathbf{k}) - \frac{J(n_{\uparrow} - n_{\downarrow})}{2N} \tag{2.11}$$

$$E_{\downarrow}(\mathbf{k}) = E(\mathbf{k}) + \frac{J(n_{\uparrow} - n_{\downarrow})}{2N} \tag{2.12}$$

where J is the energy gained if the electrons correlate with one another, N is the number of atoms, and $n_{\uparrow\downarrow}$ is the occupation of electrons in each spin state. The Stoner criterion, which tells us whether it is favourable for there to be an imbalance in spin state occupation, is given by:

$$1 - \frac{JV}{2N} D(\varepsilon_F) \geq 0 \tag{2.13}$$

where V is the volume, and $D(\varepsilon_F)$ is the density of states at the Fermi energy. Fig. 2.4 shows the splitting in the sub-bands of the density of states in a metal which satisfies the Stoner criterion.

2.1.6 Rare-earth magnetism

The rare-earth ferromagnets also do not have permanent atomic magnetic moments that are integer multiples of the Bohr magneton. Therefore rare-earth ferromagnetism is also not explained simply by the Heisenberg modification to the Weiss

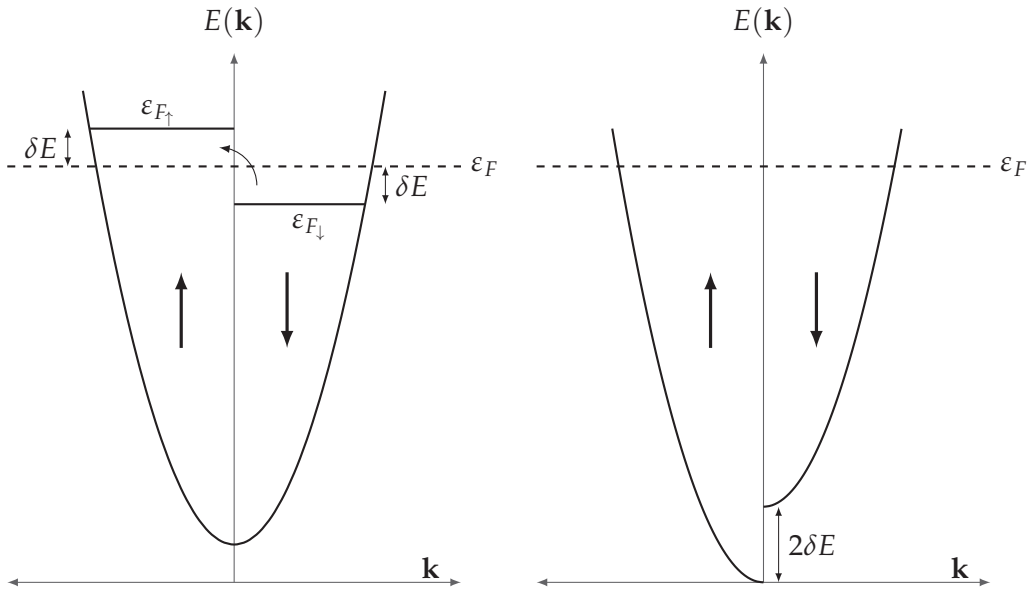

Figure 2.4: Left: Splitting of the sub-bands if the Stoner criterion is met and spontaneous magnetisation arises. Right: The incontinuity in the Fermi energy is resolved by a shift of $2\delta E$ in the minority spin sub-band. The net magnetisation direction will now be up, since the occupation of this sub-band is higher. Adapted from Ref. 7.

model. The electrons in the $4f$ orbitals are responsible for the ferromagnetism in the rare-earths, which goes some way to explaining why the atomic magnetic moments are so high (remember Gd's permanent moment is thirteen times that of Ni's). And these electrons are localised which does fit in with the idea of the neighbour-to-neighbour exchange interaction. However, the $4f$ orbitals are shielded by the outer orbitals in the rare-earths, so if there is an exchange interaction between the $4f$ electrons, it must be mediated somehow. Fig. 2.5 shows this shielding in Gd.

Indeed, the exchange interaction is mediated by the RKKY coupling mechanism, named for the primary scientists who developed the theory, Ruderman, Kittel, Kasuya and Yosida.[9–12] The premise of the theory is that a local moment polarises the nearby conduction electrons. This polarisation oscillates as a function of distance and can couple local moments together over relatively large distances, conveying the spin information of local moments to one another. In the case of the rare-earth ferromagnets, this indirect exchange information is carried by the $5d$ electrons, whose shell overlaps partly with that of the $4f$ electrons.[2] The RKKY interaction also explains the extra contribution to the observed permanent magnetic moment per atom of Gd. Armed with only the basic knowledge that the $4f$ electrons are responsible for the magnetism in Gd, we would think the moment should be $7\mu_B$ since there are 7 $4f$ electrons in a Gd atom. However, the observed value is $7.98\mu_B$, and we now can understand that this extra 10% is contributed by the conduction electrons which mediate the exchange interaction.[13] The RKKY interaction can be demonstrated relatively simply by growing a superlattice of rare-earth layers separated by a non-magnetic spacer. By varying the width of the spacer slightly, the whole superlattice will switch between ferromagnetic and antiferromagnetic coupling.

This oscillatory indirect exchange partially explains the variety of magnetic

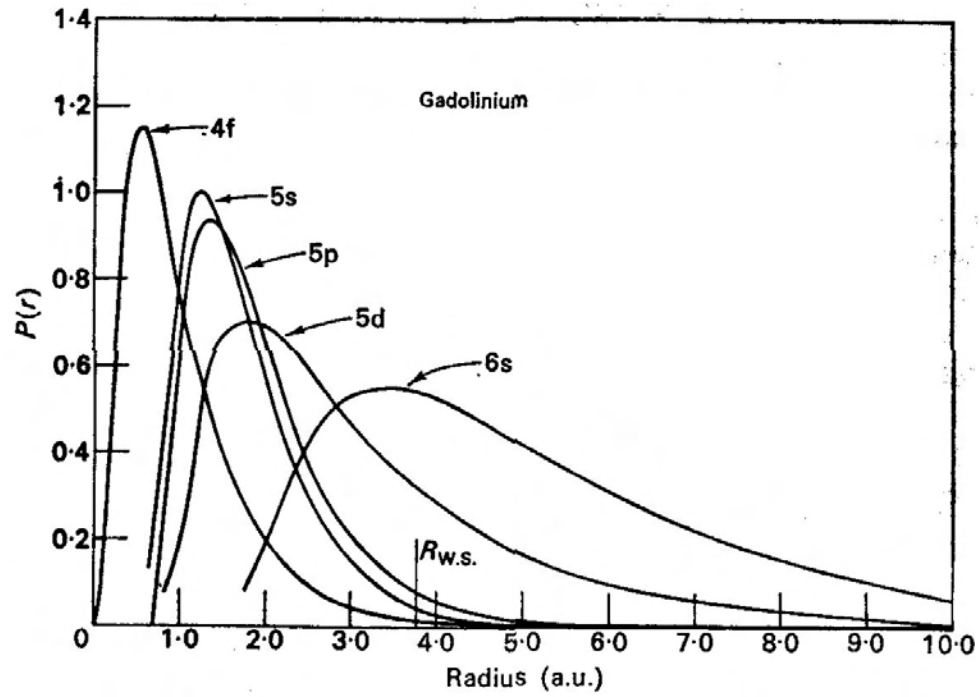

Figure 2.5: The $4f$ orbital in Gd is highly localised and shielded by the other orbitals. From Ref. 8.

textures seen in rare-earth ferromagnets, since slight differences in the separation between ions can lead to changing the sign of the polarisation, or lead to interference causing the conical or helical magnetic structures seen in Dy, Ho, Er and Tm.[14] However, these textures are also influenced by competition between the exchange term and the crystal field term in the Hamiltonian describing the system.[15] The exchange term is the only term which depends on the relative orientation of neighbouring spins, and the mismatch with the crystal field can lead to trigonal coupling, allowing the exchange interaction between nearest neighbours and next-nearest neighbours to rotate into directions away from the usual plane.[16,17] In Ho, neutron scattering experiments have shown that these crystal field mismatches "lock-in" to energetically favourable values before slipping suddenly to a new value as the temperature of the sample is cooled.[18–21] These results based on the crystal structure of Ho also show why only epitaxially grown samples display the conical and helical magnetic phases.

2.2 Antiferromagnetism

Antiferromagnetism is another form of long-range magnetic order, except rather than neighbouring magnetic moments in a lattice aligning *parallel* with one another (ferromagnetism), each moment aligns *antiparallel* to its neighbouring moments. As we saw in the introduction to the exchange interaction, while the interaction can allow two electrons to align their spins parallel and move further away from one another, the inverse is also true. So in some cases, neighbouring electrons will align antiparallel, and this ordering can extend throughout the whole material. The net magnetisation will be zero as each magnetic moment's contribution to the magnetisation is cancelled out by its neighbour.

2.3 Anisotropy

Magnetic anisotropy is the difference in measured magnetic properties of a sample when measured in different orientations or directions. Different characteristics of the sample can cause different forms of anisotropy, a few of which are discussed below.

Magnetocrystalline anisotropy: In materials with spin-orbit coupling, an applied magnetic field acting on the spin part of the angular momentum of an atom will also act on the orbital part. The orbital part is in turn coupled to the crystal lattice, so in order to rotate the spins to align with the field direction, this lattice bonding of the orbital angular momentum must be overcome. Due to this lattice coupling the resultant magnetocrystalline anisotropy will follow the same symmetry as that of the crystal structure.[22] Polycrystalline films should therefore have no overall crystalline anisotropy. In the Gd atom, the $4f$ shell is half-filled, so $L = 0$; Gd's spin-orbit contributions must therefore arise from the $5d$ shells.

Shape anisotropy: Within a sample which is magnetised by an external field, the internal field will point from the north pole to the south pole, while the external field points from south to north. This internal field which opposes the external *magnetising* field is called the *demagnetising* field. This demagnetising field makes it more difficult to magnetise a sample. In a long, thin sample, this demagnetising field will be stronger in the transverse than in the longitudinal directions, which means it will be easier to magnetise the sample in the longitudinal direction. This is another source of anisotropy, which is dependent on the shape of the sample.[22] In the long and thin sample, the anisotropy becomes stronger as the length-to-width ratio increases.

2.4 Domains

Each of the sources of anisotropy discussed above carries with it an associated energy which will contribute to the overall magnetic configuration of a system, along with the exchange energy and the magnetostatic energy. We can think of the magnetostatic energy in terms of the available work a ferromagnet can do on other magnetic materials around it; the stronger the external field and further from the sample the field lines reach, the more capacity for work on other materials there is, and by extension the more magnetostatic energy is being stored. In order to reduce this energy, the field lines can be "closed" within the sample by a reconfiguration of the moments into domains; regions within the sample that differ in their magnetisation direction.

This domain formation costs exchange energy at the domain walls because the moments have to differ from a strictly parallel coupling as the magnetisation changes from one direction to another across the wall. As usual, the formation of domains will only happen if it can lead to a net reduction in energy.

In the case of domains there will be a competition between the exchange energy and the magnetocrystalline anisotropy energy. The exchange energy is minimised if the domain wall is spread over a large distance to ensure minimal misalignment between neighbouring moments, while the anisotropy energy is minimised if all moments align with the easy axes.

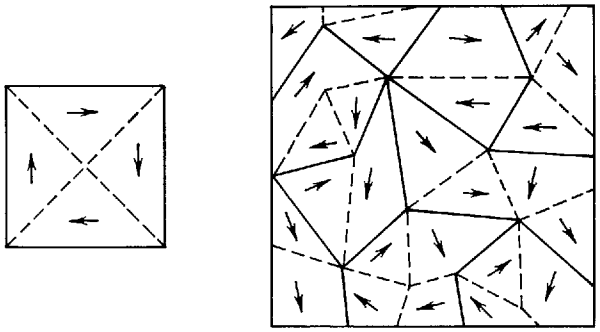

Figure 2.6: Left: A simple domain closure pattern in an ideal case. All domains are magnetised, although the net magnetisation of the sample is zero. Right: Typical domain patterns in a polycrystalline sample. From Ref. 5.

Fig. 2.6 shows domain closure in an ideal ferromagnet, as well as a more realistic layout of domains in a polycrystalline sample, where the randomly oriented crystal axes inhibit the same simple closure pattern as in the ideal case.

2.5 Response to an external field

Only after understanding domains can we understand the response of a conventional ferromagnet to an externally applied magnetic field. In the absence of an applied field a hypothetical lattice of magnetic moments forms domains to minimise the stray field and therefore the associated magnetostatic energy. When a field is applied to this sample, the magnetic moments can lower their associated Zeeman energy by aligning with the field direction. However the moments also try to minimise their exchange energy by aligning with their nearest neighbours. Those moments which are near a domain wall can lower their Zeeman energy with a small cost to their exchange energy by rotating slightly to become part of the wall. The moments on the other side of the wall are also rotating to align with their neighbours and the field and the net result is a shift in the position of the wall as a whole. The domain which aligns with the field has grown, and that which does not has shrunk.

This movement of domain walls and enlarging of favoured domains allows the whole sample to transition from having no net magnetisation to being saturated - all magnetic moments are aligned - in the presence of an external field.

If the external field direction is close to, but not parallel with, one of the easy axes of the sample, the moments will first all align with the easy axis; a higher field will be needed to force the moments away from that axis and to align parallel with the field.

In a perfect crystal, the domain walls are free to move with relative ease. However in a polycrystalline material, grain boundaries present obstacles to this free movement. Therefore, if we consider a polycrystalline sample which is saturated, magnetised completely in one direction, when a field is applied in the opposite direction there is a source of resistance to prevent all the domains easily rotating. A certain strength of the negative field is required to flip these domains. A hard ferromagnet is one which resists this negative field up to higher strengths, as opposed to a soft ferromagnet, whose magnetisations switch easily.

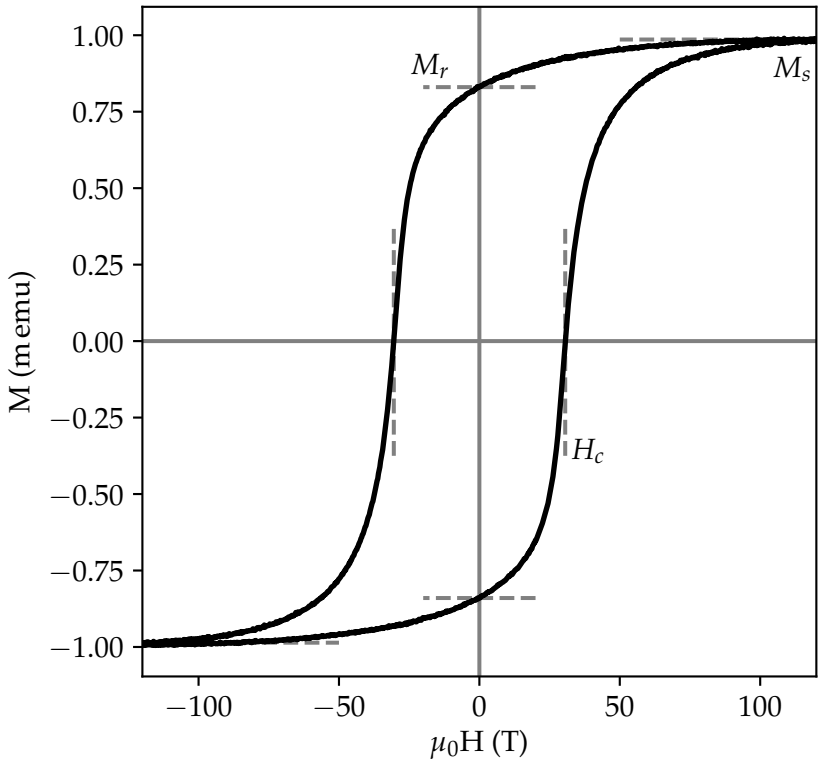

Figure 2.7: Response to a magnetic field of a 25 nm Fe film. At high applied field, all of the Ni moments are aligned with the applied field direction. The magnetisation is the saturation magnetisation, M_s. As the field strength is decreased, some relaxation of the moments occurs as they align with the easy axis. The magnetisation at zero applied field is the remanence magnetisation, M_r. As the applied field reverses direction it is now opposite to the magnetisation of most domains, and the moments begin to rotate. The field value at which the magnetisation drops to zero is the coercive field, H_c. As the field strength increases all the moments are eventually aligned to the field direction, but in the opposite direction from the start of the loop.

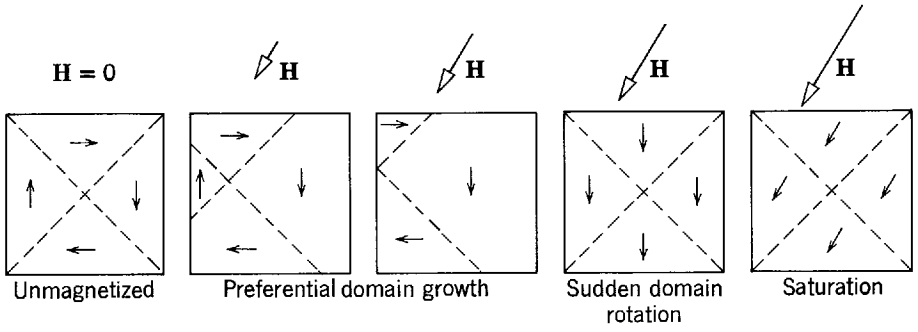

Figure 2.8: The growth and switching of domains to align the sample magnetisation with an applied magnetic field. The applied field is at an angle with respect to the easy axis so a stronger field is necessary to force all the aligned domains away from the easy axis. From Ref. 5.

This differing response to a magnetic field based on the history or previous applied fields, hysteresis, is a characteristic feature of ferromagnets. A typical ferromagnetic response to an applied field H is shown in Fig. 2.7. The hysteresis loop shows the magnetisation is a maximum at the maximum field, when all magnetic moments in the sample are aligned with the field. As the field is reduced some relaxation occurs but the magnetisation is still non-zero at zero field (remanence). A negative field is necessary to flip the majority of the moments in the sample, and as the field is increased to the negative maximum all moments are forced to align with the field.

2.6 Thin films and multilayers

At the surface of a ferromagnet, the crystal lattice will be disrupted so the surface atoms no longer have a full complement of nearest neighbours with which to bond when compared to the atoms in the bulk of the material. The unpaired electrons of the surface atoms alter the magnitude of the magnetic moments of these atoms, introducing surface anisotropy. Conventionally, "thin"-films are defined as having thicknesses low enough for this surface anisotropy to dominate the behaviour of the film. However, the films studied here are thick enough for the surface anisotropy not to dominate the behaviour, but will still be referred to as thin-films. In these films, the magnetostatic energy will dominate as the spins in the films align in-plane to lower the demagnetisation field.

2.6.1 Exchange bias

One example of the thinness of films leading to interesting behaviour that would not be present in a bulk film is exchange bias. This can manifest when an antiferromagnet (AFM, two sublattices of antiparallel magnetic moments) is interfaced with a ferromagnet. At the interface between the two, the two closest ferromagnetic and antiferromagnetic layers will be exchange coupled if the two types of moments are aligned co-linearly.[2] In the presence of an external magnetic field, which has no net effect on the antiferromagnet, the ferromagnet will preferentially switch in the direction favoured by the exchange coupling, and will resist switching away from that direction; hence the term exchange bias.[23] This is a *unidirectional* (cf. *uniaxial*) exchange anisotropy.

Exchange bias can be seen in conventional hysteresis loops by a horizontal shift of the whole loop, such that $+H_c \neq -H_c$, where H_c is the coercive field of the ferromagnet. It is a thin-film effect since the thickness of the ferromagnet layer must be low enough that the interfacial layer has a measurable effect on the sample as a whole.

The effect is used in the technology of magnetic storage media, removing some uncertainty over the magnetic state of a read head, for example. If the Curie temperature of the ferromagnet is higher than the Néel temperature of the antiferromagnet, field-cooling the system allows the direction of the bias to be controlled, since the exchange field from the "condensed" ferromagnet will inform the direction of the orientation of the antiferromagnet at the interface, and throughout the antiferromagnet.

Fig. 2.9 shows an example hysteresis loop displaying the effects of exchange bias. Both of the coercive field values have the same sign, the whole hysteresis loop

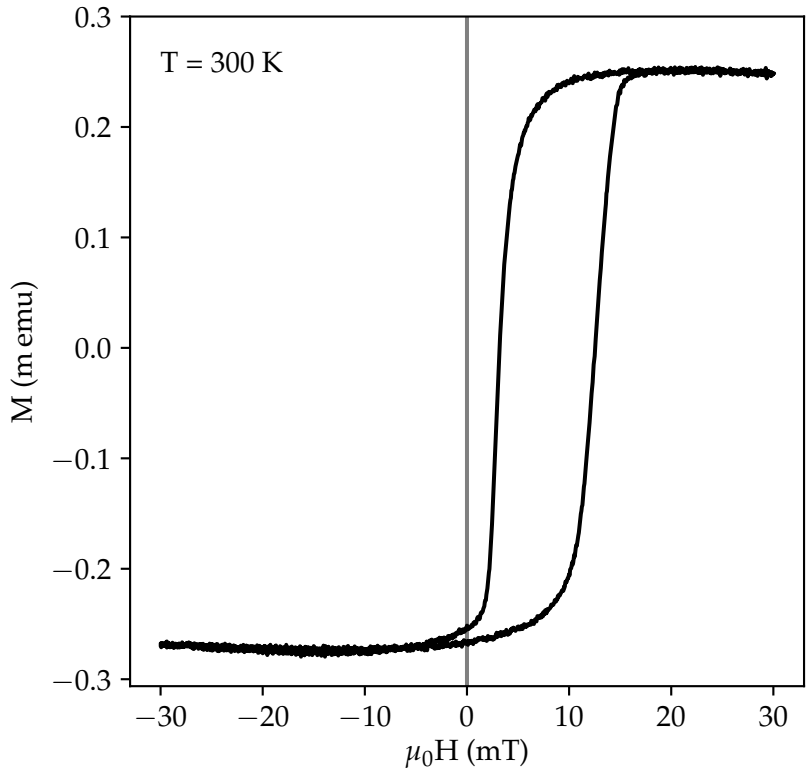

Figure 2.9: Hysteresis loop of a 10 nm Ni film exchange biased by 10 nm of $Fe_{0.5}Mn_{0.5}$. The entire loop has been shifted so far to the right that both coercive field values have the same sign.

has been shifted to the right.

2.6.2 Interfacial coupling

Exchange bias has been used to design magnetically active devices for use in technologies such as magnetic state-based storage. Interest in these devices was initiated by the discovery of giant magnetoresistance, GMR. In typical GMR devices two ferromagnetic layers are separated by a non-magnetic spacer. With difference coercivities, sometimes aided by exchange bias, the two layers can be manipulated by an external magnetic field to point either parallel or antiparallel to one another. The resistance across the device is different depending on the state of the two layers due to spin-filtering of the current as it passes through each layer. In these devices the two magnetic layers are coupled by the RKKY interaction, with the conduction electrons in the non-magnetic spacer layer mediating the coupling.[24,25]

Direct coupling at an interface of the kind in which we are interested, RE/TM coupling, was not well understood at the time of the surge in interest in magnetically active devices. As we have seen, the nature of exchange coupling with rare-earth ferromagnets themselves is not simple, and can lead to a variety of exotic textures within the rare-earths. There was still disagreement over whether the coupling at an RE/TM interface would be parallel or antiparallel, and experimental results were interpreted both ways. (See for example Ref. 26 and Ref. 27.)

Nevertheless, experimental and theoretical results discovered a variety of struc-

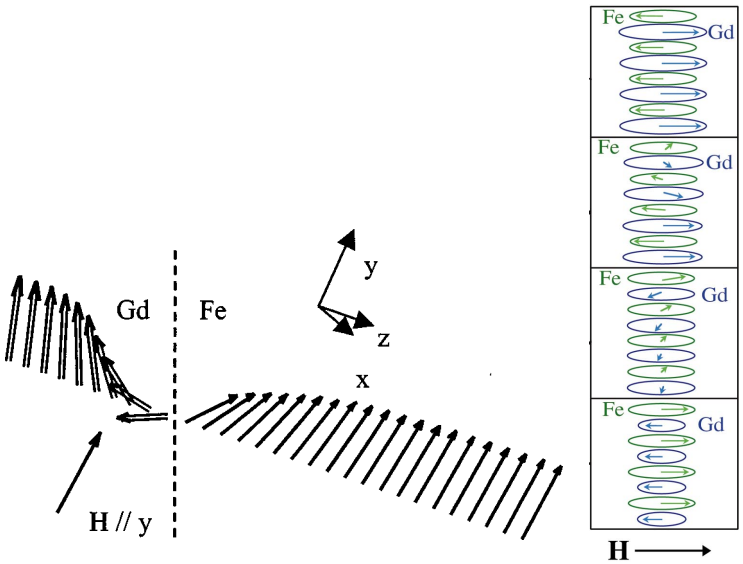

(a) Model of a thin Gd layer interfaced with a thick Fe layer by Van Aken *et al.*. The influence of the antiferromagnetic coupling between Fe and Gd leads to inhomogeneity in the Gd and slight inhomogeneity in the Fe. From Ref. 34.

(b) The effects of temperature on an Fe/Gd superlattice, modelled by Haskel *et al.*. At low temperatures (top), the Gd dominates the magnetic response of the system to an external magnetic field, while the situation is reversed at higher temperatures (bottom). From Ref. 35.

Figure 2.10

tures that can emerge at the RE/TM interface, and the field has maintained interest since the 1980s.[28–32] Consensus was established that the coupling across the interface is antiferromagnetic, and results began to be interpreted in terms of the competition between the RKKY-style coupling across the interface and the intralayer couplings within each layer.[33]

Most experiments have studied the Gd/Fe system, few have studied the Gd/Ni system, and even fewer have studied an RE/TM system with such a powerful element-specific technique as XMCD. Most previous studies also examined systems in which at least one of the layers was just a few atomic layers thick, a lot thinner than the layers in this study. Fig. 2.10 shows work by Van Aken *et al.*[34] and Haskel *et al.*[35] studying the Fe/Gd system. Both show the antiferromagnetic coupling at the interface, in Van Aken's case leading to inhomogeneity in a thin Gd layer, and in Haskel's case showing the effects of temperature on a superlattice structure. This latter result shows similarities to our own results in that at low temperatures the Gd dictates the overall magnetic behaviour of the system, but at the higher temperatures the influence of the Gd reduces until the Fe begins to dominate.

Fig. 2.11 shows the inhomogeneity present at the Fe/Gd interface in a superlattice. In this case the inhomogeneity is increased with an increasing magnetic field strength, and the inhomogeneity shifts out of the Gd and further into the Fe with increasing layer thicknesses.

Barth *et al.* have studied the Ni/Gd system with XMCD, although the study was limited in scope.[37,38] Our results do no contradict those of Barth, but do provide a richer understanding of the system, although we must appreciate that their study did have a slightly different goal from the outset. We will discuss Barth's results

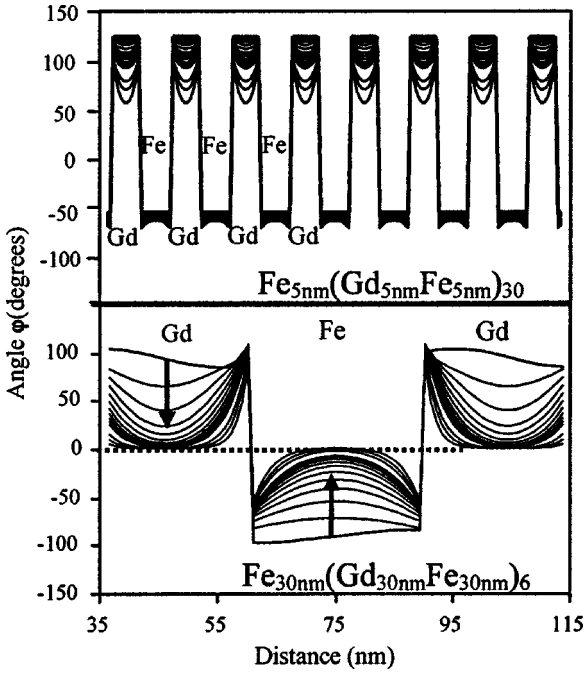

Figure 2.11: Inhomogeneity present in two different Fe/Gd superlattices. In the thinner layers, the inhomogeneity is confined to the Gd layers (top), while in the thicker structure (bottom), the inhomogeneity also penetrates the Fe layer. The solid arrows indicate increasing applied magnetic field strength, from 0 to 1 T. From Ref. 36.

and their relation to ours in more detail during the interpretation of our results in Sec. 6.3.2.

Chapter 3

Superconductivity

Despite there being more superconducting elements (25) than ferromagnetic elements (6) in the periodic table*, superconductivity as a field of enquiry is quite new compared to that of magnetism. This is of course because conductivity needs to be discovered before superconductivity (probably), and because although three of the six elemental ferromagnets are ferromagnetic at room temperature, none of the elemental superconductors is. The closest any of the elemental superconductors gets, Nb, is 9.26 K, or −263.89 °C. Therefore, it took the discovery of how to liquefy helium to enable Kamerlingh Onnes in 1911 to reach the temperatures necessary to observe superconductivity in common metals like mercury, tin and lead.

3.1 Overview

Onnes observed a sudden drop to zero in the resistance of a mercury wire at 4.2 K, and subsequently the resistanceless flow of current has become known as one of the defining features of superconductors. The other is perfect diamagnetism; the expulsion of magnetic fields (Meissner effect) up to a critical field strength. In the case of Type I superconductors, there is only one such critical field strength; Type II superconductors are characterised by allowing partial penetration of the field in the superconducting state by restricting the field lines to vortices, and as such they have two critical field values.

3.1.1 Phenomenology

The London brothers were the first to attempt to describe superconductivity semi-quantitatively in 1935. They modified the Maxwell equations to encapsulate the electrodynamic behaviour of superconductors. An influential treatment was later undertaken (1950) by Ginzberg and Landau based on Landau's theories of second-order phase transitions.[39] They defined an order parameter for the transition, ψ, which is zero in the normal state (the disordered state) and finite in the superconducting state (the ordered state).[4] The temperature of the phase transition is the critical temperature, T_c. Ginzberg and Landau assumed at first that the order parameter described the superconducting electrons' wavefunction.

Although Ginzberg and Landau's treatment was initially separate from a microscopic theory of superconductivity, Gor'kov later linked the two approaches (1959), meaning that in some cases the mathematically simpler phenomenological

*Including holmium.

theory could be used to understand some of the physical concepts behind superconductivity. This helped to shed light on a true physical interpretation of the order parameter as the amplitude probability of finding a Cooper pair at a particular point.

3.1.2 Microscopic theory

In 1957, Bardeen, Cooper and Schrieffer published a comprehensive explanatory theory (BCS theory) which included the mechanism of attraction between two bound electrons (Cooper pair). They showed that despite their opposite charges, electrons in a solid can form attractive bonds mediated by phonons - vibrations in the crystal lattice.[40] A cartoon explanation is that the negatively-charged electron can attract the positively-charged ion core of a lattice site, distorting the lattice and introducing a region of lower Coulomb repulsion for other electrons. This distortion travels through the lattice as a wave - a phonon, whose momentum has been supplied by the initial electron. The phonon passing by a second electron will attract that electron via the Coulomb interaction, and its momentum will be absorbed. In this way, the two electrons have interacted with one another via a phonon, exchanged momentum, and experienced a net attractive force. The mathematical underpinning of the Cooper pair was, as Cooper had shown, that no matter how weak the attractive force between them, two electrons outside the Fermi surface could form a pair with energy lower than the Fermi energy.[41,42]

Experimental evidence which corroborated BCS theory had already been provided in 1950 when the isotope effect was discovered. It showed that as the mass of the isotope from which a superconducting sample is made increases, the critical temperature decreases.

$$M^{1/2}T_c = const. \tag{3.1}$$

Thus, in the limit of infinite isotopic mass, lattice vibrations would disappear, as would superconductivity.[5]

3.1.3 Energy gap

Below the superconducting critical temperature, since it is energetically favourable for Cooper pairs to form, it is also energetically favourable for the maximum number of Cooper pairs to form to lower the total energy of the system. All pairs have the same total momentum in order to facilitate constant reforming of pairs, and as such the system is highly ordered and the Cooper pairs act as a condensate, albeit not a Bose-Einstein condensate[†]. The energy of the condensate is the ground state energy of the superconductor, but above this ground state there is an energy gap. The size of this energy gap is the binding energy of the Cooper pair; to excite an electron out of the ground state enough energy must be supplied to break the electron out of the Cooper pair.

Due to this energy gap, a normal metal adjacent to a superconductor cannot exchange electrons with energy lower than the gap energy without some mediating mechanism. This mechanism is Andreev reflection, in which an electron with energy ε in the normal metal, incident on the interface with the superconductor

[†]The Cooper pair, while made up of a pair of fermions behaves neither purely as a boson nor as a fermion, for reasons outside our scope. For an overview of the explanation see Ref. 5, page 488.

is reflected from the interface on a time-reversed path. All three velocity and momentum components are reversed, along with the charge. The electron has turned into a hole in the normal metal, and the net effect is of two negative charges entering the superconductor as a Cooper pair. These time-reversed states remain coherent over a distance L_c within the normal metal:

$$L_c = min\left(\sqrt{\frac{\hbar D}{\varepsilon}}, L_\phi\right) \tag{3.2}$$

where D is the diffusion coefficient in the normal metal, and L_ϕ is the phase coherence length.[43]

In this way, a "proximity effect" has arisen; the superconductor can have some influence over the normal metal and vice versa.[44–46] In the case of Cooper pairs leaking into the normal metal, is it termed the "*inverse* proximity effect", and the leakage leads to a decrease in the T_C of the superconductor; the superconductivity is suppressed.

3.2 Ferromagnetism and superconductivity

Cooper pairs conventionally occupy a spin-singlet state (Equation 3.2).

$$|s = 0, m = 0\rangle = \frac{1}{\sqrt{2}}\left(|\uparrow,\downarrow\rangle - |\downarrow,\uparrow\rangle\right) \tag{3.3}$$

Intuitively considering a Cooper pair penetrating a strong ferromagnet, we would expect the exchange field within the ferromagnet to influence the electron in the Cooper pair which has a spin antiparallel to the exchange field. For both electron spins to align with the exchange field would break the singlet pair, so we can posit that conventional spin-singlet Cooper pairs cannot exist inside a ferromagnet. Indeed, the Cooper pair acquires non-zero momentum due to the exchange splitting in the ferromagnet, and the wavefunction oscillates in space and quickly decays inside the ferromagnet.[47] This is the FFLO state (Fulde–Ferrell–Larkin–Ovchinnikov).[48,49] The Cooper pairs in the FFLO state can only penetrate $\sim \xi_h = \sqrt{D/h}$ into the ferromagnet, where D is the diffusion coefficient and h is exchange field strength. Fig. 3.1 shows this oscillation of the superconducting wavefunction within a ferromagnet, compared to the usual penetration of the wavefunction into a normal metal.

3.2.1 Spin-triplet generation

In 2003 Bergeret *et al.*[51,52] showed that an additional spin-triplet state exists within the ferromagnet when adjacent to a superconductor, but this spin-triplet state also decays quickly within the ferromagnet as it is comprised of an average of two opposite spins, so has a net spin of $S_z = 0$ when projected onto the direction of the exchange field (z). For long-range penetration of superconducting pairs into a ferromagnet, the net spin projection must be $S_z = \pm 1$ for the pair to be unaffected by the exchange field.

Bergeret *et al.*[53] and Kadigrobov *et al.*[54] proposed a scenario in which singlet Cooper pairs entering the ferromagnet can be transformed into triplet pairs with parallel spin. Since both electrons in the pairs can be aligned with the exchange field in the ferromagnet, the pair can propagate large distances into the ferromagnet,

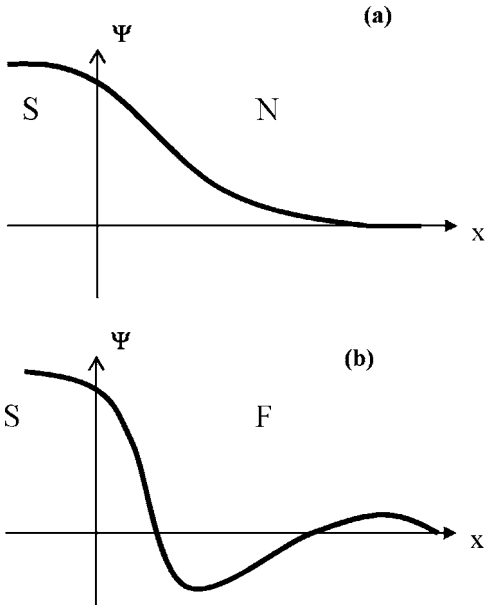

Figure 3.1: Comparison between the proximity effect of a superconductor adjacent to a normal metal (a), and a ferromagnet (b). The oscillations in (b) arise due to the non-zero momentum of the Cooper pairs acquired due to the exchange field within the ferromagnet. From Ref. 50.

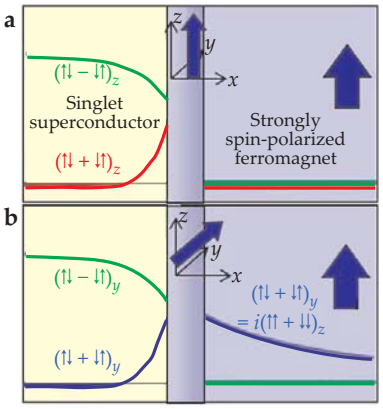

Figure 3.2: Without inhomogeneity present at an S/F interface, both the spin-singlet and spin-triplet pair amplitudes decay rapidly in the ferromagnet (a). With inhomogeneity at the interface, forming a S/F/F′ system, the spin-singlet pair amplitude now penetrates far into the bulk ferromagnet. From Ref. 55.

distances comparable to that of a conventional Cooper pair in a normal metal. This can happen when the singlet Cooper pair passes through a region of inhomogeneous magnetisation near the superconductor / ferromagnet (S/F) interface. The inhomogeneous magnetisation could take the form of a thin ferromagnetic layer (F′) with a magnetisation pointing in a different direction from that of the bulk ferromagnet. The stack would then be of the form S/F′/F. An example of this structure is shown in Fig. 3.2, and the figure shows how the spin-triplet component of the pair amplitudes penetrates the bulk ferromagnet when the inhomogeneity is present, while the spin-singlet amplitudes are strongly suppressed in both cases.

Kadigrobov *et al.*[54] postulate that the length scale of the inhomogeneity should be of the order of the size of the Cooper pair within the ferromagnet for this spin-triplet generation to be effective. Spin-triplet pairs generated in this way would be able to penetrate $\sim \xi_\varepsilon = \sqrt{D/\varepsilon}$ into the ferromagnet, where ε is an energy on the order of the temperature T.

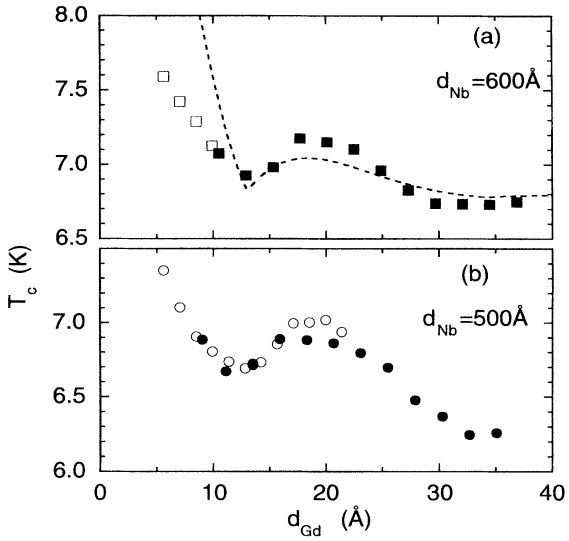

Figure 3.4: Oscillations in the critical temperature of Nb/Gd-based Josephson junctions as a function of Gd thickness. These oscillations are characteristic of π-junctions, in which the phase difference across the junction is π rather than 0. From Ref. 63.

In an S/F′/F/F′/S junction, if the thickness of the ferromagnetic layers with non-collinear magnetisations is suitable, a supercurrent should be able to persist through a relatively thick F layer. An example junction is shown in Fig. 3.3.

3.2.2 Experimental results

Theoretical work on the interaction between thin magnetic and superconducting layers lead to the experimental work of Jiang *et al.* showing the influence of these proximity effects.[57–63] In a Josephson junction, the phase difference between the two superconductors can be non zero in certain situations. Previous to their work, a phase difference of π had only been observed in high-temperature, *d*-wave superconductors. However they found oscillations in their Nb/Gd Josephson junctions characteristic of π junctions. These oscillations are shown in Fig. 3.4.

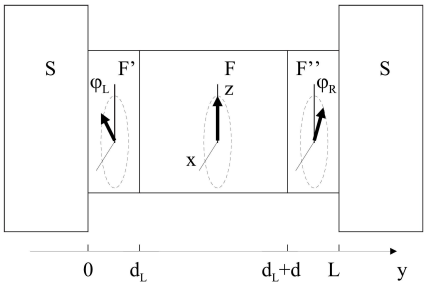

Figure 3.3: An example of an S/F′/F/F″ junction with the necessary symmetrical magnetic inhomogeneity that should generate and propagate a spin-triplet supercurrent. From Ref. 56.

Due to the interest in superconducting spin valves in the last decade and beyond, the fast pace of advancement has sometimes confused the interpretation of results, especially since theory and experiment progressed together.

Without considering spin-triplet generation, superconducting spin valves in an F/S/F′ geometry were being fabricated and studied. The two F layers are switched independently from one another, and the T_c is measured in the parallel (P) and antiparallel (AP) states. Conventionally, the T_c in the antiparallel state is higher than that in the parallel ($T_c^P < T_c^{AP}$) state as the pair-breaking exchange field is

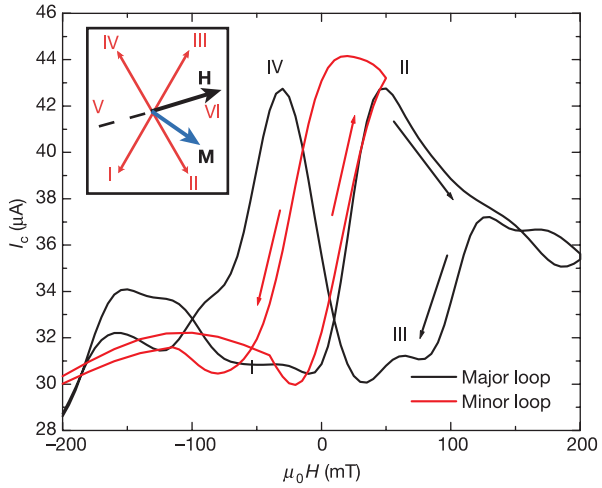

Figure 3.5: Reversible and hysteric changes of the critical current in CrO_2 devices, in which the source of magnetic inhomogeneity was the difference in angle between the applied magnetic field and the easy axes of the CrO_2. From Ref. 71.

partially compensated in the antiparallel state. Results from Moraru *et al.* and Potenza *et al.* demonstrate this effect.[64,65]

However other results showed the opposite effect, dubbed the "inverse" spin valve effect.[66,67] There was some controversy over the interpretation of these results,[68] which followed soon after the conventional experimental results. Fominov *et al.* suggest the inverse spin valve effect can be interpreted as being due to a number of factors including spin triplet generation, as well as magnetic domain structures and spin imbalance effects.[68] Fominov then presents a model of a different system, the S/F/F′ system, and shows that the T_c varies non-monotonically as a function of angle between the two layers, with a minimum when the magnetic layers are coupled biquadratically. This is the same system studied by Bergeret when the prediction was made that such a structure would generate spin-triplets. Fominov also showed that the S/F/F′ structure could exhibit both the conventional and the inverse spin valve effect depending on the parameters of the system. Nowak *et al.*[69] showed the conventional spin valve effect present in both the F/S/F′ and the S/F/F′ geometries.

So while some spin valve devices have been designed with the goal of generating spin-triplet pairs explicitly in mind, results from other devices are interpreted using known spin-triplet generation mechanisms, or simply by considering the relative strength of the exchange field in different alignments of the ferromagnetic layers.[70]

After Bergeret *et al.*[53] and Kadigrobov *et al.*'s theoretical work,[54] Keizer *et al.* made a simple device from the half-metal CrO_2 which relied on the angle between the applied magnetic field and the CrO_2 easy axis to generate magnetic inhomogeneity.[71] By using a half-metal they had shown that the long-range supercurrent must be highly spin-polarised. Fig. 3.5 shows how the critical current of the device could be controlled by the application of an external magnetic field.

Klose *et al.*, achieving (nearly accidentally) higher control over the magnetic state of their device, used a synthetic antiferromagnet (SAF) made of Co/Ru/Co aligned perpendicular to ferromagnets in an S-F′-SAF-F′-S configuration.[72] The SAF was originally intended merely to provide a strong exchange field, however

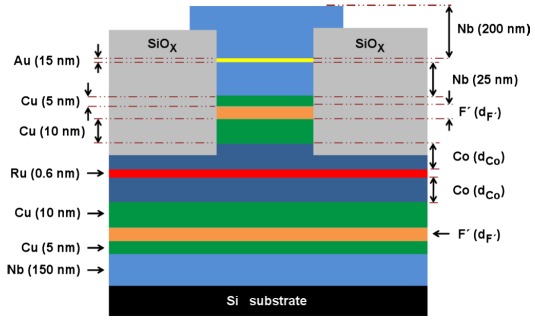

Figure 3.6: Geometry of the Josephson junction used in the experiments by Klose *et al.*. The Cu layers are used as magnetic spacers and the Co/Ru/Co layers make up the synthetic antiferromagnet. The layers marked F′ were either Ni or PdNi. From Ref. 72.

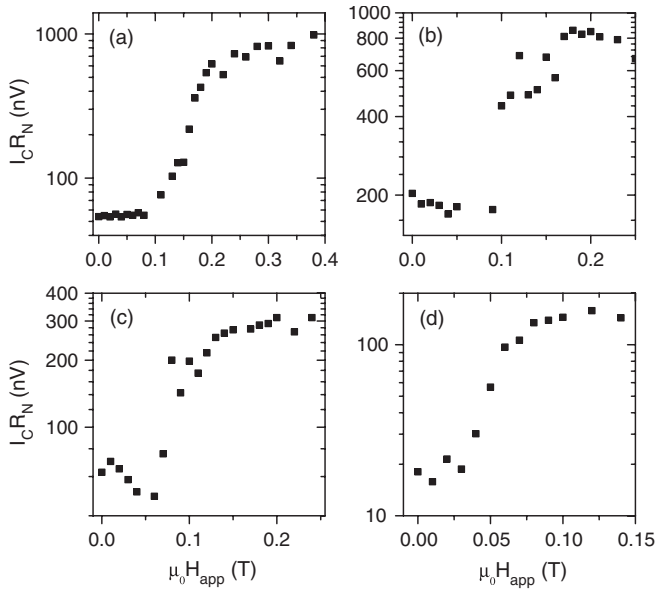

Figure 3.7: Characteristic critical current of spin-flop-driven devices, with Ni as the ferromagnetic layer. The spin-triplet supercurrent increases after the structure undergoes the spin-flop transition. Ni thickness was 1.0, 1.5, 2.0 and 2.5 nm for (a) to (d), respectively. Measurements performed at remanence. From Ref. 72.

it underwent a spin-flop transition after an external field was applied and then removed, thereby entering a new ground state of biquadratic coupling. The new state provided the necessary non-collinear magnetisations for generating the spin-triplet pairs.

Fig. 3.6 shows the structure of the device used in that experiment. The F′ layers were either Ni or $Pd_{0.88}Ni_{0.12}$, and are magnetically isolated by the Cu from the SAF Co/Ru/Co layers. Fig. 3.7 shows the increase in the critical current of devices due to the spin-flop transition driven by the applied magnetic field.

Other experiments have used the intrinsic inhomogeneous magnetic structure of holmium to generate spin-triplets. In some instances Ho can form a helical and conical magnetisation, with the magnetisation of successive atomic layers rotated in-plane, and canted out-of-plane, with respect to the previous layer. Sosnin *et al.* and

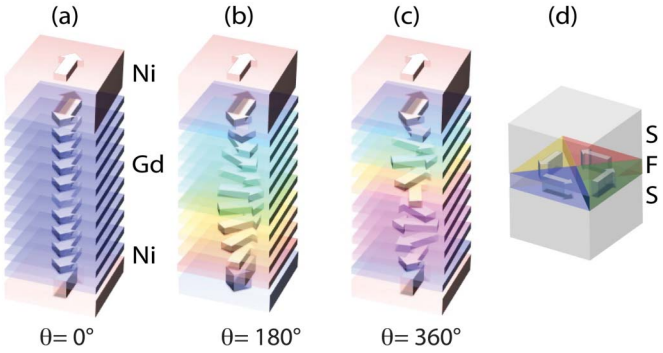

Figure 3.8: The presumed magnetic structure of a Ni/Gd/Ni structure, with the top Ni layer pinned and the bottom one rotated 180° (b), and 360° (c). No inhomogeneity was expected in the Ni layer, and a Bloch domain wall was expected in the Gd layer. From Ref. 78.

Robinson *et al.* investigated current-parallel-to-plane and current-perpendicular-to-plane geometries, respectively.[73,74] Sosnin found that his device showed the same phase-periodic oscillations as had been observed in similar Andreev interferometers with normal-metal weak links instead of ferromagnetic weak links. Robinson found that Ho provided the necessary magnetic inhomogeneity to generate a spin-triplet supercurrent that then flowed through a thick Co layer. It was found that the number of "turns" made by the Ho magnetisation affected the flow of the supercurrent.

In terms of potential applications of these types of devices, it is unfortunate that in this instance (Ho/Co/Ho) the spin-triplet supercurrent cannot be controlled *in situ*, i.e., without changing the design of the device. It is hypothesised that by removing the magnetic inhomogeneity with an external field the supercurrent could be switched off. However, the applied field needed to unwind the magnetisation of the Ho was found to be too large to be practical.

Gu *et al.* also used the intrinsic inhomogeneity of Ho, and at first only made quasi-irreversible switching devices; the devices required warming above a magnetic transition temperature in the Ho.[75] However, later experiments used a Ho/Nb/Ho geometry with slightly different Ho thicknesses so that the coercive field of each layer was different. By switching the two Ho layers from parallel to anti-parallel the T_c of the Nb layer is changed by ∼400 mK. Similar results were observed for Dy/Nb/Dy structures.[76] In another experiment, it was thought that creating an artificial magnetic helix (or Bloch domain wall) would make for easier control of the supercurrent. Since domain walls had been shown to exist in permalloy/Gd/permalloy multilayers by Prieto *et al.*,[77] Ni/Gd/Ni multilayers were used to create the spin-triplet supercurrent.[78]

It was found that the flow of the supercurrent depended on the magnetic field history of the devices, and this was thought to be due to the winding and unwinding of a domain wall in the Gd layer. Fig. 3.8 shows the preliminary interpretation of the magnetic structure of the Ni/Gd/Ni system by Robinson *et al.*. It was thought that the default configuration would be antiferromagnetic Ni and Gd layers, and that if one Ni layer could be pinned in some way and the other rotated, the interfacial antiferromagnetic coupling would induce a 180° domain wall in the Gd, possibly even a 360° wall if the Ni was rotated further. This model

did not expect any inhomogeneity in the Ni layers, and indeed the design of the experiment would not to be able to detect the exact nature of the inhomogeneity in the devices, only that there was inhomogeneity.

It is the detailed examination of this Ni/Gd/Ni structure that makes up the bulk of this research. Indeed, the symmetric nature of all the Ni/Gd/Ni structures studied stems from the symmetry required to convert spin-singlet pairs into spin-triplets and vice versa in the current-perpendicular-to-plane geometry used in Robinson's experiments.

Part III

Results

Chapter 4

Film deposition and characterisation

Films are deposited by D.C. magnetron sputtering onto a variety of substrates. For thickness calibration, magnetic and transport measurements on non-epitaxial films, SiO_2 substrates are used. For XMCD, a Si_3N_4 membrane atop a windowed SiO_2 wafer is used, because the Si_3N_4 is transparent to the x-rays used in XMCD. For epitaxial films, a-plane sapphire (Al_2O_3) is used.

4.1 Sample preparation

The silicon and sapphire substrates are cut from a large wafer using either a diamond saw or diamond-tipped scriber. They are then cleaned in acetone in an ultra-sonic bath, rinsed in isopropyl alcohol and dried with compressed air or nitrogen. The Si_3N_4 substrates arrived from the manufacturer pre-cut and are too delicate for cleaning ultra-sonically as the thin window can easily break. Dust is blown off the surface with compressed air or nitrogen.

4.2 D.C. magnetron sputtering

D.C. magnetron sputtering is a physical vapour deposition method of fabricating thin films.[79–81] A plasma (argon, in this case) is ignited in a high vacuum chamber and the target, part of the cathode, attracts the positively charged ions. The ions collide with the target atoms, some of which are ejected from the target along with secondary electrons. These target atoms are then deposited on the substrate. Specific to magnetron sputtering, the cathode also has permanent magnets that generate an axial magnetic field that, combined with the electric field, traps electrons near the target surface which increases the rate of ionisation, enabling lower pressures to be maintained without the plasma extinguishing.[82] Trenches in the target left from this electron trapping are shown in Figure 4.1. This increases the deposition rate. The thickness of the samples can be controlled by varying the pressure of gas in the chamber, the power supplied to the cathode, the distance between the target and the substrate, and, as in the case of these experiments, the amount of time the substrate is exposed to the sputtered flux of target atoms.

To achieve ultra-high vacuums within the deposition chamber, either turbo-molecular or diffusion pumps are used. Whenever Nb is grown for its superconductivity rather than as just a buffer or capping layer, the vacuum chamber walls are also cooled with liquid nitrogen to act as a cryopump; residual gases in

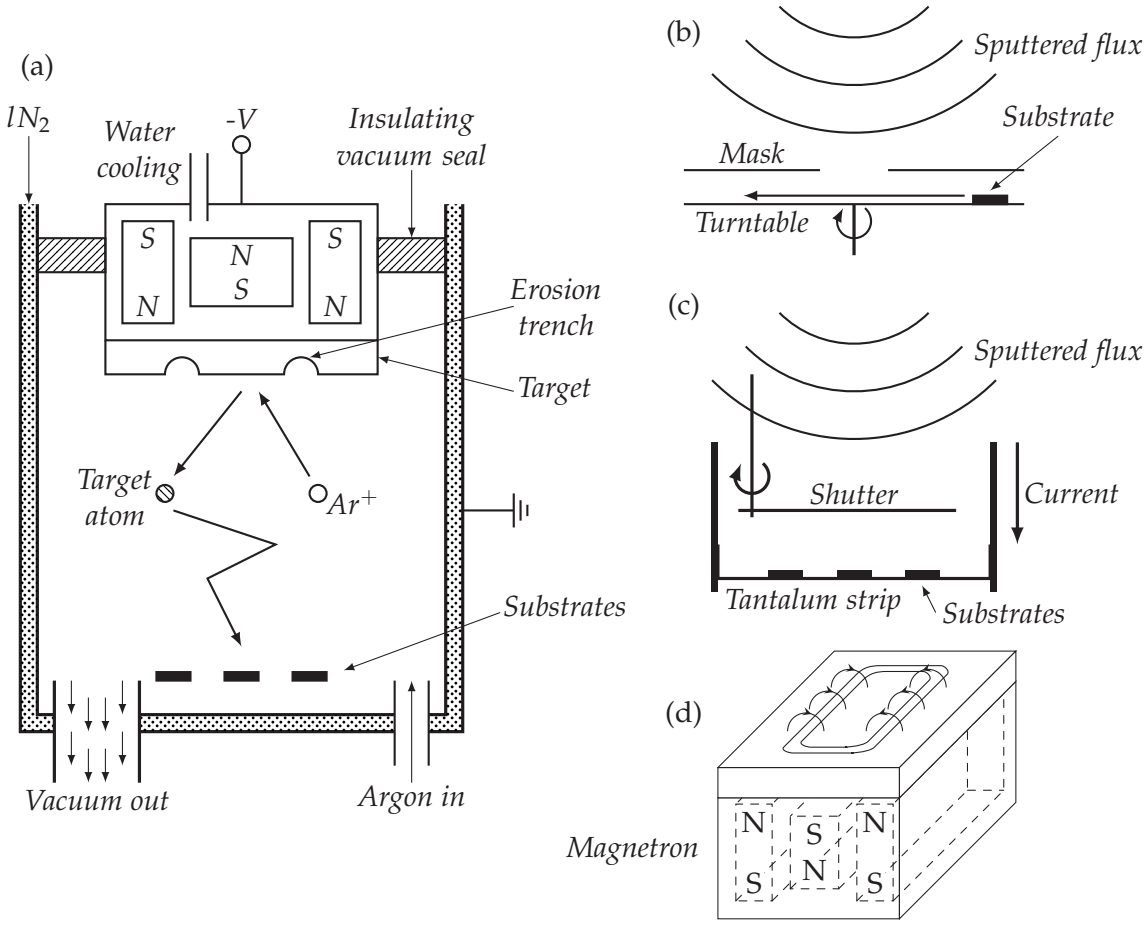

Figure 4.1: (a) Overview of sputtering process, not including a method for controlling the thickness of the films. (b) Substrates are protected by the mask during pre-sputtering, and rotated at a set speed during sputtering - exposing the substrates to the sputtered flux through a gap in the mask for a set time period. (c) Substrates are protected by the shutter during pre-sputtering, and the shutter is opened for a set time period during sputtering. (d) The magnet configuration within a magnetron which produces the desired field lines to trap electrons at the surface of the target, albeit in a restricted race-track which reduces even utilisation of the target.

the chamber condense on the cold walls. Immediately before the deposition, the pressure in the chamber is measured with a residual gas analyser.

Appendix C shows the phase diagram for the Gd-Ni binary alloy, and Fig. 4.2 shows the amount of Gd atoms that diffuse to the surface of a Gd/Ni bilayer, through 5 nm of Ni. Since all of the Gd/Ni structures grown for this research were grown at room temperature or below and were not annealed, we can be confident that the Gd and Ni layers will not have completely mixed during growth.

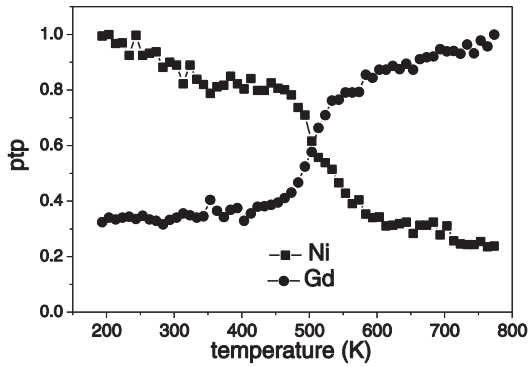

Figure 4.2: Auger-electron intensities (relative) of a Ni/Gd (5/15 nm) bilayer during annealing. Although the Gd migrates through the Ni to the surface at high temperatures, at the temperatures at which our samples were deposited, no movement can be detected. From Ref. 83.

4.2.1 Epitaxial growth

Two different methods were used to vary the time spent by the substrate in the flux of target material. In the first, used for non-epitaxial growth, and for all of the samples measured by XMCD, the substrates are mounted on a turntable which rotates underneath the target. The speed of rotation is varied to control the film thickness since this controls the amount of time the substrate spends in the "field-of-view" of the target and the flux of sputtered atoms.

However for epitaxial growth, the substrates need to be heated, which is difficult to achieve with a turntable, so a static heater strip made of tantalum is used, with shutters between the magnetrons and the heater. When the plasma is alight, the shutters are opened for a certain period of time, directly controlling the amount of time the substrates spend in the flux of target material.

Current is passed through the tantalum strip to heat it, with temperature calibration carried out using a disappearing-filament pyrometer. Heater currents of 38 and 24 A (corresponding to 880 and 650 °C) were used for Nb and all rare-earth metals, respectively.

4.2.2 Deposition rates

The thickness of the grown films and therefore the deposition rate was calibrated by scanning a profilometer or atomic force microscope across a step-edge created in thick films. For non-epitaxial film, the step-edge is created by marking the substrate with a permanent marker, and dissolving the mark in a solvent after deposition (usually acetone). The metal deposited on top of the mark breaks away from the rest of the film leaving bare substrate exposed adjacent to the deposited film. For epitaxial films the permanent marker method is not used since the marker ink can evaporate or out-gas during the heating of the substrate and contaminate the films that are grown. Instead, a thin strip of platinum foil is wrapped around a sample to create a mask.

For those films which were measured by XMCD, the thickness can also be calibrated by the x-ray measurements. This calibration technique is discussed in Sec. 4.4.1.

The deposition rates used to grow thin films are the following: $(0.035 \pm 0.004)\,\mathrm{nm\,s^{-1}}$ for non-epitaxial Ni, $(0.16 \pm 0.02)\,\mathrm{nm\,s^{-1}}$ for non-epitaxial Gd, $(0.047 \pm 0.005)\,\mathrm{nm\,s^{-1}}$ for epitaxial Nb, $(0.058 \pm 0.006)\,\mathrm{nm\,s^{-1}}$ for epitaxial Ho, and $(0.10 \pm 0.01)\,\mathrm{nm\,s^{-1}}$ for epitaxial Gd.

4.3 X-ray diffraction

The structure of the grown thin films can be studied with x-ray diffraction (XRD).[84] For epitaxial samples, the growth phase can be determined as well as the crystallographic orientation. Epitaxial samples are those which have been grown in such a way as to form a well-defined crystal structure based on the crystal structure of the substrate, or the previously grown layer. In our case, this is achieved by heating the substrate to a high temperature during growth.

When x-rays are incident on the sample surface, they will reflect from different layers in the crystal and constructively or destructively interfere according to Bragg's law:

$$n\lambda = 2d\sin\theta \tag{4.1}$$

where n is the integer index of the interference fringe, λ is the wavelength of the x-ray, d is the spacing between crystal layers, and θ is the angle between the incident x-ray and the plane of the crystal lattice layer.[85] Where the scattered x-rays from the crystal have a path length difference equal to the wavelength of the x-ray (or an integer multiple), the scattered x-rays will constructively interfere, which can be detected as a peak in a spectrum if all scattered x-rays are captured.[86] X-rays are chosen since their wavelength is very close to the spacing in a typical crystal lattice. In this case Cu K_α radiation is used, with a wavelength of 1.54 Å.

For a typical 2θ-ω scan, the angle of the incident x-ray with respect to the sample surface (ω) is scanned synchronously with the detector moving through angle 2θ. Peaks in the resulting intensity spectrum as a function of 2θ show the crystallographic planes present in the sample. These planes are represented by Miller indices, defined as the inverse of the intercepts of the plane by the lattice vectors.[87]

For most materials used in this research that were grown epitaxially, x-ray diffraction is used to find out whether any crystal planes other than the intended

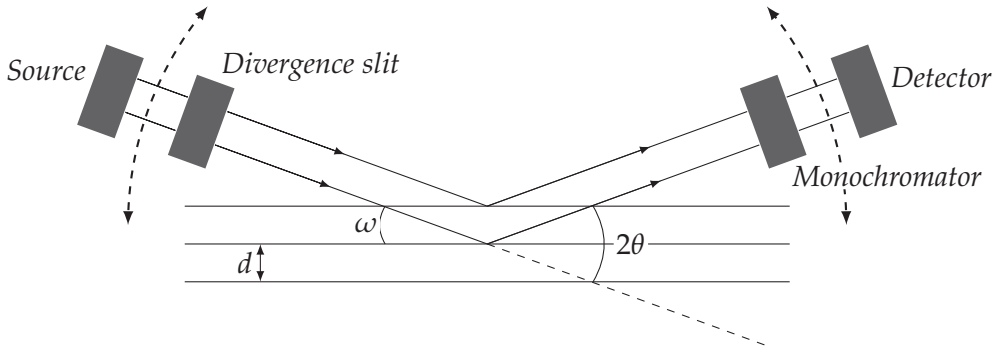

Figure 4.3: Schematic of XRD process: X-rays are generated at the source and the beam is collimated before hitting the sample. The angles ω and 2θ are shown, as well as the interplanar spacing d. The source and detecting assemblies can both move along the ω-2θ angles.

ones are present in the sample. However, Gd strongly absorbs the radiation produced by the source in the machines, so results from Gd films may not be as easily interpreted.

4.4 X-ray magnetic circular dichroism

4.4.1 Theory

XMCD uses circularly polarised x-rays with controllable energy to probe the magnetic structure of specific elements in a sample.

Circularly polarised photons carry an angular momentum (Figure 4.4(a)) which they transfer to a photoelectron in the sample; left- and right-circularly polarised photons transfer opposite spin to the photoelectron. Due to the exchange field in a ferromagnet there is an imbalance of spin-up and spin-down electrons and therefore an imbalance of spin-up and spin-down holes. A photoelectron can only be excited to a hole state with the same spin as that of the incident photon because spin flips are not allowed in electric dipole transitions. Since a photon can only excite an electron with an available excited state the absorption of an incident polarised x-ray beam is a measure of the availability of a particular spin-state in the sample. By changing the available states (Figures 4.4(b) and 4.4(c)), for example by changing the magnetisation of the sample, or the polarisation of the x-rays, the difference between the two can be measured.[88,89]

The attenuation of x-rays through matter is described by the Beer-Lambert law:

$$I = I_0 e^{-\mu d} \tag{4.2}$$

where I_0 is the incident x-ray flux, μ is an element-specific constant, and d is the thickness of the sample. Therefore, the thickness of the sample can be calibrated by XMCD to corroborate the methods outlined in Sec. 4.2. This is done by measuring the difference between the incident x-ray flux and the transmitted x-ray flux at an absorption peak for a particular element.

4.4.2 Typical XMCD setup

XMCD measurement configurations require three stages: x-ray generation, guiding the x-rays to the sample, and measuring the absorption of the x-rays by the sample. The latter two stages are usually referred to as the "beamline" and "endstation", respectively.

To generate circularly polarised x-rays at the Stanford Synchrotron Radiation Lightsource (SSRL), where these measurements were performed, an elliptically polarised undulator (EPU) is used. This is an insertion device placed within the particle accelerator ring in the path of the orbiting electrons. It is made up four rows of magnets, each row alternates between north and south poles. A pair of such rows, placed opposite one another on each side of the electron beam will cause the electrons to veer in one direction as they pass through a N-S pair, and in the opposite direction as they pass through the following S-N pair. In this way, the electron path oscillates in one dimension, and emits linearly polarized light. By adding another pair of rows of magnets perpendicular to the first pair, and by changing the relative offsets between all the rows along the beam propagation direction, the electrons can be made to follow a helical path as they pass through

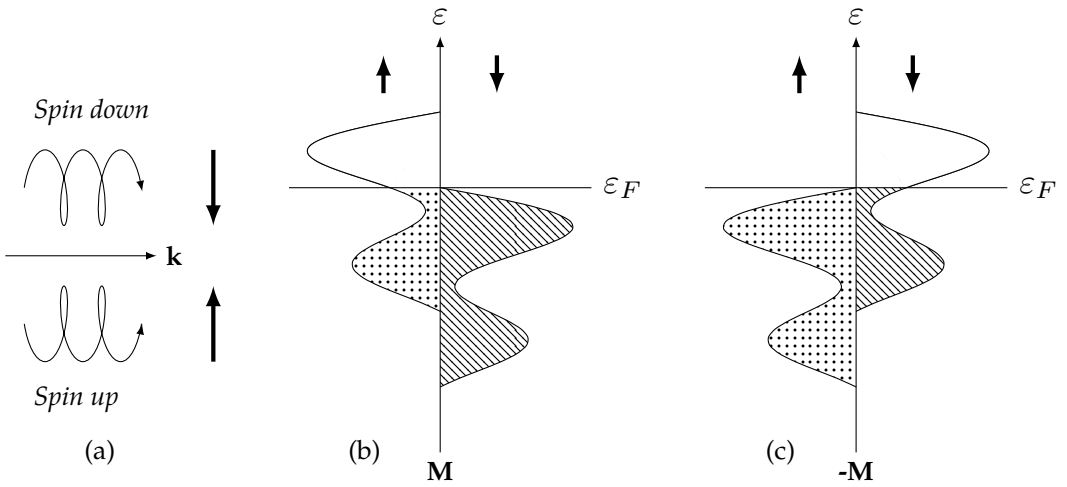

Figure 4.4: Circularly polarised x-rays with wave-vector k carry a spin angular momentum (a). Whether or not an x-ray can interact with a sample is determined by the spin of the available states in the sample. In (b) only holes with spin "up" are available so only x-rays with the corresponding spin can be absorbed. The x-ray will excite a spin-up electron into a spin-up hole. Any spin-down x-rays incident on this sample will not be absorbed and will be detected in transmission. The situation will be reversed if the sample's saturation magnetisation is reversed (c).

this undulator, emitting circularly polarised light. The polarisation can be changed by moving these rows of magnets, and therefore reversing the chirality of the helix.

Once the x-rays have been generated, they need guiding down the beamline to the endstation. For soft x-rays (energy of 200 eV to 1200 eV), grazing incidence mirrors can be used since they preserve the polarization of the incident x-rays.

The detection equipment is located at the endstation, along with fine controls for maximising the x-ray flux onto or through the sample. Detection can either be of transmitted x-rays, emitted photoelectrons, or fluorescence. Equipment for applying fields to the sample, heating or cooling the sample, and so on, are also located at the endstation.

4.4.3 Experimental procedure

At SSRL, electrons are stored in the accelerator ring in "buckets". 372 buckets are stored at any one time, each bucket containing 1 pC of charge. The buckets are 50 ps long, and are separated by 2.1 ns. They have a kinetic energy of 3 GeV. Due to constant losses from the beam over time, new electrons are injected into the buckets every five minutes, leading to a sharp increase in the beam current over approximately thirty seconds.

As mentioned above, the circularly polarised x-rays are generated by an EPU at SSRL, which is described in detail in Ref. 90.

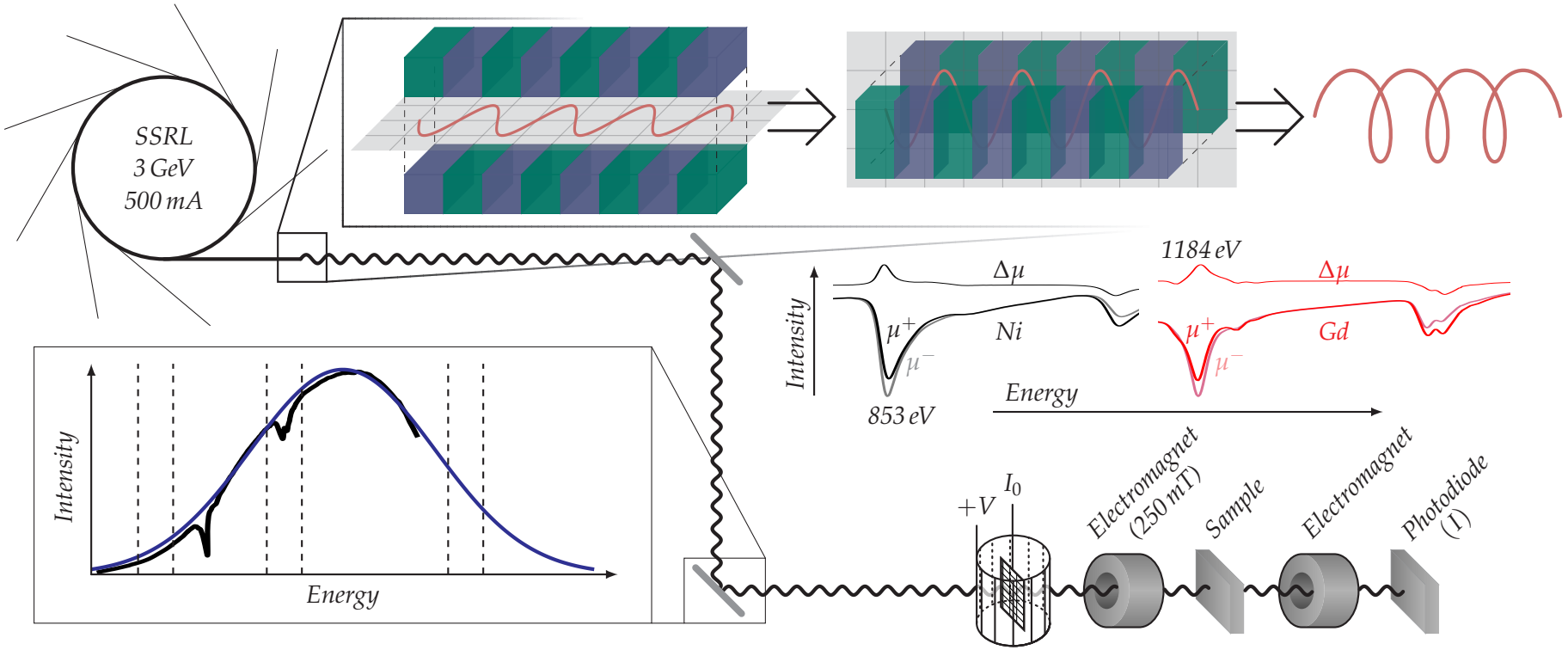

Figure 4.5: Electrons from the accelerator ring (a) are passed through the elliptically polarizing undulator (EPU, b), in which the magnet positions are controlled by motors to set the polarisation direction of the emitted x-rays. The x-rays are focussed by beam-line optics (c) incorporating a feedback system which eliminates beam movements originating at the source, and the energy of the incident x-rays can be selected by these optics. The x-rays pass through a photodiode, I_0, a coil of an electromagnet, the sample, the other coil of the electromagnet, and the final photodiode I_t. (d) shows the Gaussian distribution of x-ray energies as a function of intensity, and how, by adjusting the beam-line optics, a particular absorption edge can be brought to the peak of the intensity spectrum to maintain as high a signal to noise ratio as possible. (e,f): Example Ni and Gd XMCD spectra are shown (Ni in black, Gd in red), as well as the difference ($\Delta\mu$) between the positive and negative transmittance (μ_+ and μ_-, respectively).

Having been generated, the x-rays travel down the beamline to the endstation. The beam is first deflected in the horizontal plane by a mirror which also removes the higher energy x-rays, reducing thermal load on the rest of the beamline optics. The beam is focussed onto an entrance slit approximately 15 µm in size, before passing through a spherical grating monochromator (SGM). The SGM projects a twice magnified image of the entrance slit onto an exit slit, which is placed such that adjusting the position of the SGM changes the energy of the x-rays passing through the exit slit. The exit slit assembly consists of several electrically isolated horizontal slits. Each slit's electron yield due to the incident x-rays is measured and input into a PID circuit which adjusts the horizontal mirrors to keep the beam centred regardless of fluctuations in the beam. The beam diverges after leaving the exit slit and by the time it has reached the sample is approximately 1 mm $\times$ 0.5 mm, as shown in Fig. 4.6. The beamline (numbered 13-1) used at SSRL for all of the XMCD experiments in this thesis is described in the appendix of Ref. 91.

At the endstation, four samples at a time can be clamped onto the copper sample holder. The sample holder is on the end of a cryostat arm, and a K-type thermocouple at the bottom of the holder gives an accurate reading of the samples' temperature; both the samples and thermocouple are in thermal contact with the copper. The sample holder can be manipulated in the x and y directions, where z in the beam propagation direction, and y is the axis along which the line of four samples lie. The samples can also be rotated around y. In all of the XMCD measurements described herein, the samples were rotated at an angle of 30° with respect to the incident x-ray beam. This is the result of a compromise between two factors: that only the projection of sample magnetisation onto the x-ray propagation direction can be measured by XMCD, and that the x-ray has to pass through the window in the sample, which for some samples was only 0.5 mm $\times$ 0.5 mm. The SSRL beamline and XMCD endstation are shown in 4.5, along with example XMCD spectra.

All computerised motors along the beamline can be controlled from the endstation. The EPU phase can be changed to select a polarisation direction of the x-rays, and the gap between the EPU magnets can be varied to coarsely control the energy of incident x-rays. The electrons in the synchrotron are distributed on a bell curve of intensity as a function of energy. The EPU itself also yields a bell curve of intensity of the x-rays it generates, so by moving the EPU gap motor, one bell curve is being scanned along and superimposed on another. It is important to choose an appropriate value of the EPU gap so that the produced bell curve does not affect data analysis. Figure 4.7 shows the effect of the bell curve from the EPU before the data is normalised.

When an appropriate energy range has been selected by the EPU gap, fine energy control can be achieved by rocking the SGM (recorded in the data files as moving the MONO131 motor).

Three different types of measurements were performed using the x-rays, described below:

XAS (x-ray absorption spectroscopy): The SGM control is ramped in steps to sweep the x-ray energy, and the incident and transmitted x-rays are counted for 1 second at each energy. This was mainly used for setting up the beam parameters.

XMCD: At each of the positive and negative saturation magnetic fields, the x-rays are counted for 1 second, the energy is then increased by one step, and the process is repeated. An equivalent measurement would be to change the polarisation of the x-rays rather than the sign of the applied field. Before an XMCD measurement which does use the magnetic field, the EPU gap must be correctly positioned to ensure the incident x-rays are indeed circularly polarised.

Hysteresis: The energy is selected and fixed at the absorption peak of the element being measured. Then the magnetic field is swept from low to high and back again, and at each field step the x-rays are counted for 1 second.

Most measurements are hysteresis measurements since the XMCD measurements were not performed at different temperatures. For each sample that is measured by hysteresis, the correct energy setting for the x-rays must be found by XAS or XMCD and selected by moving the EPU gap and SGM motors. Then the incident x-ray flux is maximised by x and y adjustments to sample position. When the hysteresis measurement has completed for one energy, and therefore one element of the Ni and Gd, the same sample position optimisation must be performed due to chromatic aberration in the beamline optics. When both the Ni and Gd layers of one sample have been measured, the sample holder is moved through y to the next sample, and the process is repeated. When all four samples have been measured at one temperature, the temperature is increased and the process starts again, moving back through the samples in the y direction. At each step, the signal optimisation process must be performed. The temperature is controlled by moderating the flow of helium through the cryostat, and at higher temperatures by also running current through a small resistance heater.

The measurements were performed at SSRL in four different beam-time allocations. Each beam-time session consists of three to five days, with access to the beam twelve hours per day, either from 0600 to 1800 or vice versa.* At the beginning of each visit, the beam-line scientist† would optimise the beam but the vast majority of subsequent measurements would be done solely by me.

An example XMCD spectrum is shown in Figure 4.8b. In these experiments the difference in absorption is achieved by switching the magnetic field from $\geq +M_s$ to $\leq -M_s$ instead of changing the polarisation of the x-rays. The measurement is the number of photons detected by a diode behind the sample during one second. The incident beam intensity is also measured so the signal can be normalised to remove any artefacts from beam instabilities.

The experimental setup for taking XMCD measurements is shown in Figure 4.8a. The x-rays are measured in transmission. The magnetic field, $\mu_0\mathbf{H}$, of up to 250 mT is applied parallel to the x-ray beam. In some cases, this field may not have been enough to saturate our samples.

*Except in an instance when an administrative hiccup left me with a 24 hour shift.

†We are indebted to Hendrik Ohldag for his work as the beam-line scientist.

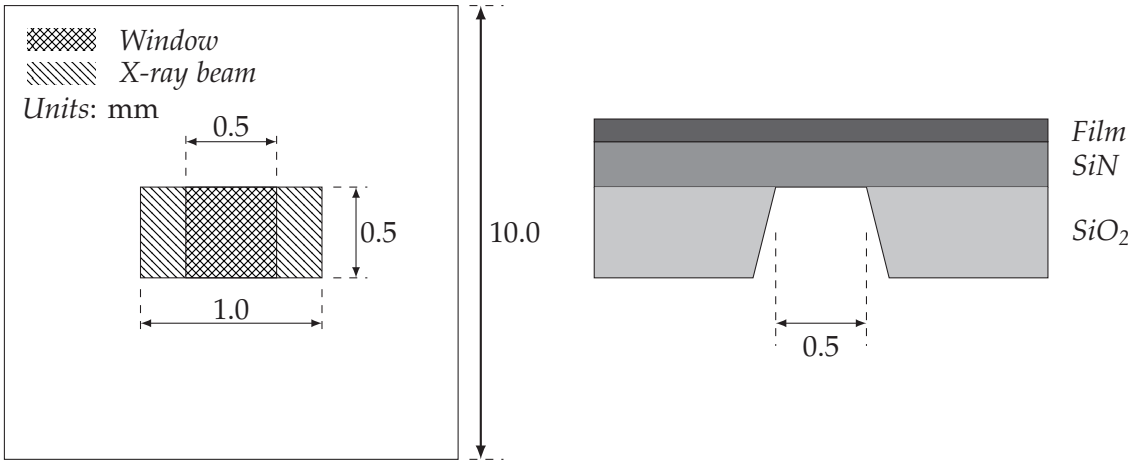

Figure 4.6: Left: Geometry of incident x-ray beam with respect to transparent (to x-rays) window in the substrates. Right: Cross-section of substrate. Si_3N_4 is grown on SiO_2 and the window in the SiO_2 is milled away from below (by the substrate manufacturer). The film is then sputter deposited onto the Si_3N_4.

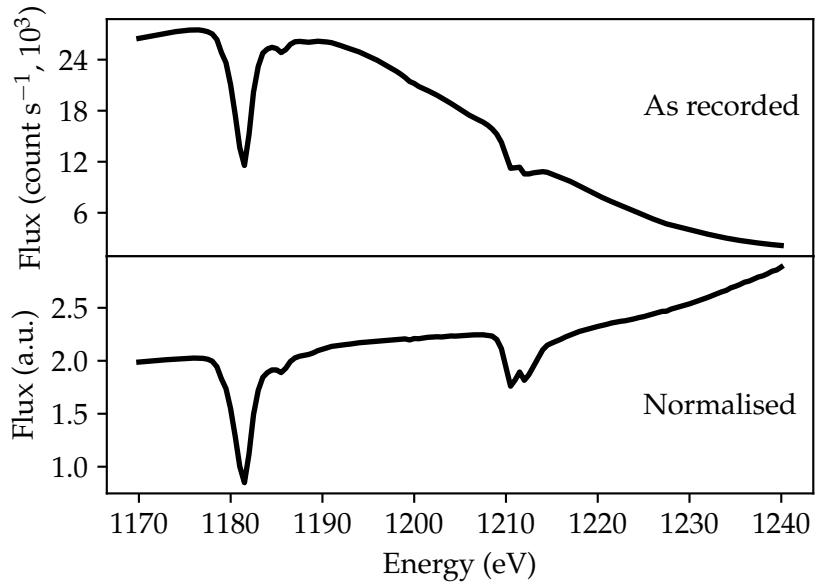

Figure 4.7: Top: XAS measurement as recorded; as well as the signal from the sample the intensity follows the normal distribution of x-ray energies due to the beam-line optics (as explained above). Bottom: The same measurement after normalisation with respect to the incident x-ray flux.

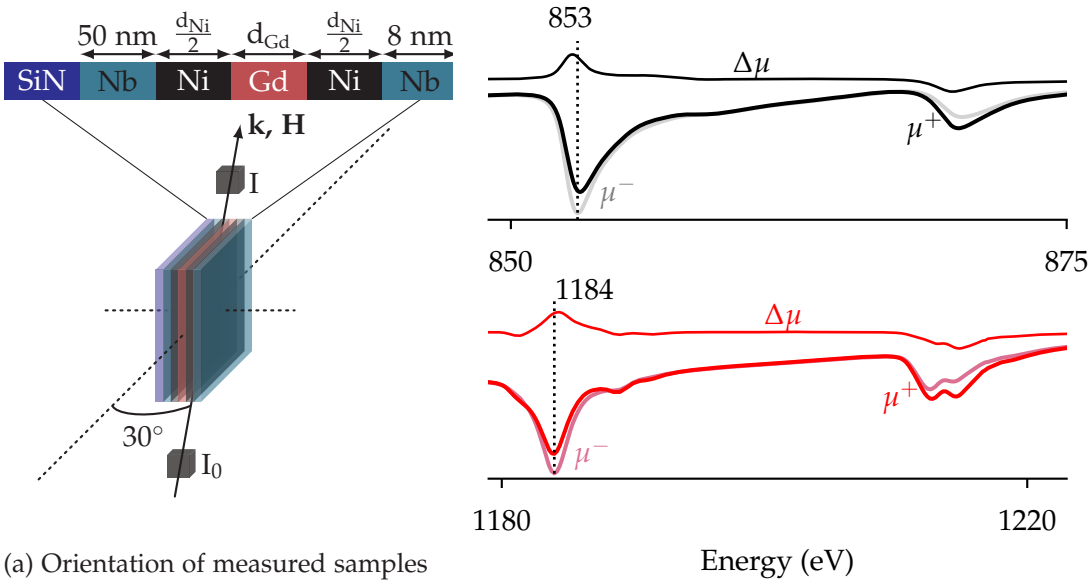

(a) Orientation of measured samples with respect to the incident x-ray direction and externally applied magnetic field. I_0 and I represent the photodiodes measuring x-ray flux before and after the sample in the beam-line, respectively.

(b) Example XMCD spectra from the Ni (top) and Gd (bottom) layers of S3. The individual signals from each saturation magnetisation direction is shown, as well as the difference between them.

Figure 4.8

4.5 Low temperature transport

4.5.1 4.2 K probe

A variety of low temperature transport measurements have been undertaken on various samples mentioned throughout this work. The simplest is measuring resistance vs temperature of a sample in order to determine the critical temperature of a superconducting Nb layer. A dipping probe with electrical connections to the surface of the sample is lowered into a dewar of liquid helium; from the top of the dewar down to the surface of the liquid helium, the temperature of the helium gas decreases continuously so as the probe is lowered through the gas to the liquid it is gradually cooled down from room temperature to a minimum of 4.2 K. Resistance is measured using a four-point technique with all four electrical contacts in a row, and the current contacts at the ends of the row.[92,93] This measurement setup is shown in Fig. 4.9. The current flows in the plane of the thin-film sample, and through the superconducting layer of the sample.

The current used for superconductivity measurements is important, as superconductors have a critical current above which they enter the normal state. Currents also must not be high enough for any heating of the sample to affect the measured critical temperature. However, the higher the current used the better the signal-to-noise ration. In these experiments, currents below 100 µA were typically used. This value was arrived at by performing several measurements of the critical temperature of a sample with different currents to determine which current magnitudes altered the measured T_c.

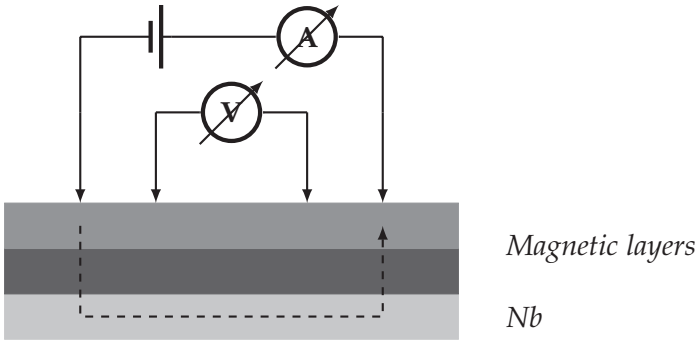

Figure 4.9: Illustration of the four-point measurement used for transport measurements. Current is supplied and monitored across the outer contacts, and the voltage is measured across the inner contact. The current flows in the plane of the thin-film samples, and through the superconducting layer when $T < T_c$.

4.5.2 Magnetoresistance measurements

The dipping probe is limited to electrical measurements down to liquid-He^4 temperatures - for lower temperatures and for an applied magnetic field a cryogen-free‡ refrigeration system is used. A Mini Cryogen Free System by Cryogenic Ltd. was used for magnetoresistance measurements, and successive T_C measurements which required a magnetic field to be applied during or between each measurement. The cryostat can apply an in-plane field of 1 T, and can cool down to 1.4 K by pumping on a pot of liquid helium. The most energetic atoms are evaporated from the pot and therefore the average kinetic energy of the atoms in the pot is reduced.

4.6 Bulk magnetometry

Bulk magnetometry is volume sensitive measurement of a sample's magnetisation without being able to distinguish directly the contribution from each material of the layers in the sample.

From such measurements we can directly extract the coercive field of a sample and its saturation magnetisation. By calculating the expected magnetisation value from the density and magnetic moment per atom of the constituent layers of the sample, the total thickness of the sample layers can be measured.

For multilayer films, any "double-switching", where each layer changes magnetisation direction at different field values, can also be observed.

In conjunction with thickness calibration measurements, magnetometry can also be used to investigate the presence of magnetically dead layers in the sample. Using the density of the metal, the theoretical Bohr magneton per atom, and the volume of the sample, the expected saturation magnetisation for each layer thickness can be calculated. An example of this is shown in the inset of Fig. 4.10. As the Ni layer thickness increases, the saturation magnetisation per unit volume also increases linearly, indicating that there is no magnetically dead layer in these films.

‡ These cryostats are not technically "cryogen-free" despite being marketed as such; they still use liquid helium to cool samples, however the helium is recycled within the cryostat and when it boils it does not escape the system.

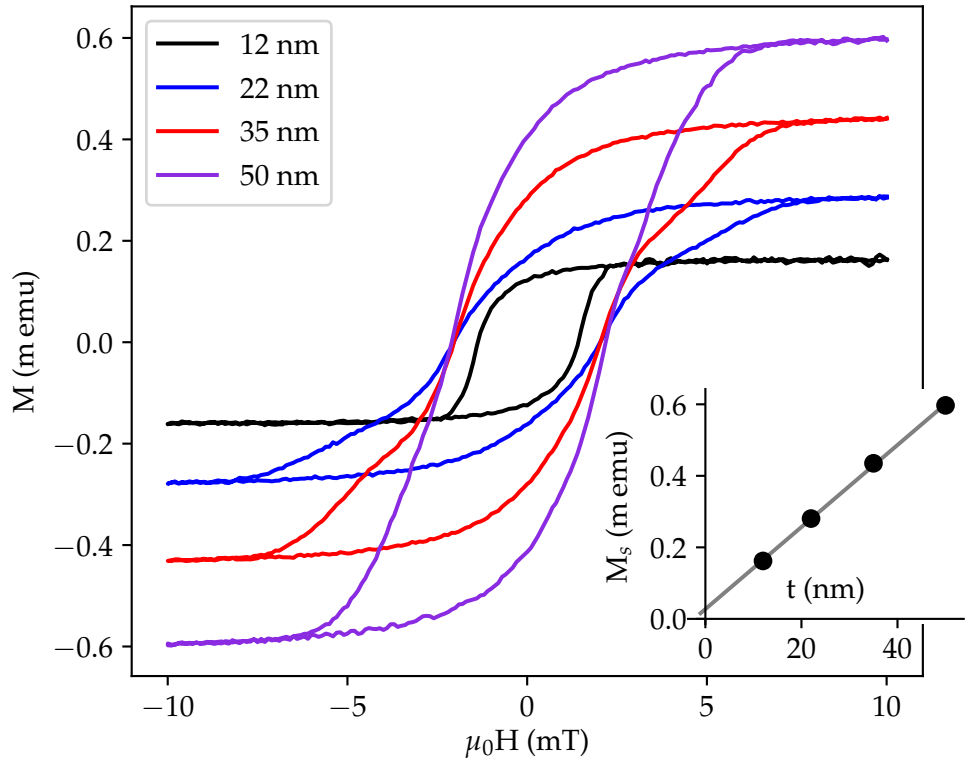

Figure 4.10: Room temperature $M(H)$ loops for different Nb/Ni/Nb thin films. The inset shows the saturation magnetisation (M_s) as a function of expected Ni layer thickness. Since the relationship is linear and the intercept is close to zero we can conclude that there is not a magnetically dead layer in the samples, since the effect would be more pronounced at lower thicknesses which would affect the linear relationship.

4.6.1 Room temperature VSM

A MicroMag™ by Princeton Measurement Corporation was used for room temperature vibrating sample magnetometry (VSM) measurements. A sample is mounted on the end of a non-magnetic rod, and positioned between the magnet poles. Attached to the ends of each of the magnet poles are a pair of counter-wound detection coils. The detection coils are mounted as counter-wound pairs so that any change in flux through them caused by variations in the applied magnetic field is cancelled out and not detected. The sample is vibrated by a piezoelectric oscillator at 83 Hz, and as it vibrates its external magnetic field enters and exits the top and bottom loops in turn. This creates an alternating electromotive force (EMF, ε) in the detection coils as a function of the rate of change of the flux through each coil: $\varepsilon = -d\phi/dt$.[94]

The water-cooled (non-superconducting) magnet could apply up to a 1 T magnetic field, and the pick-up coils were calibrated using a Co sample with a known saturation magnetisation supplied by NIST.

4.6.2 Low temperature VSM

VSM at low temperatures operates on the same principles outlined in the previous section (4.6.1), except these measurements were performed in a High Field Cryogen Free Measurement System by Cryogenic Ltd.; a cryogen-free cryostat with a VSM mounted in the sample space. The superconducting magnet can apply a field up to 9 T in the plane of the thin-film samples, and the cryostat can cool to 1.4 K. All bulk magnetic measurements at temperatures other than room temperature were made with this cryostat unless otherwise stated.

Chapter 5

X-ray magnetic circular dichroism

5.1 Ni/Gd/Ni system

The study presented here is a comprehensive examination of the TM/RE system, since no single study has hitherto approached the scope of this one. There are many previous results from other groups, but the combined effect of many small investigations is a fragmented view of the complete picture, and, at the very least, a view which is difficult to piece together from the literature.

The theoretical groundwork of RE/TM systems was established by Camley and Tilley;[29,95] they modelled RE/TM multilayers and found that due to the different Curie temperatures (T_C) of the RE and TM layers several phases occur as the effects of temperature and applied magnetic field are incorporated.* For given thicknesses of the RE and TM layers, at low temperatures the larger magnetic moment per atom of the RE layers contributes to a stronger coupling of the RE layer to an applied magnetic field, and it will dictate the behaviour of the coupled TM layer. As the temperature increases and the intra-layer RE coupling becomes weaker, meaning that the combined effect of the larger magnetic moments of the RE atoms loses dominance over the system, and the TM layer (with a much higher Curie temperature) will dictate the behaviour of the RE layer. The antiparallel coupling between the RE and TM layers ensures that when the RE layer is dominating the system and following the direction of the applied magnetic field, the TM layer will be antiparallel to both the RE layer and the field. This is termed the "RE-aligned" state, and the opposite case the "TM-aligned" state.

This simple picture was later confirmed experimentally,[30,37] and while the existence of a twisted state at the interface between bulk Fe and a thin layer of Gd (five atomic layers) was also predicted by Camley for certain values of the applied field,[28] this has not been conclusively demonstrated.

Due to the interface-driven nature of RE/TM systems it is difficult to measure the exact magnetic structures of the individual layers using standard measurement techniques such as VSM or magnetoresistance measurements.[77,96,97] Previous studies using XMCD have been performed and have mainly confirmed the predictions of Camley and Tilley: Barth *et al.* observed evidence of the transition between the RE- and TM-aligned state as a function of temperature in a Ni/Gd bilayer (7.5 nm and 5 nm thick, respectively),[37,38] while Koizumi *et al.* observed the same behaviour in a Gd/Fe $(2\,\mathrm{nm}/2\,\mathrm{nm})_{50}$ superlattice measured at 20 K and room temperature.[32]

*These models are also discussed in Sec. 6.1.1.

5.1.1 Experiment

Several different samples were measured by XMCD at SSRL.[98] The samples were grown by D.C. magnetron sputtering as described earlier (not on a heater), and all have the structure Si_3N_4/Nb/Ni/Gd/Ni/Nb. The top Nb layer is a capping layer to prevent oxidation and degradation of the active TM/RE/TM layer. The bottom Nb layer acts as a buffer layer between the Ni and Si_3N_4. The base pressure for all depositions was better than 10^{-8} mbar.

XMCD was measured for all samples, while XAS measurements were only performed on a selection and usually as part of the process of optimising the beam parameters.

In order to find out the magnetic states of the Ni/Gd/Ni samples, we measured hysteresis loops for all of them at both room temperature and $\sim$5 K. Since the hysteresis loops are effectively measuring the number of photons absorbed by a layer in the sample, if that layer is very thin, the number of photons absorbed can be very low and the data can be very noisy. Additionally, at the energy of the $M_{3,4}$ transition in Gd, we are pushing the limits of the capability of SSRL; the number of photons generated follows a bell curve as a function of energy, and the 1180 eV absorption peak is near the tail of the curve. Consequently samples with thin Gd layers were often too noisy to measure in detail. Time was another constraint, as beam-time at a large, national scale facility like SLAC is highly competitive. Table 5.1 shows which measurements were performed on each sample; the gaps being present due to the reasons cited above.

	Sample number																				
T (K)	1	2	3	4	5	6	7	8	9	10	11	12	13	14	15	16	17	18	19	20	T (K)
5	●	●	●	●	●	●	●	●	●	●	●	●	●	●	●	●*	●*	●*	●*	●*	5
10	●	●					●	●	●	●	●	●	●	●	●	●	●	●	●	●	10
15	●	●	●				●	●			●	●	●	●	●	●	●	●	●	●	15
20	●	●	●		●		●	●			●	●	●	●	●	●*	●*	●*	●*	●*	20
25		●	●				●	●					●	●	●	●	●	●	●	●	25
30	●	●	●				●	●			●	●	●	●	●	●	●	●	●	●	30
32.5			●																		32.5
35	●	●	●				●	●					●	●	●	●	●	●	●	●	35
37.5			●																		37.5
40	●	●	●				●	●			●	●	●	●	●	●*	●*	●*	●*	●*	40
42.5			●																		42.5
45	●	●	●				●	●					●	●	●						45
47.5			●																		47.5
50	●	●	●				●	●			●	●	●	●	●	●	●	●	●	●	50
52.5			●																		52.5
55	●	●	●				●	●					●	●	●						55
60	●	●					●	●						●†	●	●	●	●	●	●	60
65	●	●	●				●	●													65
70	●	●					●	●													70
75	●	●					●	●													75
80																	●	●	●	●	80
300	●	●		●	●	●†	●	●‡						●†		●*	●*	●*	●*	●*	300

Table 5.1: Temperatures at which samples were measured indicated by ●. * indicates out-of-plane measurements were performed, † indicates that only the Ni layers were measured at this temperature, and ‡ that only Gd was measured.

	Sample number										
Layer	S1	S2	S3	S4	S5	S6	S7	S8	S9	S10	...
Ni	3.6	2.5	3.9	2.7	3.7	2.4	6.5	4.2	2.6	2.9	...
Gd	11.4	4.6	6.0	2.6	21.5	11.0	20.8	11.1	6.2	6.1	...
Ni	3.6	2.5	3.9	2.7	3.7	2.4	6.5	4.2	2.6	2.9	...
	Thickness (nm)										

	Sample number										
...	S11	S12	S13	S14	S15	S16	S17	S18	S19	S20	Layer
...	1.4	1.9	3.1	3.8	2.2	5.9	10.8	5.2	6.0	3.7	Ni
...	8.2	6.2	7.9	11.1	9.7	9.9	8.8	17.2	3.1	5.1	Gd
...	1.4	1.9	3.1	3.8	2.2	5.9	10.8	5.2	6.0	3.7	Ni
	Thickness (nm)										

Table 5.2: Thicknesses of magnetic layers in all samples, measured by XMCD or XAS. Each sample has a capping layer and buffer layer of Nb, with thicknesses of 8 nm and 50 nm, respectively. The Nb layer thicknesses were not measured with x-rays.

Table 5.2 shows the thicknesses of all of the measured samples, as determined by XMCD or XAS. The top and bottom layers of Ni were grown to be symmetrical, and XMCD and XAS can only tell us the total thickness of both Ni layers combined. The values in the table then, are just this total thickness halved. If, elsewhere in the text, the thickness of a sample is only given as one value for Ni and Gd each, that value is the total Ni thickness.

5.2 Observed behaviours

All the samples that were measured fell into three categories of behaviour according to which element was aligned with the applied magnetic field at low temperature, and whether the alignment changed as the temperature was increased. Each behaviour is described below, along with an example of the data from a sample which displayed that behaviour. The full hysteresis data from each measured sample is shown at the end of the chapter.

5.2.1 Constant alignment

The first behaviour consists of a simple aligned state (either RE- or TM-aligned) which persists throughout the measured temperature range. Although some samples' Gd data is too poor to tell the Gd orientation direction, it is inferred to be antiparallel to the Ni orientation direction, and some noisy samples do nevertheless contain spurious indications that this is indeed the case. For example, S16's 25 and 30 K loops, and S18 10 K and upwards show small hysteresis loops embedded within the distribution of Gd x-ray intensity. The presence of recognisable hysteresis loops in some samples and not others could be due either to the thickness of the Gd layers, or to daily fluctuations in the beamline setup and optimisation or the x-ray beam current supplied by the synchrotron. This is also the cause of some inconsistencies in the Gd results as a function of thickness; since the overall signals

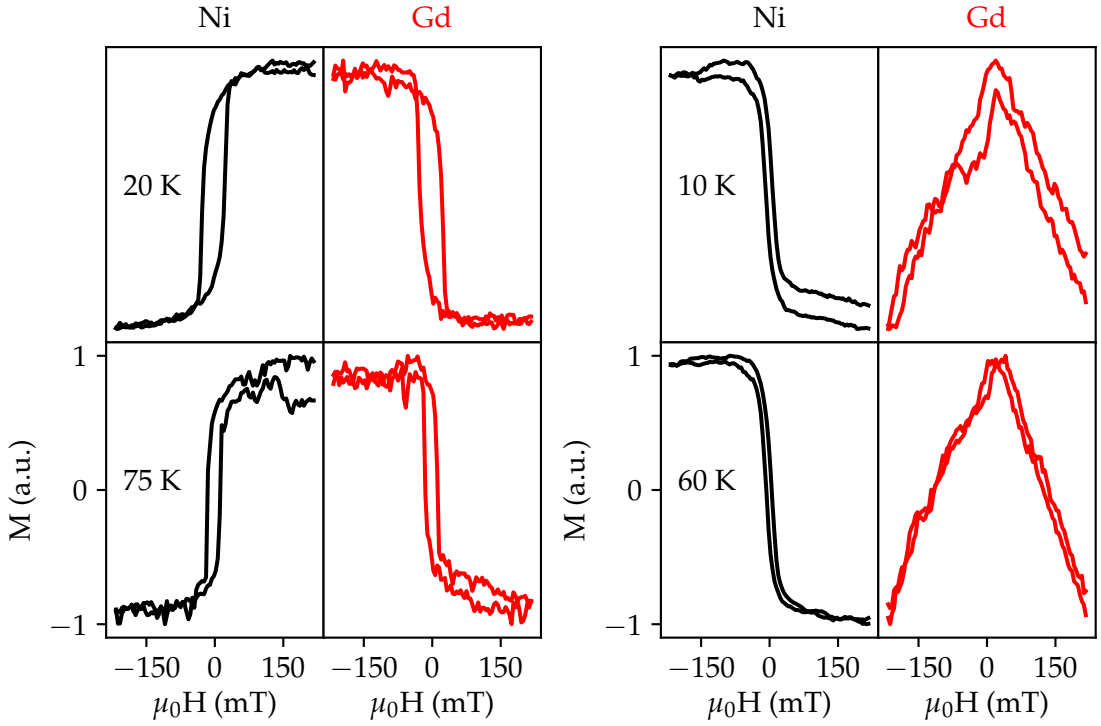

(a) Element-specific XMCD measurements of S2 at a range of temperatures. The sample structure is Ni/Gd/Ni (2.5/4.6/2.5 nm).

(b) Element-specific XMCD measurements of S16 at a range of temperatures. The sample structure is Ni/Gd/Ni (5.9/9.9/5.9 nm).

Figure 5.1

from the Gd layers are relatively weak, difficulties in equipment alignment can have pronounced effects on the measured signals.

A phenomenological explanation for this behaviour is that the antiparallel-aligned layer is too thin compared to the other layer to dictate the behaviour of the stack, regardless of temperature.

An example of the Ni-aligned state is shown in Fig. 5.1(a), and an example of the Gd-aligned state is shown in Fig. 5.1(b). Other samples showing this behaviour are shown at the end of the chapter in Figs. B.1, B.2, B.3, B.4, B.5, and B.6.

5.2.2 Switching alignment

The second behaviour is characterised by the sudden flip from the RE-aligned state to the TM-aligned state over a narrow temperature range. We can think of this as the influence from the two Ni interfaces with the Gd counteracting the ferromagnetic response of the Gd. As the temperature increases the relative strength of this interaction increases until it dominates over the Gd. This behaviour is seen in a relatively narrow range of sample thicknesses implying that a certain narrowness of layers prevents any inhomogeneity forming as the exchange interaction dominates the behaviour of each of the layers. However, the Gd has to be thick enough to dominate over the Ni at low temperatures.

This behaviour is the same as that described by the models of Camley and Tilley. Fig. 5.2 shows an example of this behaviour, and Figs. B.7 and B.8 show other

samples which displayed this behaviour.

5.2.3 Inhomogeneity

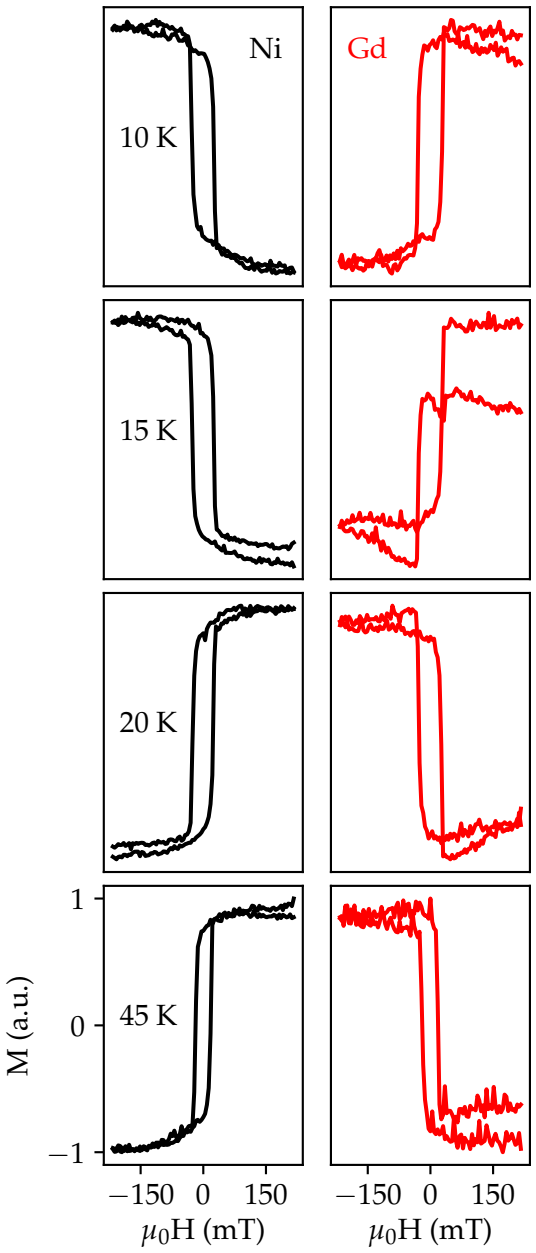

Figure 5.2: Element-specific XMCD measurements of S13 at a range of temperatures. The sample structure is Ni/Gd/Ni (3.1/7.9/3.1 nm).

The third behaviour is characterised by a number of features. The Ni, at higher fields at least, remains parallel with the applied magnetic field. However, at low temperatures and low fields, one gradual and one sudden transition take place from one magnetisation direction to the other. As the temperature increases, these transitions become less pronounced, until the whole hysteresis loop looks essentially conventional. At least in the case of one sample however, S3, small deviations can be seen in the hysteresis loop at the same field as the transitions even at higher temperatures.

Meanwhile, the Gd at low temperatures looks like a conventional hysteresis loop with a low coercive field, parallel to the applied magnetic field. As the temperature increases, the magnetisation at higher fields is no longer the highest magnetisation in the loop. The magnetisation at high fields decreases throughout the temperature range until at high temperatures the whole Gd loop is now antiparallel to the applied field. Throughout the transition too, the coercive field has increased.

Fig. 5.3 shows a phase diagram which can be constructed from the full temperature range of hysteresis loops and shows the evolution of the system as a function of temperature. To construct the phase diagram we take one branch from each of a normalised Ni and Gd hysteresis loop at a particular temperature. We then take the absolute difference between the two branches. If the Ni and Gd layers are parallel at a particular field value, both the curves will be at their normalised maximum or minimum, and the absolute difference between them will be 0 (shown in blue). If the two layers are antiparallel to one another at that point, one curve will be at the normalised maximum while the other is at the minimum, or vice versa. In that case, the absolute difference will be 2 (shown in red). This procedure is carried out for a hysteresis curve at every

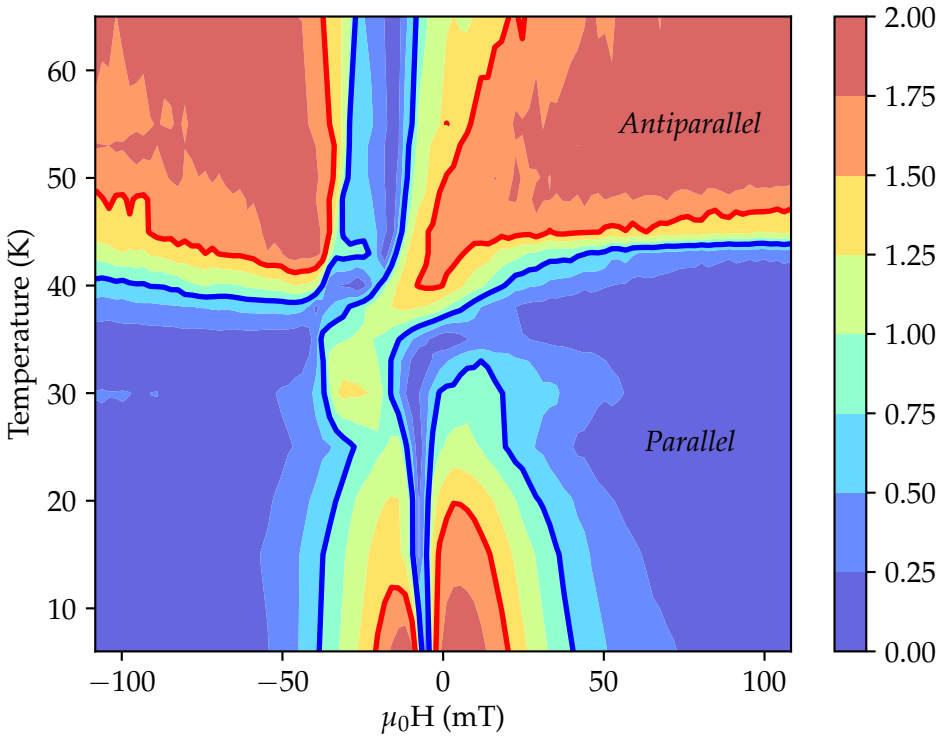

Figure 5.3: Experimental phase diagram of S3. The colour scale shows the absolute difference between normalised Ni and Gd hysteresis loops at the same temperatures. A difference of 2.00 (red) means that at that field value and temperature the Ni and Gd were at opposite saturation magnetisations and therefore completely antiparallel, while a difference of 0.00 (blue) shows that the Ni and Gd layers were aligned parallel to one another. A detailed explanation of the construction of this diagram is given in the text.

measured temperature value, and the results are stacked to create the phase diagram. In this way we can easily see the change in alignment between parallel and antiparallel as the temperature increases, as well as the transitions between states.

Fig. 5.4 shows the hysteresis loops which made up the experimental phase diagram, while the other samples which displayed this behaviour are shown in Figs. B.9, B.10, and B.11.

Note that not all of the samples shown were grown in the same growth run, yet the differences in behaviour transcend the different growth runs, so these behaviours cannot simply be explained by unique growth conditions.

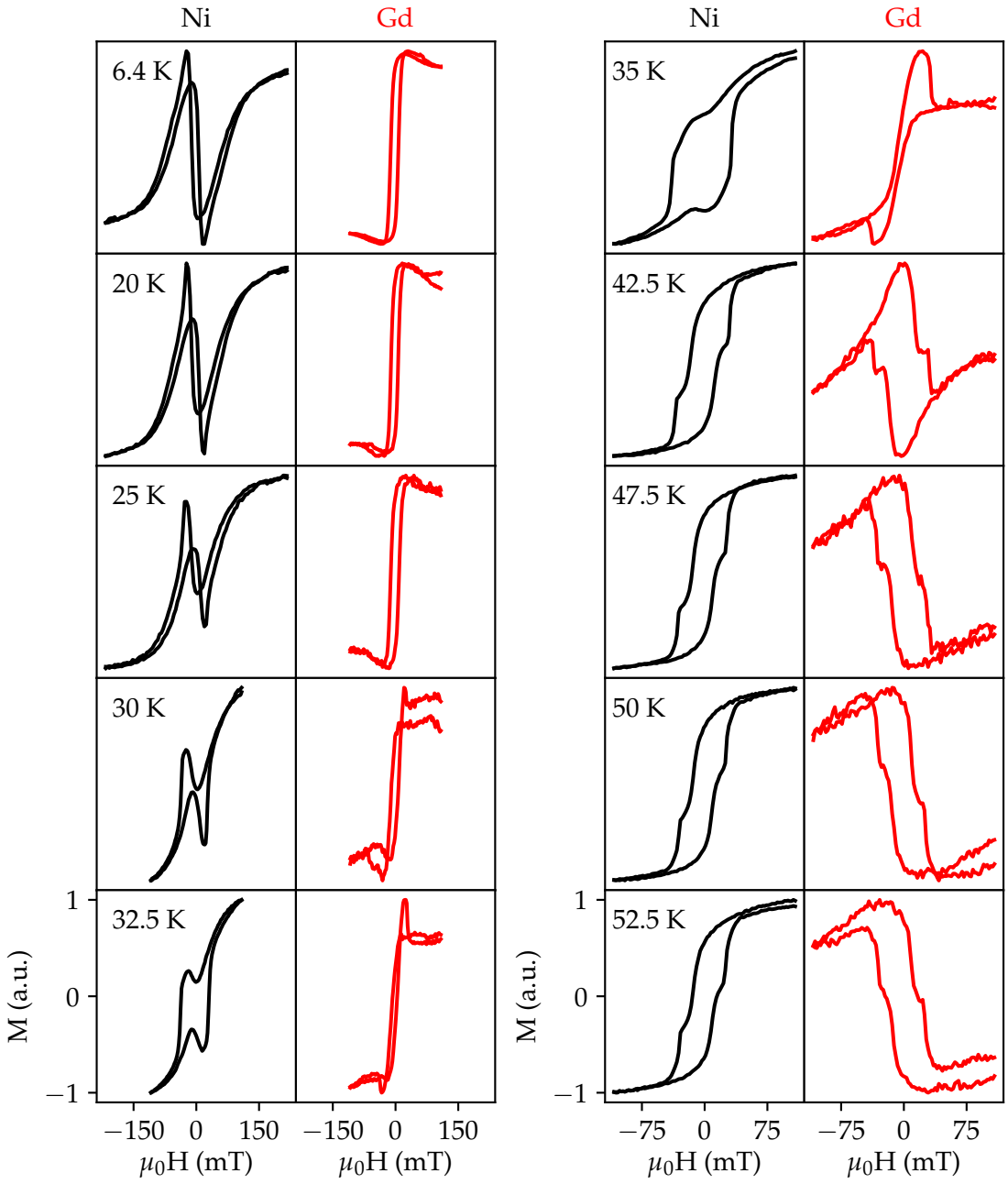

Figure 5.4: Element-specific XMCD measurements of S3 at a range of temperatures. The sample structure is Ni/Gd/Ni (3.9/6.0/3.9 nm).

Chapter 6

Model

The use of models in physics can be a double-edged sword. On the one hand, a model can provide useful insight into the behaviour of a complex system; on the other, a subtly wrong model can lull one into a false sense of knowledge security, or become a time-sink in a quest to perfect an imperfect model. Bearing this in mind, successful models are usually one of two types. The first is the highly detailed, highly accurate model. These models go to a lot of effort to take into account every single interaction in the system, and sometimes require fully-fledged computer scientists to write, maintain, and continually hone the ever-improving implementation. The Object Oriented MicroMagnetic Framework would be an example of such a model.

The second type is the modest yet useful type which tries to capture the essential behaviour of the system without having to get too bogged down in the details. The Ising model would be a very successful example of such a model. The simple model should almost be like an *ansatz*: ready to be discarded when it outlives its usefulness.

The model presented here tries to be simple, capture the complex behaviour that can arise from two competing energies in a system, while maintaining accuracy relevant to the system studied experimentally.

In this chapter, an introduction to the basic simple model of a ferromagnetic moment is given, as well as an introduction to similar models which have been used in the past to study either the RE/TM system or similar systems. The theory behind our model is then expounded, as well as a description of the implementation of the theory into software. The results of the model are presented, and linked to the experimental results of the previous chapter.

6.1 Stoner-Wohlfarth model

The Stoner-Wohlfarth model describes a simple, single-domain magnetic particle in a magnetic field. The particle has a uniaxial magnetic anisotropy (K_u), and therefore an easy axis (θ), measured with respect to the applied magnetic field (H).[99] The magnetisation of the magnet, M, is free to rotate in the plane of the easy axis and applied magnetic field, and the angle subtended is denoted by ϕ (also measured relative to H). The energy describing such a system is given by:

$$E = K_u V sin^2(\phi - \theta) - \mu_0 M_s V H cos(\phi), \tag{6.1}$$

where M_s is the saturation magnetisation, μ_0 is the permeability of free space, and V is the volume of the magnetic particle.

6.1.1 Similar models

In the 1980s Camley and Tilley (together and separately) were working on models of rare-earth and transition metal systems in various configurations, although mainly involving Fe and Gd. However, at the time, there was still disagreement within the community about the behaviour of the Gd moments; Weller *et al.* claimed that the first Gd layer at the Gd/Fe interface couples antiferromagnetically to the rest of the Gd,[26] in contrast to Taborelli *et al.* who argued that all of the Gd/Gd interactions in their system were ferromagnetic.[27] Camley is convinced by Taborelli's mean-field model, and applies this assumption in his model of five atomic layers of Gd on bulk Fe.[28] This model simulates bulk Fe by having the bottom out of 20 layers pinned in the direction of the applied field, while allowing the rest of the spins to rotate. The final angle of each spin is calculated by rotating it within the effective field produced by each of its nearest neighbours. (Only nearest neighbour interactions are considered.) While this model does include the effects of temperature on the system, it does not include anisotropy effects, noting that these effects should be less important in polycrystalline films.

Mauri *et al.* constructed a model which examined the case of a thin ferromagnetic film coupled to an antiferromagnet.[100] The thickness of the ferromagnet is less than the width of a domain wall in the ferromagnet so all the ferromagnet spins are aligned. They assume uniaxial anisotropy within the antiferromagnet, in a different direction from the alignment of the ferromagnet spins, and examine the effect the exchange coupling at the interface has on the spins within the antiferromagnet. Although the model does not incorporate the effects of temperature, and varies the sign of the exchange coupling at the interface, it mainly looks at one sublattice of the antiferromagnet so in some ways is quite similar to the FM/FM interaction we want to study.

6.2 New model

6.2.1 Overview

A number of other models from around this time (the late '80s) also incorporate a thin (rare-earth/transition metal) ferromagnet interfaced with a bulk (transition metal/rare-earth) ferromagnet, or look at superlattices made of very thin layers. The consensus is established, both experimentally and theoretically, that intra-rare-earth interactions are ferromagnetic, and rare-earth - transition metal interactions are antiferromagnetic.[29,95,97]

Given these other models, it may seem arrogant not to simply use them as they are. Why reinvent the wheel? However, none of these models on their own exactly capture the system we want to study. (Although there are aspects from the models we want to use, just not all present in the same model.) Another obstacle also presents itself; we are separated from the implementations by time, albeit only a few decades. However, the use of computers has evolved significantly since the 1980s. By writing a modern implementation that anyone can run on their own

computer our model can be more readily adapted to different situations*.

Our model incorporates magnetocrystalline anisotropy, the effects of temperature, and we use it to study a wide range of layer thicknesses. All systems we examine are of the form TM/RE/TM, where the TM-layer thicknesses are symmetric, as in the results presented in Chapter 5.

6.2.2 Modelled system

We represent our system as a vertical stack of single atomic layers, or equivalently a stack of magnetic moments. We call the vertical axis along which the stack is aligned z, and each moment in the stack is referenced by the index i. The moments rotate in the plane perpendicular to z, and a magnetic field is applied in one of the directions within this plane. The angle of each moment, ϕ_i, is measured with respect to the angle of this applied field, H. All of the moments are free to rotate, the only constraint applied is the antiparallel coupling at the interface, represented by the sign of the inter-layer exchange constant. Each moment interacts with its nearest neighbour via the exchange interaction, and inherits element-specific constants based on the definition of the elemental make-up of the stack. The energy of such a system is given by:

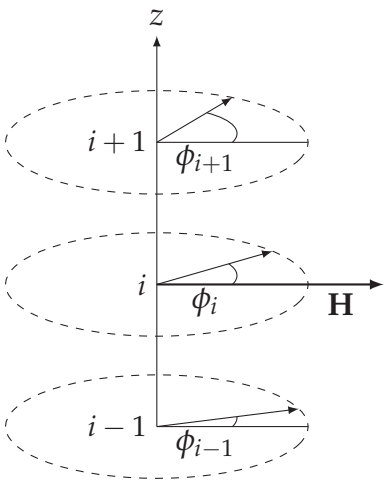

Figure 6.1: Diagram of part of the modelled stack of magnetic moments, represented as arrows. The moments are free to rotate in the plane perpendicular to z; the angle of rotation, ϕ, is measured with respect to the applied magnetic field direction, H.

$$\begin{aligned} E_i = &- g\mu_B\mu_0 M_i H\cos(\phi_i) + \frac{K_i}{n}\sin^2(\phi_i - \theta) \\ &- J_{i+1}S_{i+1}S_i\cos(\phi_i - \phi_{i+1}) \\ &- J_{i-1}S_{i-1}S_i\cos(\phi_i - \phi_{i-1}). \end{aligned} \tag{6.2}$$

The first term is the Zeeman energy, the second the magneto-crystalline anisotropy energy and the last two are the exchange energy terms of the moment interacting with the moment above and below, respectively. g is the Landé g-factor, μ_B is the Bohr magneton, μ_0 is the permeability of free space, M is the average magnetisation of the layer (in our case M is equal to the value of the magnetic moment of the atom for a perfectly ordered material), ϕ is the angle of a magnetic moment with respect to the applied magnetic field direction, K is the magnetocrystalline anisotropy energy, θ is the direction of the easy axis, n is the number density of the material of the layer, J is the exchange constant of the layer, and S is the magnitude of the magnetic moment of an atom in units of the Bohr magneton. We assume infinite extent of the ferromagnet layers in the x and y directions in order to neglect the effect of stray fields on the magnetic structure of the stack, and we include an easy

*A slightly future-proof version of the model is currently being implemented in Python 3, as opposed to the now deprecated Python 2 in which the original was written. All results presented here are from the original implementation. When the final implementation is finished it will be released open-access in the same repository as the data which was released to accompany the paper which first described the experimental results and the model.

axis in order to keep the model general rather than specific to our experimental system.

6.2.3 Temperature dependence

The equation given above does not take into account the effects of temperature on the system. In order for the model to be applicable to our experimental results, it would be useful to examine the variation of the state of the system as the temperature is increased.

First, we note the large difference between the Curie temperatures (T_C) of RE and TM ferromagnets. It so happens that Ni and Gd are both superlative in this respect; Ni has the lowest T_C of the TMs at 627 K, but this is still more than double that of Gd at 293 K, the highest of the RE ferromagnets.

This means that for measurements (or simulations) far below the T_C of Ni, the decrease of the average magnetisation of the Gd with increasing temperature will be significant, while for the Ni the change is negligible. As such, we incorporate the second-order phase transition into the expressions for M; $M \rightarrow M(T) \propto \tanh(T_C - T)$. However, when considering the *microscopic* exchange interaction between the adjacent layers we expect the strength of the interaction to be constant in temperature since the energy of this interaction depends only on the magnitude of the layers' magnetic moments. Therefore, this term is unchanged in our treatment for temperature.

Since each atomic layer in the model is only populated by a single magnetic moment, the values of M and S in the model will be equal. However, the behaviour of each of these terms will be different as a function of T. S represents the value of an atom's magnetic moment, which is unaffected by T, while M represents the average magnetisation of each layer. This is varied according to the function above. From Ref. 101 we assume that K varies with the cube of the magnetization (the uniaxial anisotropy case, $K \rightarrow K(M) = K_m M^3$), and so K will also vary with temperature.

The function minimization method used allows us to simplify the anisotropy energy term. Since the angle of the magnetic moment will always be close to the energy minimum, $E_{an} \propto \sin^2(\phi - \theta) \approx E_{an} \propto -|\cos(\phi - \theta)|$ (note the change in sign). To solve Equation 6.2 analytically, we consider the anisotropy energy term in two regimes when the above approximation is valid:

$$E_{an} = -\frac{K}{n}\cos(\phi_i - \theta) \text{ when } \phi_{min} < \frac{\pi}{2} + \theta \text{ or } \phi_{min} \geq \frac{3\pi}{2} + \theta \tag{6.3}$$

and

$$E_{an} = \frac{K}{n}\cos(\phi_i - \theta) \text{ when } \frac{\pi}{2} + \theta \leq \phi_{min} < \frac{3\pi}{2} + \theta, \tag{6.4}$$

where ϕ_{min} is the angle at which the total energy of the layer is minimum.

6.2.4 Implementation

The model has been implemented in Python 2.7. Several lists are constructed in parallel initially, one to hold values of ϕ, one for values of J for each i, and K, and so on. The length of each list is the number of moments in the stack, so as we cycle through the moments, we can easily look up the relevant parameters for that moment.

Since the energy calculation depends on the values of ϕ of the moment above and below the current moment, initial values of ϕ must be supplied for the calculation to start. Due to the hysteretic nature of the system, and therefore to avoid becoming trapped in local energy minima, the initial values of ϕ supplied are 0 and $\pi/2$. (This is important for our substitution for K to be valid.) By supplying realistic initial values for ϕ, the energy state of the system should move mostly continuously from one state to the next, without having the chance to jump to the non-global energy minimum.

For each temperature an applied field range is iterated through, and for each field value, the stack is iterated through[†]:

```
phi_check = phi_stack
for temperature in range(5,51,2.5):
    for field_value in range(-1,1,0.01):
        delta = [1] * len(phi_stack)
        while delta.max() > 0.001:
            for i in stack:
                phi_stack[i] = Min_Energy_Calc(
                        moment, field_value)
            delta = abs(phi_check - phi_stack)
        result[temperature][field_value] = phi_stack
```

where the function `Min_Energy_Calc` is of the form:

```
def Min_Energy_Calc(i, H):
    J_i = J[i]
    J_above = J[i+1]
    J_below = J[i-1]
    K_i = K[i]
    phi = result_of_calculation
    return phi
```

The `while delta.max()` line is a check to stop the energy calculation running forever once a solution has been found. The check subtracts the current stack values of ϕ from the stack values found from the previous iteration; if the largest of this list of differences is less than or equal to 0.001, the iteration is stopped and the current stack values are kept as the list of ϕs for that field value. If the "delta" is greater than 0.001, the iterations continue, with the check happening after each iteration.

Without a similar check on the number of iterations allowed, there is a possibility for the program to run in an infinite loop. This possibility can be countered in other ways, however. An emphasis elsewhere in the program to ensure local minima are

[†]In describing the implementation of the model, it is sometimes easier to use pseudocode rather than plain English. The pseudocode is syntactically similar, but not identical, to Python, and should be easy to interpret as an algorithm being performed.

eliminated in favour of a global minimum, for example. Without such checks it could be still possible for the system to switch between two equal minima.

The calculated values of ϕ are stored and can be retrieved later to plot vector diagrams of the system at particular field and temperature values. To construct hysteresis loops, the values of ϕ can be projected onto the applied field direction, and the resulting projection summed.

6.2.5 Caveats

As mentioned in the introduction, it is important to take into account the limitations of a simple model when examining its results. And due to the simplicity of this model, we cannot expect it to make accurate predictions about all aspects of the system. For example, we do not take into account stray fields in the model, so when comparing the model's results to that of measurements of the kind of mesoscopic multi-layered pillars which are common in superconducting spintronics studies, we should not be surprised if stray field effects are important and lead to differences.

We also do not attempt to take domains into account in the model. This can lead to numerical discrepancies between the predicted coercive fields given by the model, and those measured experimentally. This difference arises due to the Brown's paradox; a phenomenon of simple models that do not account for effects due to defects in the crystal structure and other nucleation points for disorder, corners being another example.[102–105] This means that the reversal of magnetic moments in the model requires higher fields than in the equivalent physical system. The paradox should not affect the results of the model in any way other than a scaling of the equivalent fields.

6.3 Results

6.3.1 Py/Gd system

As an example of the type of output we can get from the model, we first examine Py/Gd/Py system (Py, permalloy, is an alloy of $Ni_{0.8}$ and $Fe_{0.2}$). This is the system studied by Prieto *et al.*, who concluded from indirect measurements of the magnetic structure of the system that a domain wall was forming within the Gd. They built upon earlier theory by Inoue *et al.* and others who showed how domain walls in a multilayer structure would affect a current flowing perpendicular to the multilayer plane (CPP geometry).[106–108]

Fig. 6.2 shows some magnetic configurations thought likely in the Py/Gd/Py multilayers, and magnetoresistance results for structures with different Gd thicknesses. In the thickest samples, there is no measurable change in the resistance as a magnetic field is applied. According to the theory of transport across a domain wall, polarised carriers are scattered more by a narrower domain wall, i.e., by a higher rate of change of magnetisation direction within the sample. The change in magnetoresistance is highest for intermediate thicknesses of Gd, and when that thickness was measured at low temperatures, the change was highest at lower temperatures. These results are consistent with any domain wall present in the structure being dependent on the thickness of the Gd, and the interaction between the Gd and Py at low temperatures. The results are interpreted as the thinner samples constricting the domain wall within the Gd layer, so the domain wall

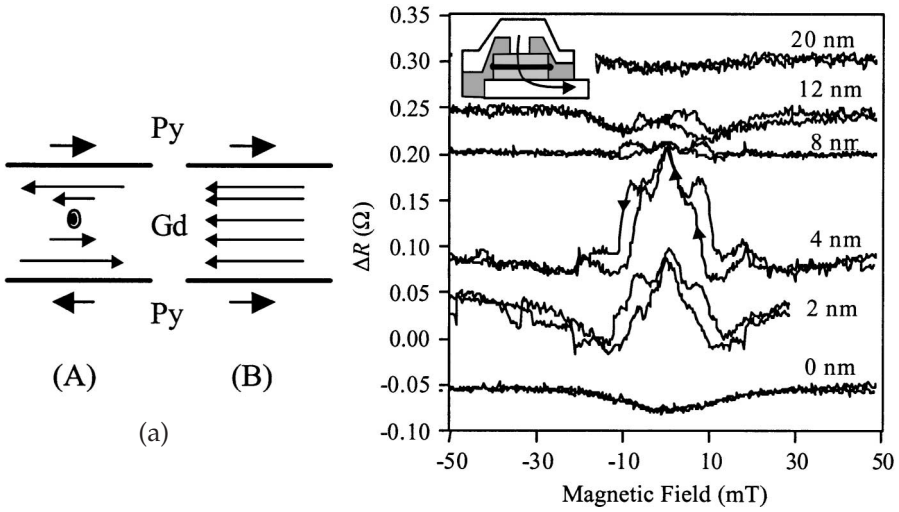

Figure 6.2: Results by Prieto *et al.* on Py/Gd multilayers. (a) shows magnetostatic energy reduction by the Gd layer forming a Bloch domain wall. This was presumed to be the magnetic structure in the devices which explained the results shown in (b). The graph shows that the increase in resistance of the devices are maximised for specific thicknesses of Gd. The current flows through all the magnetic layers of the device, and so was presumed to be flowing through the kind of Bloch domain wall shown in (a). The device structure was Py/Gd/Py, with Py thicknesses of 100 nm, Gd thicknesses are shown in the graph. From Ref. 77.

would be more tightly wound and hence the ΔMR would be higher. Below a certain thickness however, the Gd rotates more coherently, lowering ΔMR.

Fig. 6.3 shows element-specific $M(H)$ loops over a range of temperatures extracted from a modelled Py/Gd/Py system with thicknesses 3.5/7/3.5 nm. These hysteresis loops alone demonstrate the complex magnetic behaviour of the system. We can see that at low temperatures, the Py and Gd layers have parallel saturation magnetizations, and both are parallel to the applied field; however, at higher temperatures, the Gd has rotated at saturation and has a component of its magnetization antiparallel to the applied field and the Py layer, indicating a competition between the Zeeman energy and interfacial exchange energy.

Fig. 6.3 also shows the micromagnetic structure at different points in the field cycle. Following from negative saturation to positive, we can see the competition between the Zeeman energy term trying to align the bulk of the Py and Gd parallel to the applied field and the antiferromagnetic exchange coupling which leads to a twist in both the Py and Gd close to the interface. As the applied field decreases the exchange coupling dominates and the Py magnetization rotates away from the field. Next, as the Gd magnetization flips as the field direction reverses, the Py is dragged round to remain antiparallel to the field before the Zeeman energy term becomes more dominant again.

We now examine the results from our own model of a similar system to that studied by Prieto *et al.* Fig. 6.4 shows element-specific $M(H)$ loops at 77 K for two Py/Gd/Py multilayer systems. For simplicity, we have assumed that above some Py thickness threshold, extra Py layers will have a smaller and smaller influence on

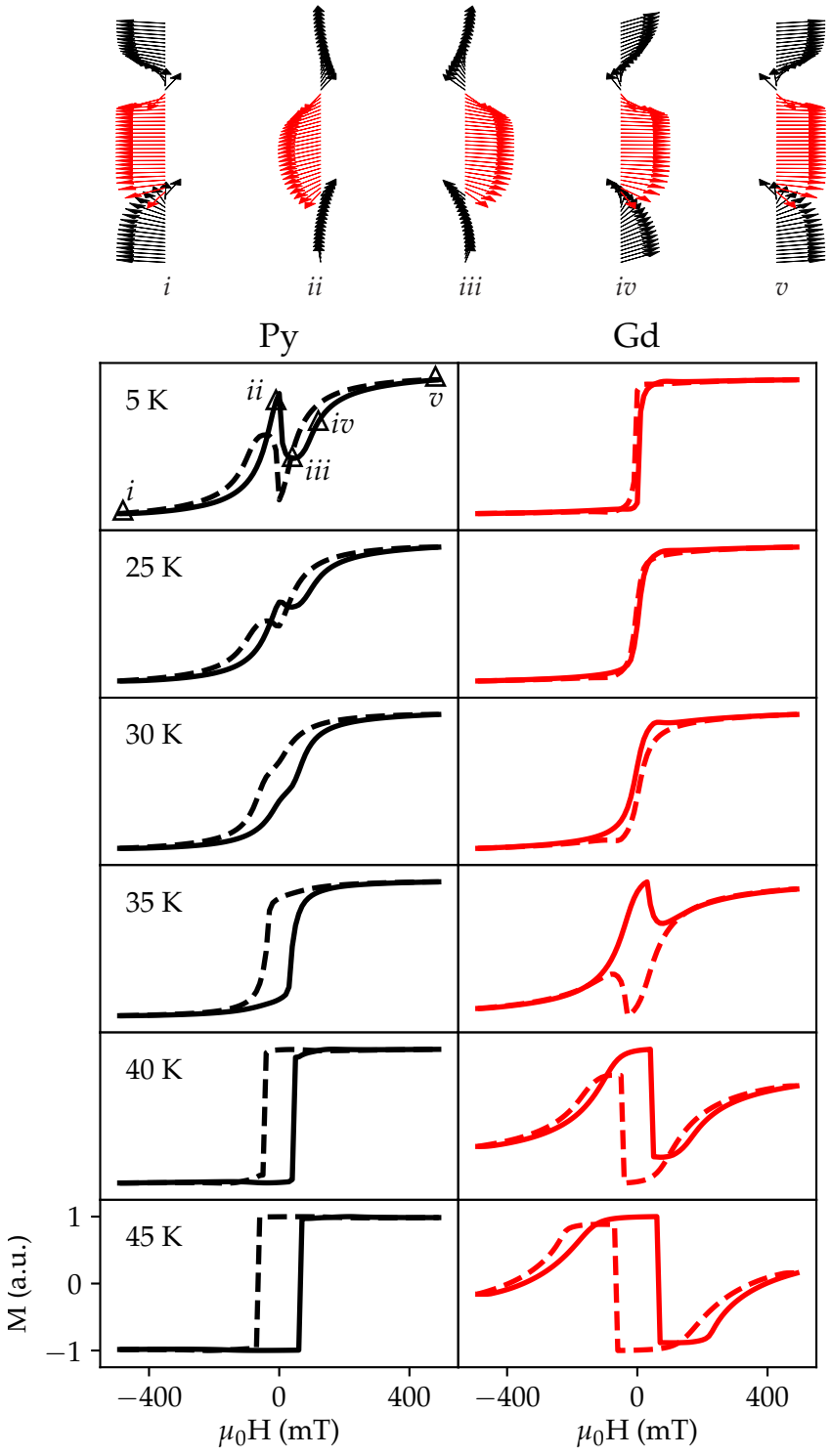

Figure 6.3: Top: Vector diagrams (*i* - *v*) showing the micromagnetic structure of a Py (3.5 nm)/Gd (7 nm)/Py (3.5 nm) at the indicated applied field value. Bottom: Element specific $M(H)$ loops of the same multilayer at various temperatures.

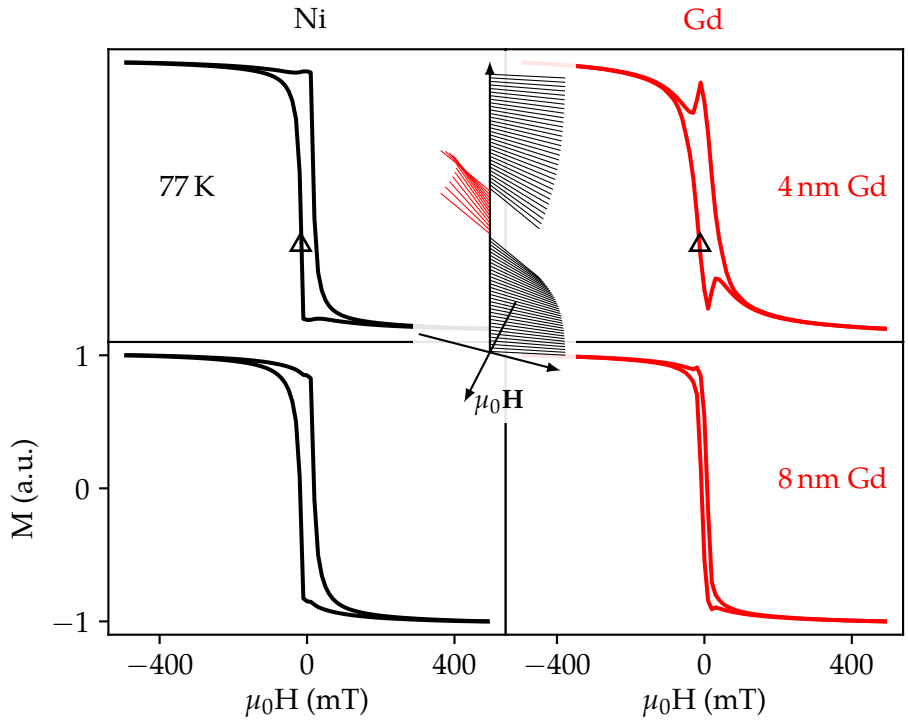

Figure 6.4: The results of the model for a Py/Gd/Py multilayer, with Py thicknesses of 40 nm, and Gd thicknesses of 4 and 8 nm (top and bottom in the figure). These thicknesses are similar to those studied by Prieto *et al.* The inset shows the micromagnetic structure of the stack (with 4 nm of Gd) at the field value indicated by a triangle on the hysteresis loops (the uppermost and lowermost Py layers are not shown).

the Py/Gd interface, especially since the model only considers nearest-neighbour interactions. So although the Py layers in the model are 40 nm thick rather than Prieto's 100 nm, this should be sufficiently thick, and the Gd layers are 4 and 8 nm in each sample, the same as two of Prieto's samples. The inset arrow diagram shows the magnetic moment configuration at the field value indicated by a triangle, which tells us that similar inhomogeneity is present in this structure as was found in the results shown in 6.3, although this structure is no longer present in the samples with thicker Gd layers. Therefore, our model disagrees with the interpretation of a simple Bloch domain wall in the Gd layer. However, our theoretical results are still consistent with their experimental results. The current flowing through the devices will respond to any continuous magnetic inhomogeneity, so the experiment cannot distinguish between a domain wall only located within the Gd and the inhomogeneity we see at each Gd/Py interface. Additionally, our model would predict the same dependence on Gd thickness as was found in the experiments. So our results are consistent with the measurements taken by Prieto *et al.*, and their experimental method was not able to distinguish between their interpretation and the one provided by our model.

To investigate the results of the model in more detail, we now consider the effects of varying the thickness of the Py and Gd layers. Only one stack with particular Gd and Py layer thicknesses is shown in Fig. 6.3. However, by varying

the thickness of the Py and Gd layers in the structure, we see different regimes of behaviour emerge. Figs 6.5(a) and 6.5(b) capture two of these regimes. In (a) the cosine of the difference in angle between the bulk and interface Py moments is calculated for each field value in one branch of an $M(H)$ loop over a range of temperatures. A contour separates two magnetic states that emerge. At low temperatures and high fields a domain wall (DW) is present in Py, which disappears at low fields and at higher temperatures. The structure represented in this phase diagram is the same as that shown in the vector diagrams of Fig. 6.3(b)(i - v). The symbol "AP" in the diagram shows the areas where the Py and Gd are antiparallel without an inhomogeneity.

Fig. 6.5(b) shows a similar state diagram as in (a) but for a thinner sample (Py (1.25 nm)/Gd (2.5 nm)/Py (1.25 nm)) and constructed in a slightly different way so as to show the different behaviour. This diagram shows the cosine of the difference between the angle of the Py spin and the angle of the applied magnetic field. At low temperatures, the Py is forced to be antiparallel to the field due to the coupling between the Gd and the applied field and its antiferromagnetic coupling to the Py (Py_{AP}). At higher temperatures the situation is reversed and the Py follows the applied field (Py_P). The contour is offset from zero field at higher temperatures because the field has been swept in only one direction to produce the diagram. This transition is the same type as that observed by Barth *et al.*, from a Gd-aligned state to a TM-aligned state.

6.3.2 Ni/Gd system

Having seen that the model can predict quite complex hysteresis loops, we now use it to examine the behaviour observed in Section 4.4. We turn first to the physical sample for which we have the most data, and that which displayed the richest hysteresis loops, S3 (Fig. 5.4). The modelled version of S3 is shown in Fig. 6.6. We can see that the model shows complicated Ni hysteresis behaviour: an "N"-shaped loop at low temperatures, transitioning to a conventional hysteresis loop shape at higher temperatures. At saturation, the Ni appears to be aligned with the applied field. The Gd starts with a conventionally shaped hysteresis loop at low temperatures, with a low coercive field, transitioning to an antiparallel-to-field hysteresis loop at higher temperatures, and with a higher coercive field.

This matches closely what was observed in the XMCD experiment. With the addition of the model though, we can extract the vector positions of each layer in the model and show the angle they subtend with respect to the applied field to generate the hysteresis loop.

At 6 K and high fields, we expect the majority of moments in both the Ni and Gd layers to be aligned parallel with the applied field direction. However, if the interfacial antiparallel coupling is maintained, there must be some moments canted away from this direction (seen in the vector diagrams marked with a square). Indeed, the model enforces strict antiparallel coupling at the interface, and the fact that the magnetisation at the maximum applied field is not the highest magnetisation measured in both the Ni and Gd loops supports this experimentally. The angle of the moments canting away from the applied field direction are highest at the interface, and due to the intra-layer exchange energies the angle changes continuously to allow the moments to align with the bulk further away from the interface. As the applied field is lowered the exchange energies dominate over the Zeeman energy and the change in angle of moments as a function of the distance

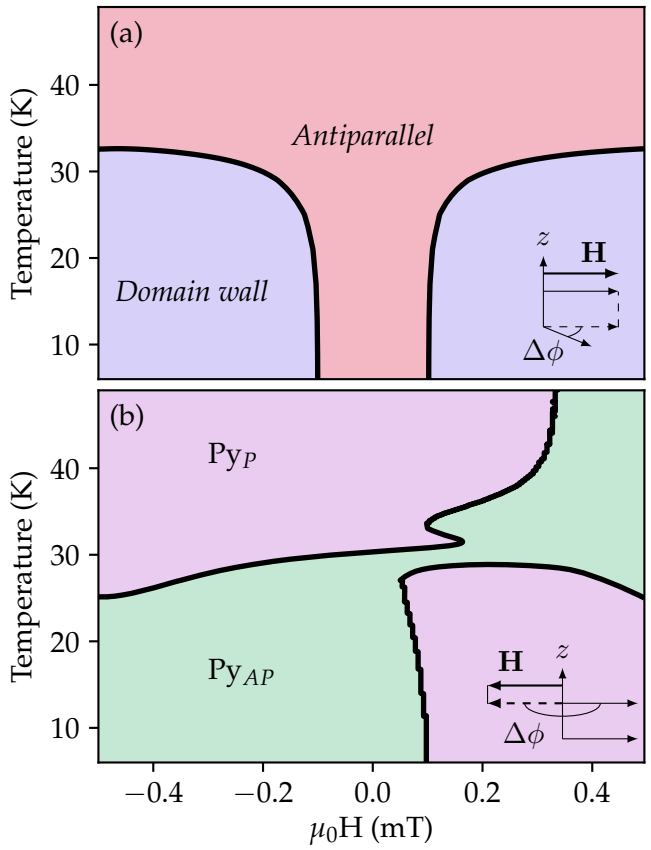

Figure 6.5: Magnetic state diagrams showing two regimes of behaviour in multilayers with different thicknesses. In (a) the contours show the cosine of the difference between the angle of the bulk Py spins and the interfacial Py spin. Areas marked DW (domain wall) show a twisted Py state, while AP (antiparallel) areas show homogeneous Py that is antiparallel to the Gd. In (b) the contours show the cosine of the difference between bulk Py spins and the direction of the applied magnetic field. Py$_{AP}$ marks areas where the Py is antiparallel to the applied field (and the Gd parallel), while Py$_P$ marks areas where the reverse is true. The layer thicknesses are (3.5/7/3.5 nm) and (1.25/2.5/1.25 nm), in (a) and (b), respectively.

from the interface is reduced (seen in the vector diagrams marked with a circle). This means that either the Ni or Gd are forced to align mostly antiparallel to the applied field due to the influence of the interfacial coupling. At low temperatures the Gd couples more strongly to the field and so forces the Ni to align antiparallel to both the Gd and the field. This is reflected in the hysteresis loops; as the field strength is decreased the magnetisation of the Ni decreases to negative saturation as the bulk Ni moments are forced by the intra-layer exchange energy to follow the Ni moments which are closest to the interface with the Gd. Then, as the field crosses zero, the Gd moments flip, following the field, and the Ni moments also all flip as shown by the sudden reversal in the hysteresis loop from negative to positive saturation (shown in the vector diagrams marked with a triangle).

As the temperature increases, the reversal of Ni becomes less pronounced due to a lowered influence of the Gd (Gd has a Curie temperature less than half that of Ni), and vanishes altogether by 50 K. Correspondingly, the Gd begins to display similar signs to those that the Ni displayed at low temperature; sudden magnetisation reversals that do not follow the direction of the applied field. This indicates that more of the Ni moments will be aligned with the field at high fields and higher temperatures, and we can see from the corresponding Gd loops that the Gd is for the most part completely under the influence of the Ni and remains antiparallel to both the Ni and the applied field for the majority of the applied field range. This

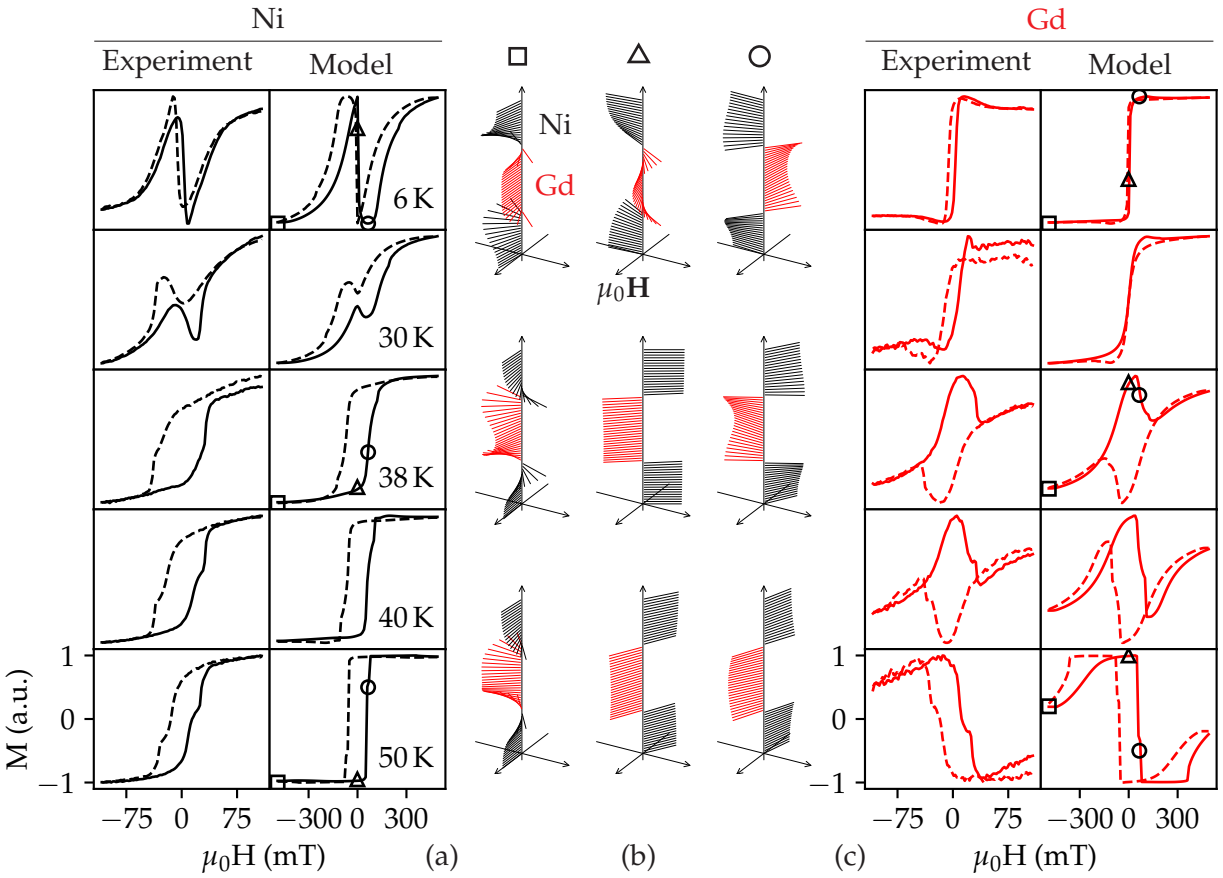

Figure 6.6: Comparison between the results of the model and the XMCD experimental results for sample S3. (The same thicknesses were used in the model as are present in the experimental sample.) (a) and (c) show the hysteresis curves produced by the experiment and model for Ni and Gd, respectively, for various temperatures. (b) shows the vector representation of the output of the model at specific temperatures and specific applied field strengths indicated on the graphs by the square, triangle and circle. At low temperatures and at high fields, the inhomogeneity at the Ni/Gd interfaces is maximised, whereas the opposite is true for higher temperatures and low field values. At the higher field values, the Zeeman energy plays an important role in driving competition between the exchange energies, while at higher temperatures the Gd is close to its Curie temperature and behaviour of the whole stack is more determined by the Ni layers.

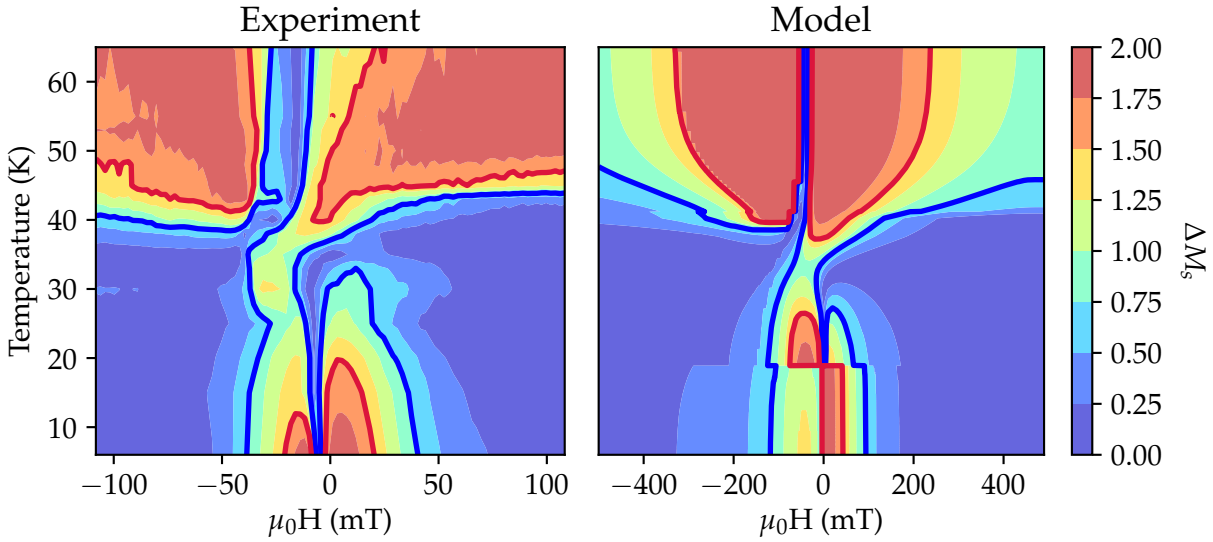

Figure 6.7: Phase diagrams showing the degree of inhomogeneity present in an experimental and theoretical multilayer as a function of applied field and temperature. Left: The phase diagram as constructed from experimental hysteresis loops by taking the difference between the normalised magnetisation of Ni and Gd at each field value in a loop. This is then repeated for every temperature. Right: A phase diagram constructed in the same way as that in (a) but from theoretical hysteresis loops.

also explains the coercivity of the Gd growing to match that of the Ni at higher temperatures. Any magnetic inhomogeneity that was present at the interface at lower temperatures has vanished for the most part.

The only other major studies on the Ni/Gd system using an element-specific technique are those undertaken by Barth *et al.*,[37] who also used XMCD. However, the main aim of their study was to investigate the effects of deposition temperature and substrate on Ni/Gd bilayers. The introduction of a second Ni/Gd interface in our structures brings with it a slight increase in complexity, although bilayers would be interesting structures to study with the model.

Barth did observe an antiparallel alignment of the Ni and Gd layers, and a step-wise rotation of the Gd layer. This may not be consistent with the continuous region of inhomogeneity predicted by our model. The system behaves as if the Gd layer is made of two decoupled layers, one more influenced by the Ni interface than the other. We'll call these the "interfacial" layer and the "bulk" layer. At high fields, the Ni is aligned with the field, as is part of the Gd, presumably our hypothetical "bulk" layer. As the field is reduced below zero, and at small negative fields this bulk layer switches with the field, and is now also antiparallel to the Ni layer. When the Ni layer flips, it also induces the interfacial Gd layer to flip too, so once again the two Gd layers are antiparallel to one another.

Barth's measurements during the growth phase of the bilayers indicated that Gd was growing in islands, so he posited that the Ni layer was filling in these gaps before smoothing over the surface. It is known that such undulations in the interface between ferromagnets can lead to interesting effects, including an effective exchange bias due to this so-called "orange-peel" coupling.[2,109]

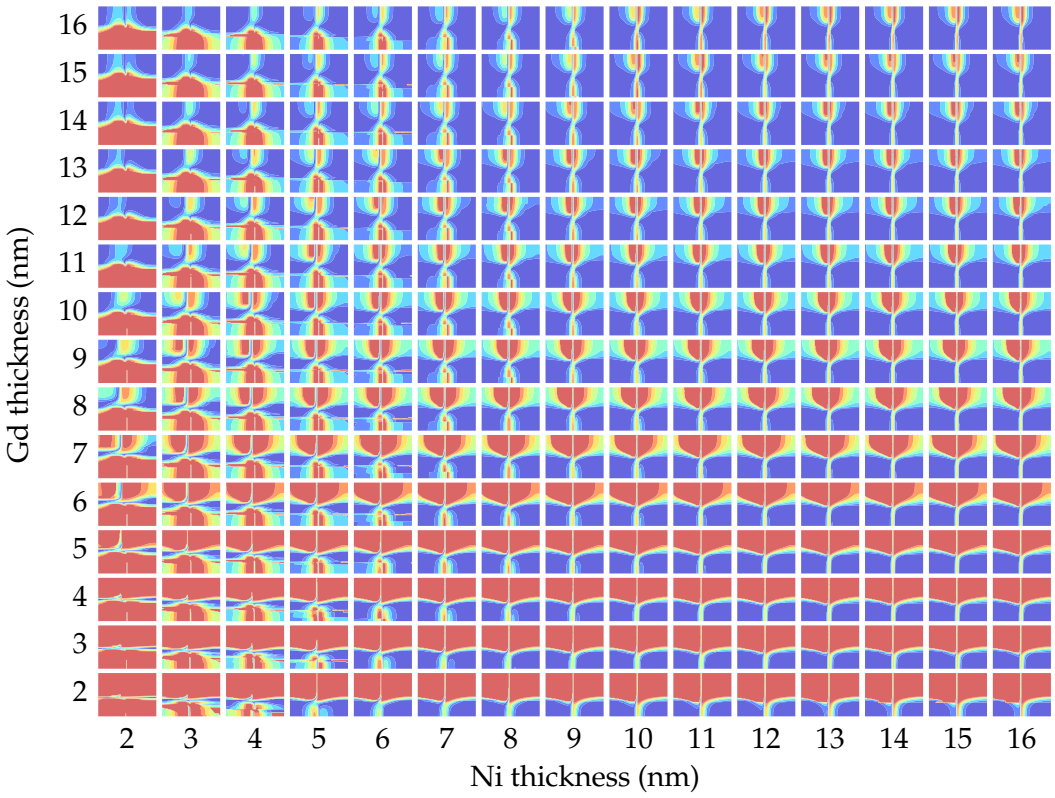

Figure 6.8: Phase diagrams generated by the model as a function of Ni and Gd thickness. The colour code is the same as before, where red shows antiparallel alignment between the Ni and Gd layers, and blue parallel. We can see clear regions where inhomogeneity should be expected, for example when the Gd and Ni (total) thicknesses are both 7 nm. However at the corners and edges of the diagram few samples would show inhomogeneity.

Our model assumed a perfect interface between the Ni and Gd and produced a good match with our experimental results, however, a study of the interfaces grown in our deposition chambers would still be beneficial.

Summary Considering the Ni/Gd/Ni results as a whole we see that due to the number of samples studied, each with a different thickness, and the temperature range through which most of the samples were studied, we now have a comprehensive picture of the behaviour of the system, and, thanks to the model, a great insight into the magnetic microstructure of the system. The interplay between the exchange energies within the system and the Zeeman energy from an applied magnetic field lead to rich magnetic textures at the interfaces within the structure. These textures are interesting in their own right, but, as we will explore in the next chapter, can also be exploited in spin valve devices.

As always, more work could be done investigating the system. Sometimes due to time constraints not every sample was investigated throughout the full range of temperatures possible, however beam-time at a necessary facility is extremely competitive and we tried to fully utilise the time we had available to us. Some other features of the data could not be avoided due to the physics of the synchrotron,

such as the high noise levels in some of the Gd data, however this only could have been solved by using a different x-ray source.

In order to more closely align the model with the experiment an investigation of epitaxially grown structures would be beneficial, however this is rendered difficult by the requirement of growing the structures on substrates which are transparent to x-rays. Such a study would tie into the further work mentioned above of also studying the interface between the Ni and Gd.

Chapter 7

Spin valves

This work follows on from the results presented in Section 3.2.2. Many designs of superconducting spin valves have previously been reported, and those designed with spin-triplet supercurrents in mind all utilise magnetic inhomogeneity of some kind. Josephson junction-based devices must be nanofabricated in a way to ensure the supercurrent must pass through the magnetically active layer. The measurements are then performed in the current-perpendicular-to-plane configuration. All of the results presented below use the alternative method, current-in-plane. In this way thin films can be used as grown and without requiring extensive processing.

7.1 Exchange biased samples

Based on the results of previous chapters showing the rich variety of inhomogeneous magnetic textures available in the Ni/Gd system, a spin valve was designed to utilise the inhomogeneity. For better control of the magnetic behaviour the Ni was exchange biased by $Fe_{0.5}Mn_{0.5}$*. In this way, by pinning the Ni layer and flipping the Gd layer from parallel to anti-parallel to the Ni, inhomogeneity can be introduced and erased. According to the results above, the inhomogeneity will be maximised when the moments furthest from the Ni/Gd interface are parallel to one another (i.e., the "bulk" moments in the Ni and Gd layers), and minimised when the bulk Gd moments are antiparallel to both Ni layers' bulk moments.

First, it was shown that 10 nm of FeMn grown on various thicknesses of Ni will alter the values of $\pm H_c$ of the Ni. Fig. 7.1 shows the room-temperature VSM measurements of a variety of thicknesses of Ni with FeMn grown on top. All of the samples are exchange biased to some extent, with some even having both H_{c1} and H_{c2} the same sign.

One of the samples is biased in the opposite direction from the other three samples. Since none of the samples was grown in a magnetic field, the direction of the bias is essentially random between the two directions of the easy axis of the long, thin samples.

All of the samples were grown at room temperature on SiO_2 with buffer and capping layers of Nb. In the thinnest samples, the diamagnetic contribution from the SiO_2 can be seen; indeed, the effect becomes less pronounced as the thicker layers of Ni begin to dominate the behaviour of the system.

*For an overview of exchange bias, see Sec. 2.6.1

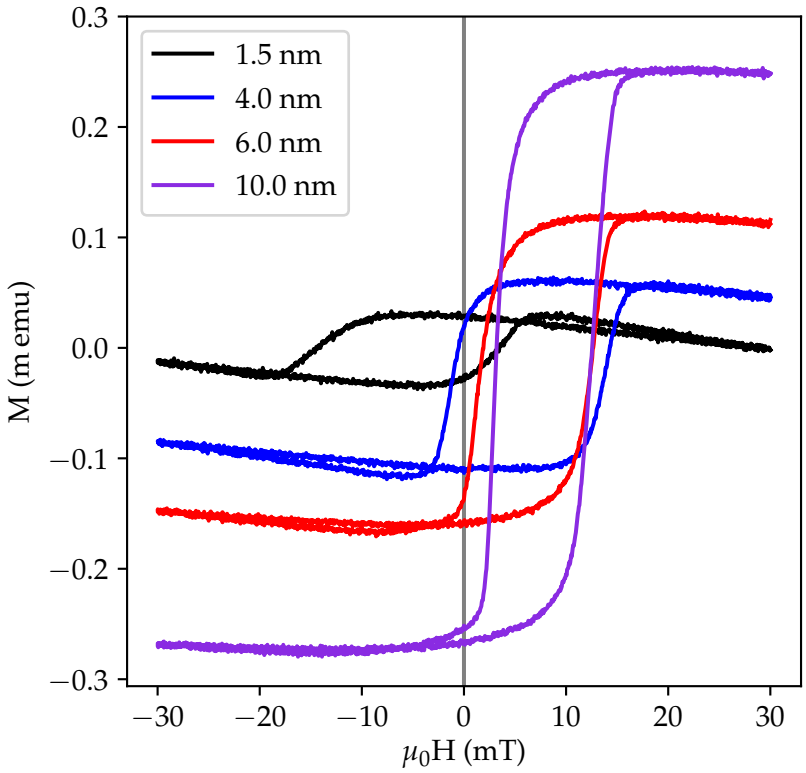

Figure 7.1: Room temperature $M(H)$ measurements of Ni thin films exchange biased by 10 nm of FeMn. Ni thickness is shown in the legend. The samples were grown on SiO_2 with buffer and capping layers of Nb.

After the exchange biasing of the Ni layer had been established, a layer of Gd was added to the structure. The active layers[†] of the structure are then grown as follows: Nb/Gd/Ni/FeMn.

Fominov *et al.* showed that inhomogeneity at the F/F′ interface in such a structure generates spin-triplet pairs, which can "leak" from the superconducting layer suppressing the critical temperature.[68] If we assume that the magnetic layers far away from the Nb layers in our sample can act as a triplet-pair sink, either by acting as a spin sink, or due to some decoherence or spin unmixing, then we would expect the T_c of our sample to decrease when the inhomogeneity in the sample is maximised. This would be the case when the Ni and Gd layers are aligned parallel to one another, at least, far from their shared interface. In the opposite case, when the Ni and Gd are antiparallel to one another, there will not be any inhomogeneity at the interface, and the exchange fields in both layers will be strongly uniform, suppressing spin-triplet generation and suppressing any spin-singlet penetration into the magnetic layers.

There are differences between our system and that considered by Fominov and others however.[110,111] It is usually assumed that the source of inhomogeneity in these spin valves simply arises from non-collinear coupling at the interface of the two magnetic layers, however, our inhomogeneity is rather more elaborate than that.

[†]I.e.: excluding the substrate and capping layers.

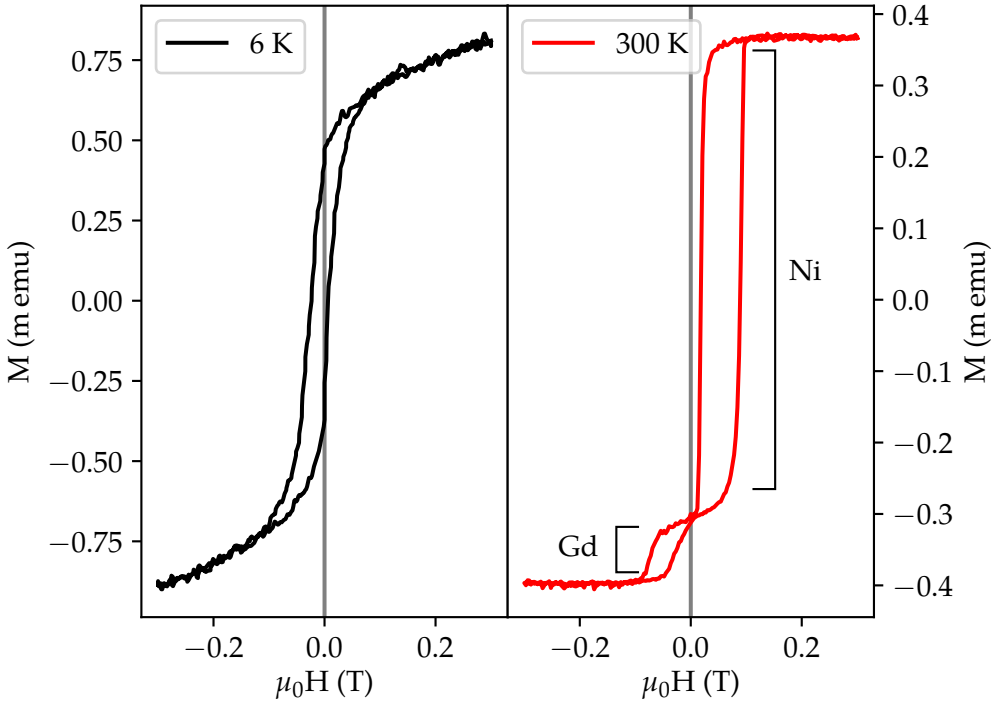

Figure 7.2: Ni/Gd sample exchange biased by 10 nm of FeMn, measured at room temperature (right) and low temperature (left). The sample structure was Nb/Gd/Ni/FeMn/Nb with thicknesses (30/5/15/10/10 nm). The labels on the room temperature measurement show the switching of the Ni and Gd as well as the relative sizes of the contributions to the overall saturation magnetisation.

Fig. 7.2 shows the anticipated double switching of one sample grown with this structure. However, the double switching is only observed at room temperature. On the right hand side of the figure, the room temperature measurement, we can see that the Ni makes up the majority of the magnetic response, and is clearly exchange biased. At high positive field the Ni and Gd are both aligned parallel to one another and the field, except for any inhomogeneity at the interface. As the field is reduced, the Ni switches due to the exchange bias from the FeMn. As the field strength is increased in the opposite direction the Gd also switches until both layers are parallel again at high negative field. As the negative field strength is reduced the Gd switches at low fields due to the effective exchange bias from the Ni. So the Gd response is very similar to that of the Ni, whereas while the Ni has been exchange biased by the FeMn, it appears as if the Gd has been exchange biased in the opposite direction by the Ni, due to the antiparallel exchange coupling at the Ni/Gd interface. The Gd near the interface will compensate the rest of the Gd which behaves nearly paramagnetically, lowering the overall response of the Gd.

On the left hand side of the figure, the low temperature measurement at 6 K, the Gd response dominates over that of the Ni, and any evidence of the exchange bias of the Ni is gone. We can see that the overall saturation magnetisation has increased which we can attribute to the Gd since it was so close to its Curie temperature during the room temperature measurements. Even though the Gd is 3 times thinner than the Ni layer, at low temperatures it should contribute nearly

4 times the saturation magnetisation than the Ni. For the sample size and layer thicknesses, the saturation magnetisation of this structure should be 0.87 m emu with a contribution of 0.19 m emu from the Ni and 0.7 m emu from the Gd. The inhomogeneity at the interface will decrease this expected value slightly, but we can see that the magnetic response of the structure will be dominated by the contribution from the Gd at low temperatures. This structure therefore becomes unviable as a spin valve candidate. The Ni layer needs to be thin enough for the interface with the FeMn to play a significant role in its magnetic response, but the ratio of the Ni and Gd layer thicknesses needs to high enough to prevent the Gd overwhelming the thin Ni layer.

Another feature precludes this structure from use. Even if the room temperature behaviour had persisted to low temperatures, the double switching displayed at room temperature is frustratingly the wrong kind of double switching. For a spin valve to work effectively, it must maintain the two states, parallel and antiparallel, at remanence. An applied magnetic field needed to maintain one of the states affects the T_c of the superconductor. To eliminate this effect, spin valves measurements usually involve the following procedure:

- A large positive (for example) field is applied to put the system in the parallel state.
- The field is removed, and the T_c is measured.
- A smaller negative field is applied to put the system in the antiparallel state.
- The field is removed, and the T_c is measured.

For this procedure to work, the two sweeps of the hysteresis loop in opposite directions must have different intercepts with zero field. We can see this is not the case with this structure, so the parallel and antiparallel states would not have been able to be maintained at remanence.

Although the Ni/Gd system was shown to display suitable magnetic inhomogeneity for spin-triplet generation, the bilayer studied here is perhaps not the ideal design for a spin valve since the maximum inhomogeneity occurs when both layers' magnetisations are parallel to one another. Usually, opposite exchange fields are desirable for spin-triplet generation; after all, the spin-singlets need to penetrate the ferromagnet enough to be affected by the inhomogeneity, so strong suppression from an exchange field would lower the efficacy of the device.

Finally, Fig. 7.2 is a good example of the differences between the measurement equipment used for room temperature and low temperature VSM. The noise level is noticeably higher in the low temperature VSM, and it has problems changing the sign of the applied field.

7.2 Ni/Gd/Ni samples

Due to the delicate nature of the Si_3N_4 membranes on which the samples measured by XMCD were grown, in each run identical samples were grown on SiO_2 as well. These samples could be characterised more easily without risk of breaking the Si_3N_4 windows. Two of the samples displayed double switching behaviour at room temperature when measured by VSM, shown in Fig. 7.3 Again, although measured above the T_C temperature of Gd, the exchange coupling from the ferromagnetic

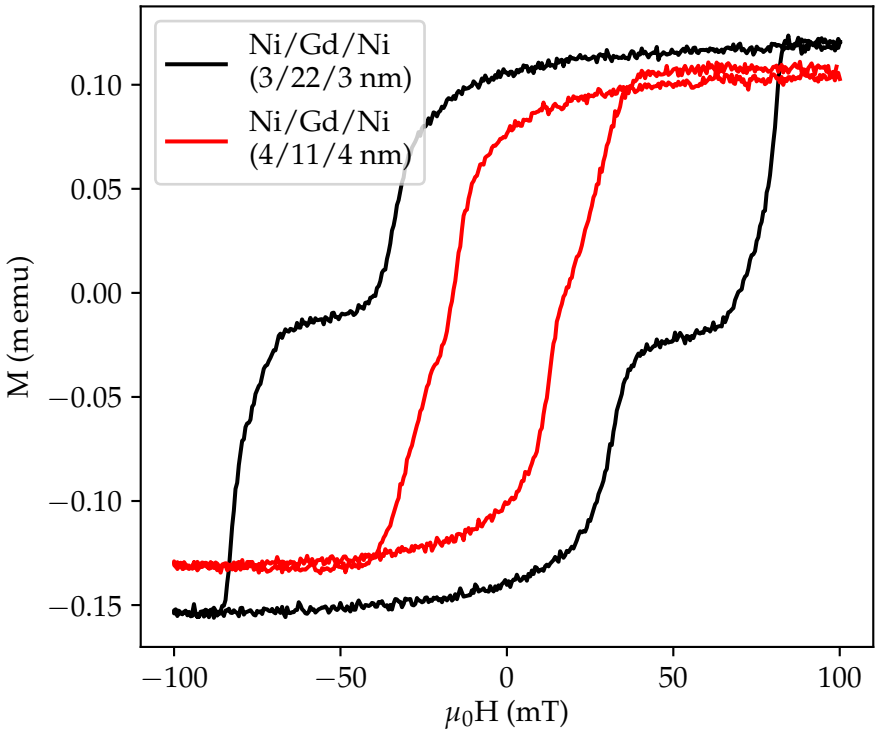

Figure 7.3: Room temperature hysteresis loops of two samples grown in parallel to those measured by XMCD, but grown on SiO_2.

Ni induces ferromagnetism in the Gd, and, unlike in the exchange biased samples discussed earlier, these samples contain two Ni/Gd interfaces.

Despite the clear double switching observed in these samples, they are not suitable as spin valves because the samples grown for XMCD have a 50 nm thick buffer layer of Nb. Similar structures were therefore grown in order to utilise the observed double switching. The samples were grown at room temperature on SiO_2. Although the (3/22/3 nm) sample in Fig. 7.3 shows the clearest double switching at room temperature, the new samples were instead based on "S3" from the XMCD data, since that sample showed the maximum inhomogeneity at low temperatures. The room temperature hysteresis loops for these samples are shown in Fig. 7.4.

The low temperature transport measurements for one of the samples is shown in Fig. 7.5. The measurements were performed according to the procedure outlined in Sec. 7.1. A clear difference in the T_c between the parallel and antiparallel state can be seen, although the difference is only of the order of tens of millikelvins. Other recent spin valve designs have obtained a ΔT_c of hundreds of millikelvins.[76]

A possible reason for this comparatively poor performance was outlined in the previous section. The design of this spin valve relies on the magnetic inhomogeneity arising from the antiparallel exchange coupling at the Ni/Gd interface, but this is maximised when the two layers magnetisations are parallel to one another. If the net exchange field within the Ni layer adjacent to the Nb is high in the parallel state, Cooper pairs which could potentially be converted to spin-triplet pairs if they are affected by the inhomogeneity are suppressed too quickly; they cannot penetrate far enough into the Ni. If this is the case, this effect would have the opposite effect from the desired effect in the parallel state, minimising ΔT_c.

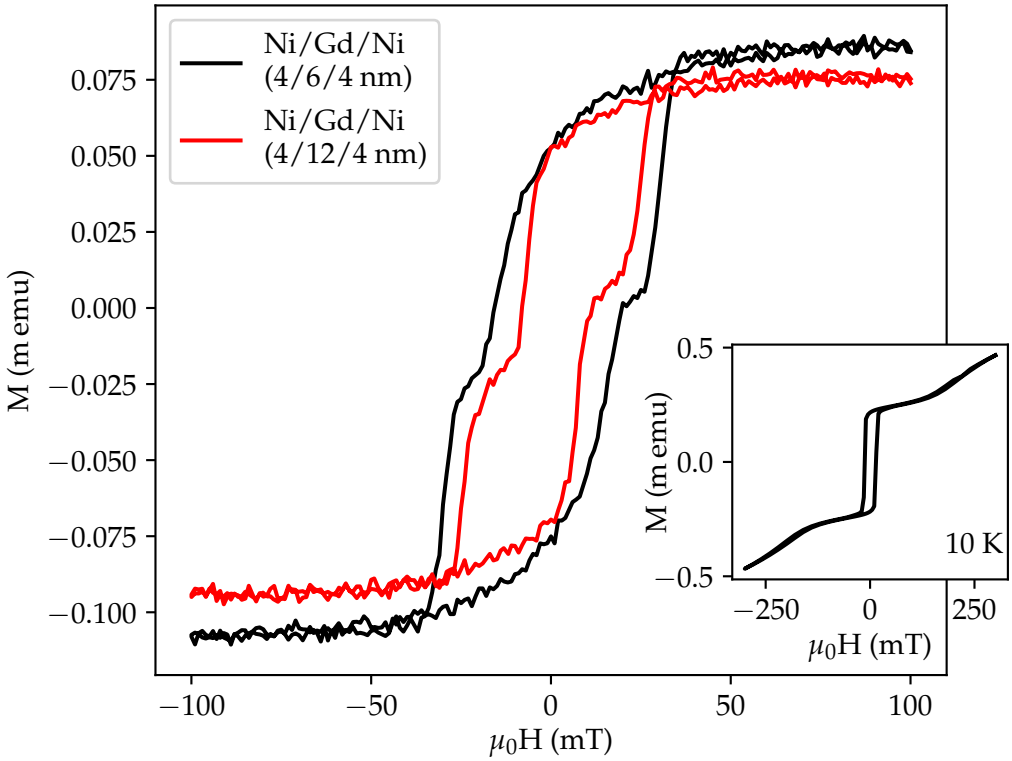

Figure 7.4: Main: Room temperature hysteresis loops of two samples with the same structure as those measured by XMCD showing double switching. Inset: Low temperature (10 K) hysteresis loop of the (4/6/4 nm) sample. These samples have a Nb layer of 30 nm at the bottom.

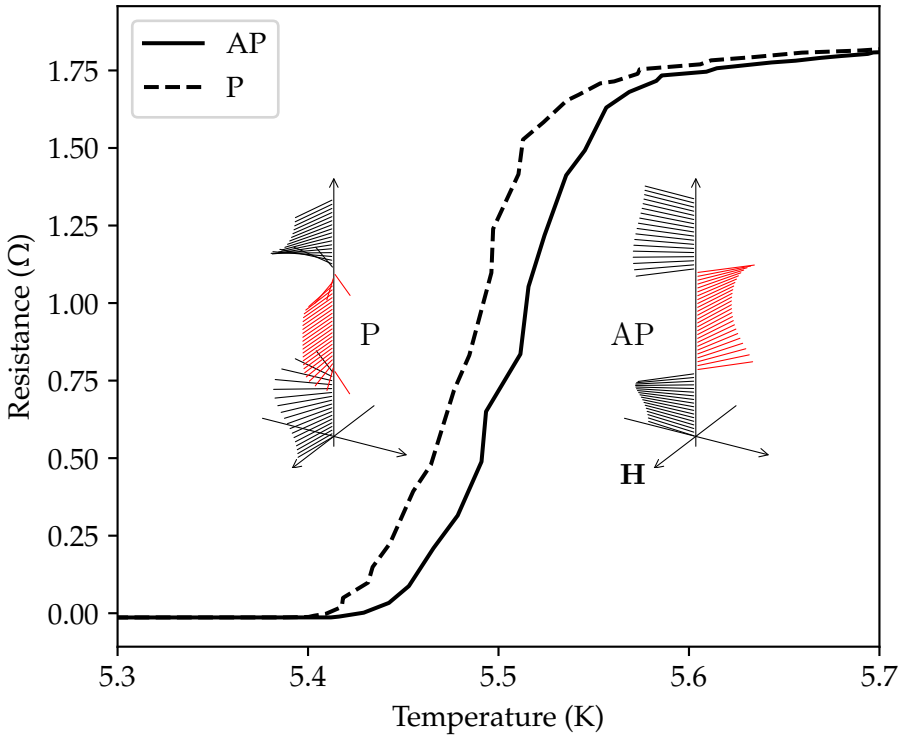

Figure 7.5: T_c curves taken in zero field after applying 80 mT (parallel, P) and −30 mT (antiparallel, AP). The sample is the same as that shown in Fig. 7.4, with thickness Ni/Gd/Ni (4/6/4 nm). The diagrams show magnetic configurations in the P and AP states to illustrate the difference between the inhomogeneous and more homogeneous states. The diagrams are made with the results from the model.

7.3 Ho/Gd-based structures

7.3.1 Previous work

A single-crystal sample of Ho, when cooled in zero magnetic field will enter an antiferromagnetic phase at 133 K, although with a helical magnetic structure. When cooled further to around 20 K, the previously basal plane helix transforms into a conical helix; the moments rotating out of plane by 10°. If a magnetic field is then applied, the sample enters a conventional ferromagnetic phase which remains unless the sample is then heated above 133 K again.[18,19,75,112–114] These transitions are shown in Fig. 7.6. One would think these helical and conical phases in Ho are perfectly suited for generating spin-triplet superconducting pairs. Indeed there is extensive experimental[73,74,115] and theoretical[116–118] work confirming this view, although some of the experiments were successful even with polycrystalline Ho.

Gu *et al.* have studied Ho-based structures in two configurations. In the first, a simple Nb/Ho bilayer, the Ho was transitioned from a virgin conical magnetic state to a ferromagnetic state.[75] The change in the critical temperature of the Nb was larger than previously reported values for conventional spin valves, at $\Delta T_c = 130$ mK. However, the change between the two magnetic states is only quasi-reversible; to revert to the conical state from the ferromagnetic state requires heating the sample up. Spin valves typically work simply by changing the applied magnetic field.

Later results were on Ho/Nb/Ho spin valves. These devices again showed a much larger irreversible ΔT_c than had previously been observed in spin valves, but also a much larger reversible ΔT_c.[76] In this case the devices were cooled and would enter the conical state, and after a magnetic field had been applied and the Ho became ferromagnetic, the two Ho layers could be switched independently due to having difference coercivities from the two layers' different thicknesses. This meant the device could reversible switch between the parallel and antiparallel states. In this case the reversible $\Delta T_c = 400$ mK was obtained. To rule out any effects from the out-of-plane component in the conical state of the Ho, the same devices were made with Dy which does not enter the same conical state, and the same reversible effects were observed. The results from both of the Ho-based devices are shown in Fig. 7.7. Ho, therefore, shows great promise as both a spin-mixer to transform

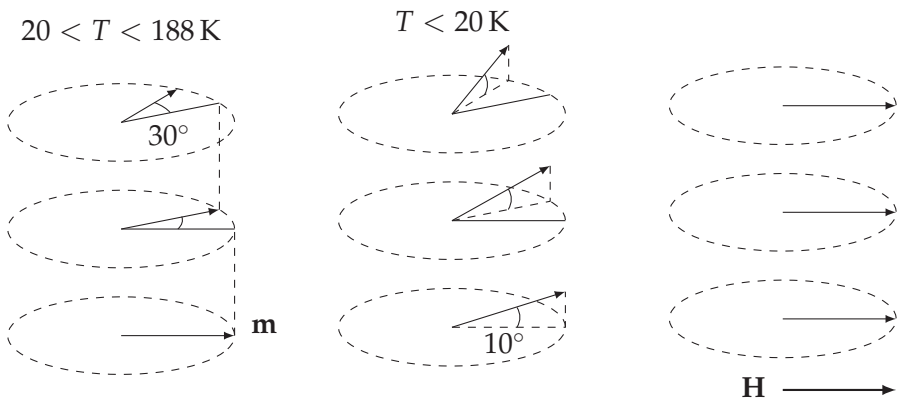

Figure 7.6: The magnetic phases of Ho when cooled in zero field (left and centre), and the ferromagnetic response when an external magnetic field is applied.

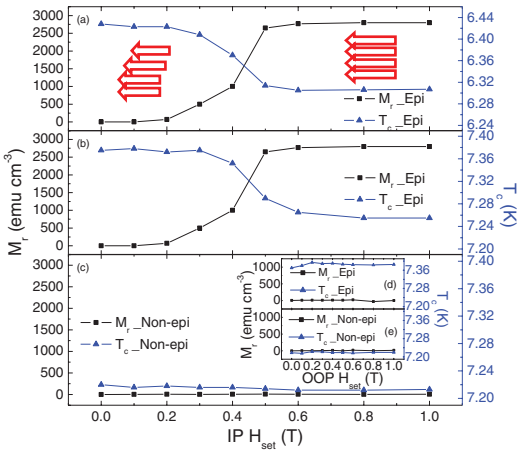

(a) Irreversible changes to the critical temperature of an epitaxially grown Nb/Ho bilayer. The Ho was 12 nm thick in all cases, and the Nb was 24, 30, 15, 20 and 15 nm thick for (a) to (e), respectively. The T_c is highest when the Ho is in the conical state, and lowest in the ferromagnetic state. To reverse the change in T_c, the device must be heated back to ∼20 K. From Ref. 75.

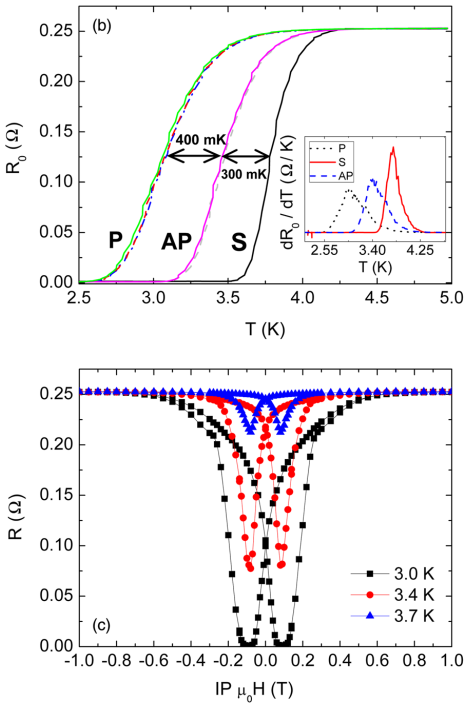

(b) A 700 mK irreversible ΔT_c in a Ho/Nb/Ho (10/20/40 nm) trilayer (from the spiral state to the antiparallel state), and a reversible 400 mK change from the parallel to the antiparallel state. This device relies on the independent switching of the two layers which have different coercivities. From Ref. 76.

Figure 7.7

spin-singlet pairs into spin-triplet pairs, and as an active layer in conventional spin valves.

7.3.2 Results

Nb/Ho/Gd samples were grown at high temperature on a-plane sapphire, with a capping layer of Nb. The samples were grown at high temperature to encourage epitaxial growth due to the uniqueness of the magnetic behaviour of epitaxial rather than polycrystalline Ho. Deposition procedure is given in Sec. 4.2.1. From one run of samples with thicknesses 35/10/20 nm, measurements from one sample are shown below. The sample was characterised by x-ray diffraction, shown in Fig. 7.8. The sample appears epitaxial, although the Ho and Gd peaks are very close together and have therefore merged. The Ho has grown predominantly in the (002) direction although a peak remains at the (100) direction; unfortunately a peak for the sapphire substrate is also very close to that peak so deconvolution of the two seems extremely difficult.

Fig. 7.9 shows low temperature $M(H)$ measurements of the sample (4 K). The grey, dotted loop shows a hysteresis loop taken from the virgin state, i.e., cooled from room temperature in zero field. The central dotted line shows the

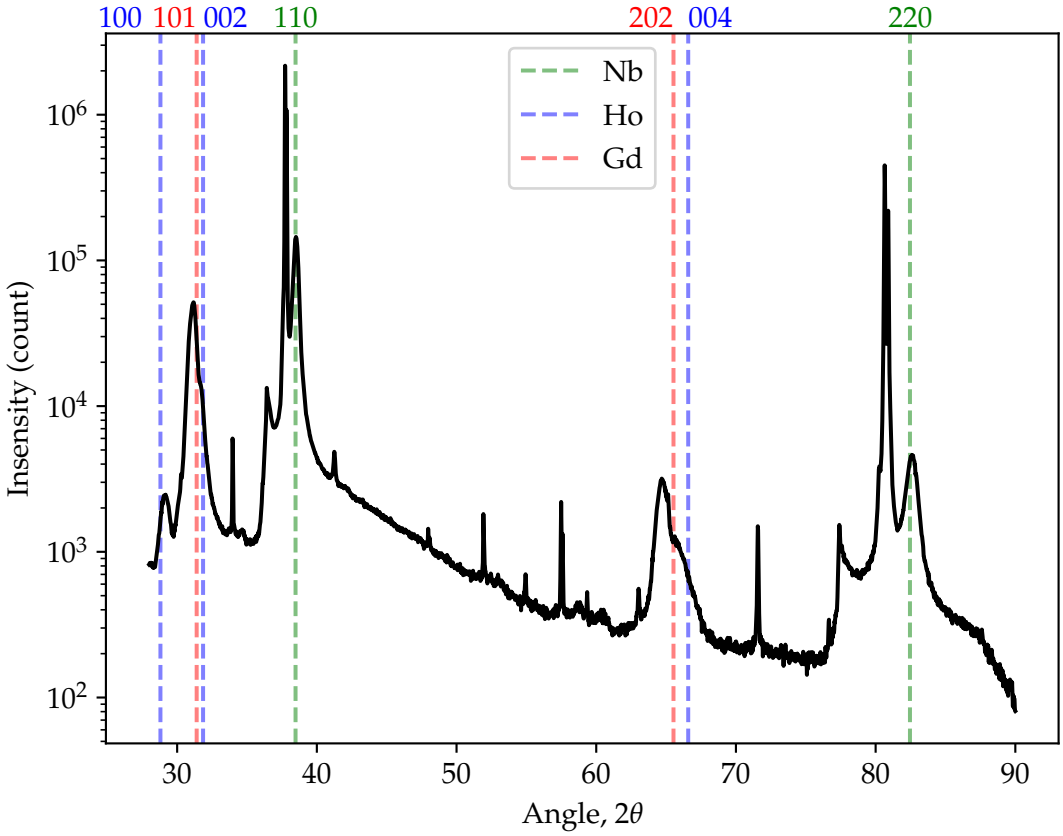

Figure 7.8: X-ray diffraction measurement of the Nb/Ho/Gd (35/10/20 nm) sample. The unlabelled sharp peaks are from the sapphire substrate.

magnetisation dropping sharply as soon as a small positive magnetic field is applied.

Some part of the structure must be extremely sensitive not just to the direction of the applied field, but the direction of *change* of the applied field. The structure also relaxes somewhat at low fields, characterised by an increase in magnetisation. And when what would be the ferromagnetic switch takes place, the magnetisation does not change sign. Since Gu *et al.*[75] showed that for 12 nm of high-quality Ho the conical structure is irreversibly unwound by slightly less that 1 T of applied field, we would not expect the observed behaviour to be explained by such structures. Also, the unwinding of the conical structure usually happens outside the main hysteresis loop, and at fields of at up to 0.5 T. However, we do not know what effect the presence of the Gd layer has on the intrinsic magnetic structure of the Ho.

Magnetoresistance ($M(R)$) measurements were also performed on the sample. Fig. 7.10 shows two such measurements at slightly different temperatures. $R(H)$ measurements should be taken at the temperature at which the gradient of the resistance is highest, during the superconducting transition. In this way, the maximum difference in resistance can be captured.

The measurement at 6.8 K was taken more slowly than that at 6.9 K, confirming that the features within the "fangs" are real. Temperature stability during these measurements was between 20 and 30 mK. The mismatch at zero field between the two branches of the loop in the red curve is probably due to a constant drift in

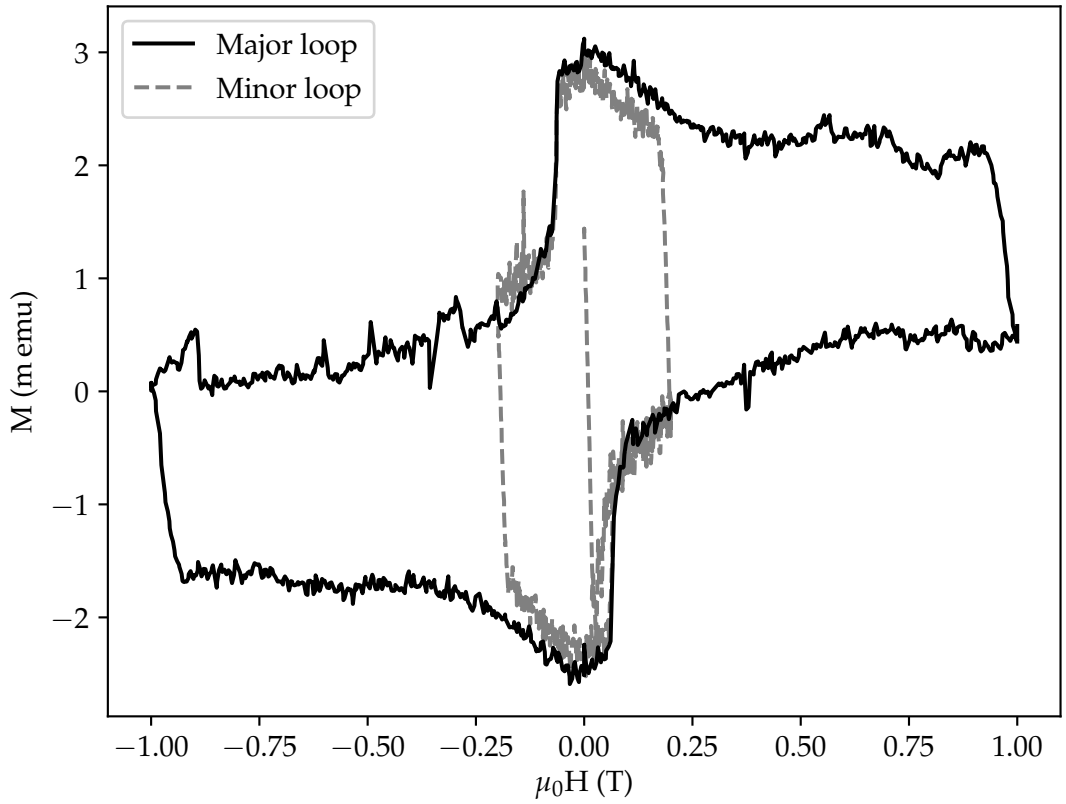

Figure 7.9: Low temperature (2.2 K) magnetic hysteresis measurements of the Nb/Ho/Gd (35/10/20 nm) structure. The grey dotted curve shows a measurement taken in the virgin state, hence the central line. The black data was gathered at 2.2 K, and the grey at 3.0 K.

temperature over time.

The major features of the $R(H)$ curves coincide with the conventional, albeit minor, change in magnetisation seen in the $M(H)$ loops, as shown in Fig. 7.11. However, the $R(H)$ curves extend beyond the graph to 1 T so the other magnetisation switch is not seen in the $R(H)$ curves.

The difference between the two branches of the $R(H)$ curves tells us that we should observe a difference in T_c between the two magnetic states, if after applying a field to reach that state, the state remains when the field is removed.

Fig. 7.12 shows the difference in T_c between the two magnetic states above and below $\sim$60 mT. The T_c is measured in zero field, but after specific field values have been applied. First, a large positive field is applied and removed so that the sample is what would conventionally be the parallel state. Then the T_c is measured. Then a small negative field is applied and removed so that the sample is in the antiparallel state, and the T_c is measured again. In this case, the small applied field was -70 mT to ensure that the antiparallel state is reached, however too high a field would decrease the ΔT_C. The increase in resistance on the outside of the "fangs" in the $M(R)$ curve shows this. The aim is to measure the T_c at the point of the $M(R)$ curve where the difference between the two branches is a maximum. The dashed lines show a repeat measurement to ensure that the switching between the two magnetic states is reliable.

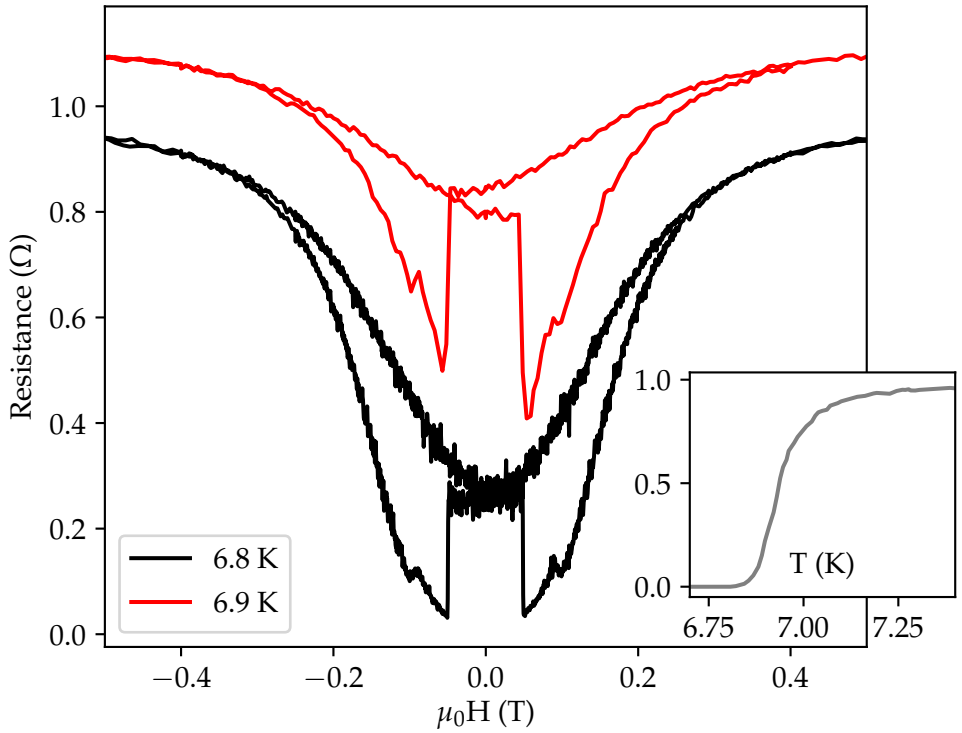

Figure 7.10: Magnetoresistance measurements of the Nb/Ho/Gd (35/10/20 nm) structure at different temperatures. The red curve has been vertically offset by 0.15 Ω for visual clarity. Inset: the superconducting transition of the sample in zero field.

The ΔT_c measured at 50% of the normal-state resistance is ∼40 mK. This is a better performance than that achieved by the Ni/Gd/Ni-based spin valve, but still not as impressive as that achieved by Gu *et al.*[76] There are many possible reasons for this including parameters which we know are important for a high ΔT_c, including having a long superconducting coherence length, low pair-breaking scattering, and a high interface transparency. However, Gu *et al.* also found that when modelled, their results showed that the exchange energy in the Ho was anomalously low, for reasons as yet not understood. The difference between our devices and Gu's is the adjacent Gd layer, which could be influencing the strength of the exchange field within the Ho. The difference should not be arising due to out-of-plane components of any remnants of the conical structure of the Ho since our Ho layer is the same thickness as Gu's, and they could detect no such remnant when measuring the out-of-plane response. Further study will be needed to examine precisely why the discrepancy between the devices remains.

Summary Throughout this chapter we have seen the evolution of the Ni/Gd-based spin valve design. Although exchange biasing a simple Ni/Gd bilayer is viable solution to generate inhomogeneity, the maximum inhomogeneity in a structure with appropriate layer thicknesses for spin valve design does not occur at temperatures which are low enough for superconductivity to be present. Utilising the intrinsic inhomogeneity present in the Ni/Gd/Ni trilayers proved a better solution. An interesting approach in the future would be to combine the two

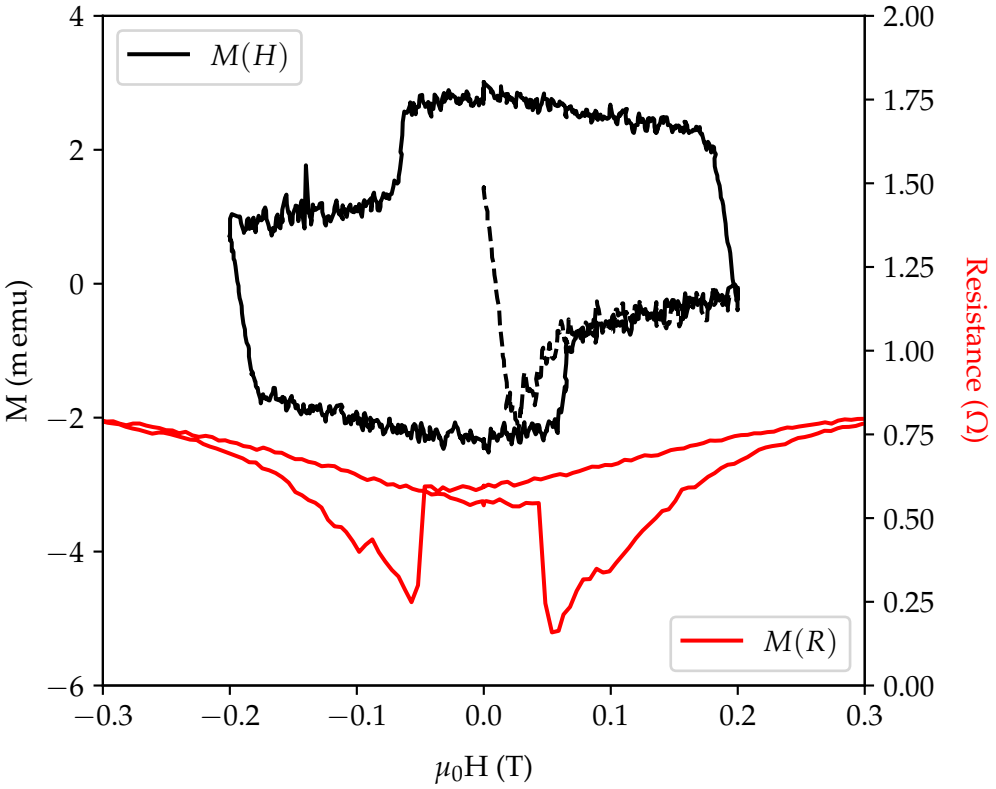

Figure 7.11: Magnetoresistance (red) and magnetic hysteresis loop (black) measurements of the Nb/Ho/Gd (35/10/20 nm) structure. The sharp changes in resistance coincide with the magnetic switching of one of the layers in the sample. The dashed line shows the magnetic response from the virgin state.

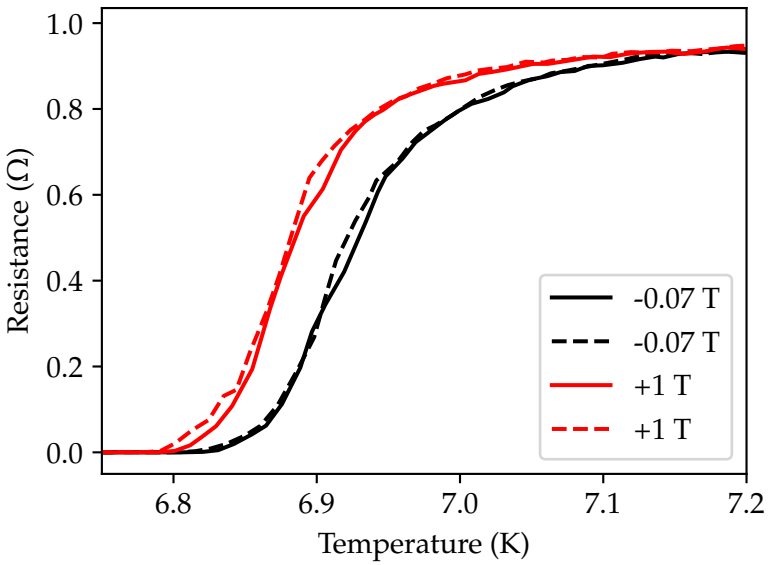

Figure 7.12: Difference in T_c between the parallel state (after applying 1 T), and the antiparallel state (after applying −0.07 T) in a Nb/Gd/Ho (35/10/20 nm) structure. The dashed lines show a repeated measurement.

designs and exchange bias the top Ni layer in the structure, in order to maximise the inhomogeneity present at remanence, since, as we see from the model results in the previous chapter, the maximum intrinsic inhomogeneity in the system otherwise is at finite field values.

The smaller mismatch between saturation magnetisations of Ho and Gd layers compared to that of Gd and Ni layers did not present the same difficulties when Ho-based designs were used. This design showed promise, and very interesting future work would be to investigate the micromagnetic structure of such a device. Unfortunately XMCD does not appear to be a viable technique for this due to the limitations on the energy of the x-rays produced by synchrotrons.

Part IV

Conclusion

Chapter 8

Summary and further work

8.1 XMCD

The XMCD results presented here represent a comprehensive study of the Ni/Gd system. It is the first study to examine such a broad range of layer thicknesses and throughout a large temperature range. We were fortunate to have access to such a powerful experimental technique when access to the necessary equipment is so highly sought after.* The observed behaviours fit into three categories; constant alignment of the layers as a function of temperature, a switch in alignment as the temperature increases, and a continuous region of magnetic inhomogeneity driven by the antiparallel coupling at the Ni/Gd interface.

The first two behaviours are consistent with major experimental and theoretical results in the field. However, the final behaviour was best explained by a newly developed simple model. Assuming strict antiparallel coupling at the interface, the Zeeman and exchange energies compete to determine the state of the system, and the decreasing average magnetisation as a function of temperature.

In the case of Prieto *et al.*[77] and Robinson *et al.*,[78] the model could help to reinterpret the experimental results. In both cases it was assumed that a domain wall was present *only* in the RE layer of a TM/RE/TM multilayer. In the case of Robinson's experiment spin-triplet Cooper pairs were being generated, and such generation relies on a region of continuous magnetic inhomogeneity, as a Bloch domain wall in the Gd would provide. However, according to our model the inhomogeneity would actually extend into both Ni layers and would not be confined to the Gd. The inhomogeneity would also be symmetric about the middle of the stack which is important in the Josephson junction devices used in the experiment, since the spin-triplet pairs which have been generated to penetrate far into the ferromagnetic layers then have to be converted back into spin-singlet pairs for transport in the superconductor at the other end of the junction. The results from our model would still explain the results observed in that experiment.

The output of the model proved extremely useful due to its flexibility. Either conventional hysteresis loops can be produced to directly compare to experimental results, or phase diagrams can be constructed, or the vector diagrams can be drawn which directly tell us the micromagnetic structure of the stack being studied. The advantage of working with models is that large quantities of data can be produced, analysed and plotted automatically.

* We were also fortunate enough to have our work chosen as an SSRL research highlight.

When the latest implementation of the model is finished it should be easier to use it to study systems other than a symmetrical TM/RE/TM system. For example, the bilayer system studied by Barth *et al.*[37] would be an interesting subject to model. If the model can corroborate their measured magnetic response of the system despite the implicit assumption in the model of a perfect Ni/Gd interface, the orange-peel coupling hypothesis may be rendered unnecessary. However, an *in situ* growth characterisation technique would also offer insights into the nature of the interfaces between the Ni and Gd layers. Such a study would be important in helping to justify or undermine the assumptions made in the model. Knowing the limitations of a simple model is vital in preventing its unjustified use.

In order to corroborate the results of the model, modelling the Ni/Gd/Ni system in a more detailed micromagnetic framework like OOMMF would be beneficial. Such work could also provide more insights into the specifics of Robinson's Josephson junction work, since the smaller cross-sectional area of the functional stacks in that work could lead to extra effects such as fringe fields.

8.2 Spin valves

Ni/Gd/Ni spin valves were fabricated with the same structures as those samples which showed interesting behaviour in the XMCD measurements. Although these spin valves did show a T_c difference between two controllable states, the difference was not as high as other spin valve designs.

Exchange biased bilayer spin valve designs were less successful, although worthy of further study, especially due to the ease with which Ni can be exchange biased by FeMn. Of particular interest is the hypothesis of the "anti-exchange bias" influence of the Ni on the Gd, it would be interesting to measure a device with a non-magnetic spacer layer between the two. Also of interest would be to combine the two Ni/Gd-based designs, i.e., to exchange bias one of the Ni layers in the Ni/Gd/Ni stack to more easily control the presence of the inhomogeneity, especially at low values of applied field.

Again, further work with the model could prove useful in this area. Adding the feature of the pinning of one surface layer to the model would be trivial, and in this way the model would simulate exchange bias. The model could then be used to study exchange biased bilayer spin valves, as well as being used to explore the design of other bilayer-based spin valves.

Not simply for the purposes of symmetry, although it would be satisfying, a further look at Robinson *et al.*'s work on the Ni/Gd/Ni Josephson junctions could be interesting. Since the majority of this work was inspired by trying to understand those results, having now achieved the objective of understanding the magnetic structure of those devices, the new knowledge could be used to refine the design of those devices.

Although a slight departure from the main RE/TM theme, the Gd/Ho devices showed great promise, and displayed some very interesting magnetic behaviour. Unfortunately, a comprehensive study of the coupling between the two layers would be a PhD project unto itself. Even decades after a peak in interest in the rare-earth ferromagnets they can still surprise us.

This is therefore a system ripe for further study. Having seen how powerful an element-specific measurement technique is in understanding the magnetic structure of multilayers, performing XMCD measurements on the system would be ideal.

However, recall that the energy needed to measure the Gd $M_{3,4}$ transition was at the edge of SSRL's capabilities, and the same transition in Ho is at a higher energy still.

Gu *et al.* concluded that the impressive results from the Ho-based spin valves were due to some new physics which greatly suppressed the exchange energy within the Ho. Is this still the case in our devices, or did the presence of the Gd remove or just mask this effect? What feature of the Ho gives rise to this effect, and is that feature shared by Gd? Bearing in mind that the same results obtained for Ho were also obtained for Dy-based devices.

As ever, perhaps more questions than were answered have sprung up as the result of this research.

Appendix A

Open access

All of the XMCD data presented in this work is available open access at:
`http://dx.doi.org/10.17863/CAM.609`.

Included with the data is a guide to the layout of the files and a guide to how to plot it. However, the sample names used in this work have used a different system from that recorded in the data archive. A conversion table is presented below:

Sample number									
S1	S2	S3	S4	S5	S6	S7	S8	S9	S10
S1old	S1new	S2old	S2new	S3old	S3new	S4old	S4new	1b	2b
S11	S12	S13	S14	S15	S16	S17	S18	S19	S20
PS1	PS2	PS3	PS4	US3	PCS1	PCS2	PCS3	EPS1	EPS2
Sample name used in archive									

Table A.1: Conversion between the sample numbers used throughout this paper, and the names of samples as labelled in the data archive.

Appendix B

Full XMCD data

B.0.1 Full results

Hysteresis loops from most samples are now presented, in order of which behaviour they display. Not all the data are presented since some is simply too noisy to be intelligible. Some hysteresis loops do not close or contain sudden jumps due to a combination of a low signal to noise ratio, and a sudden injection of electrons into the accelerator beam leading to a sudden increase in x-ray intensity, which the measurement stabilisation system could not cope with.

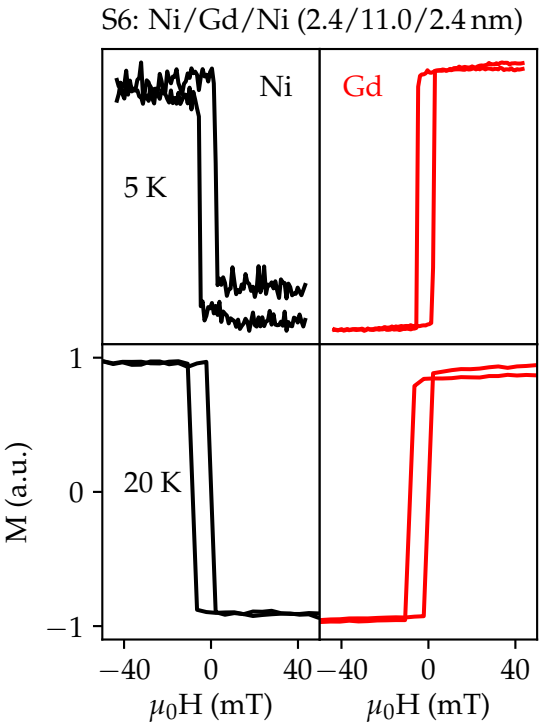

Figure B.1

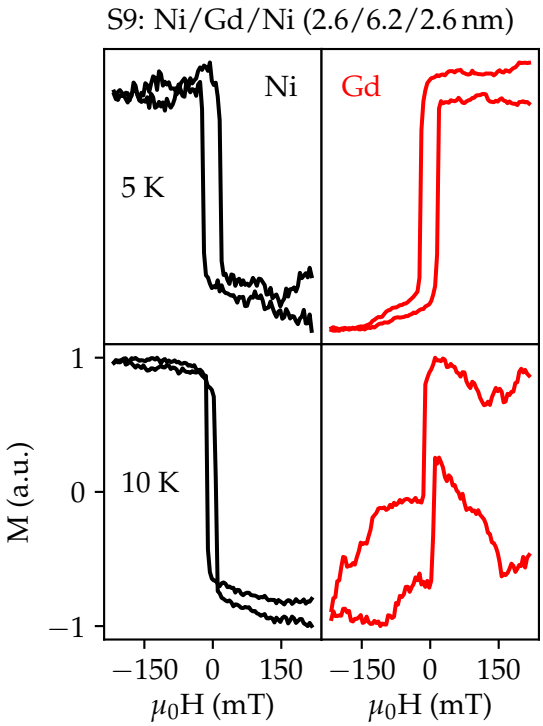

Figure B.2

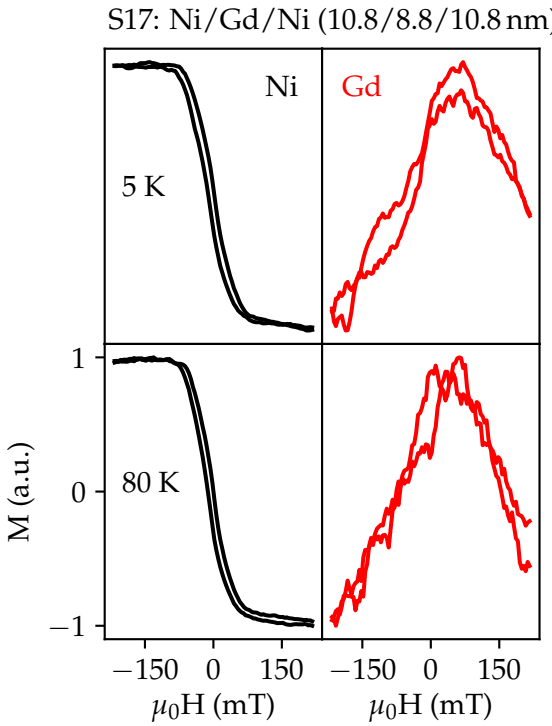

Figure B.3

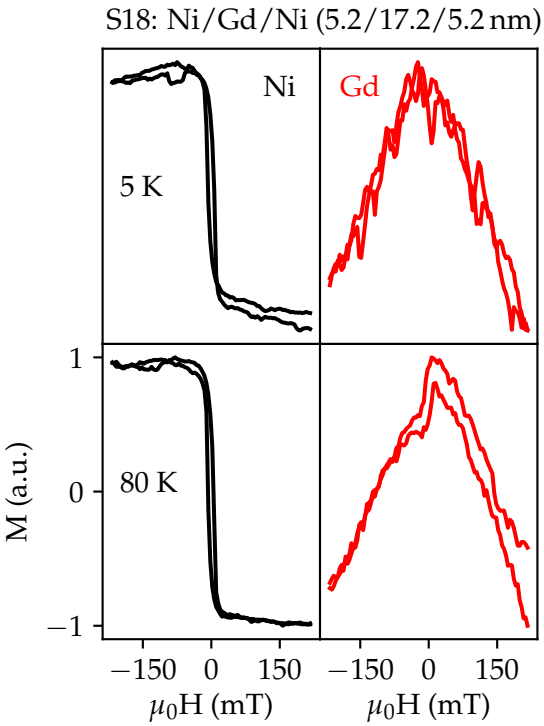

Figure B.4

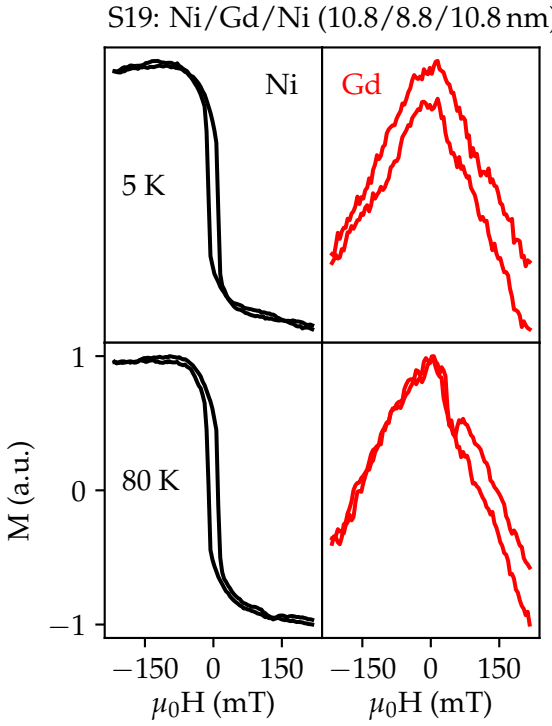

Figure B.5

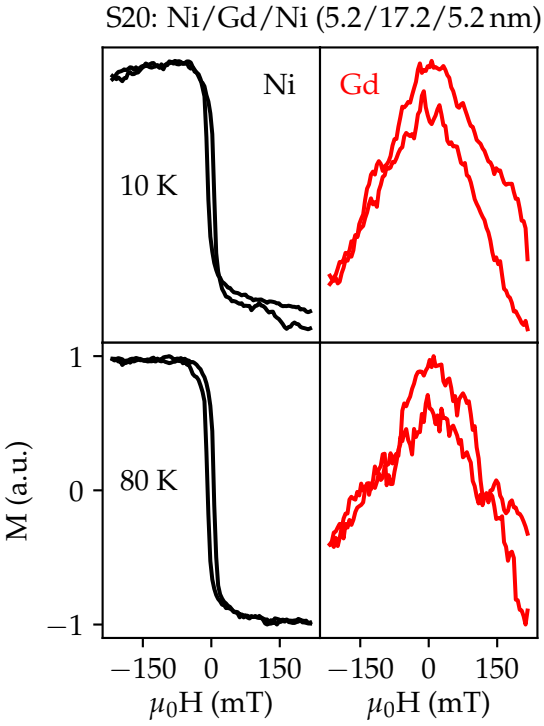

Figure B.6

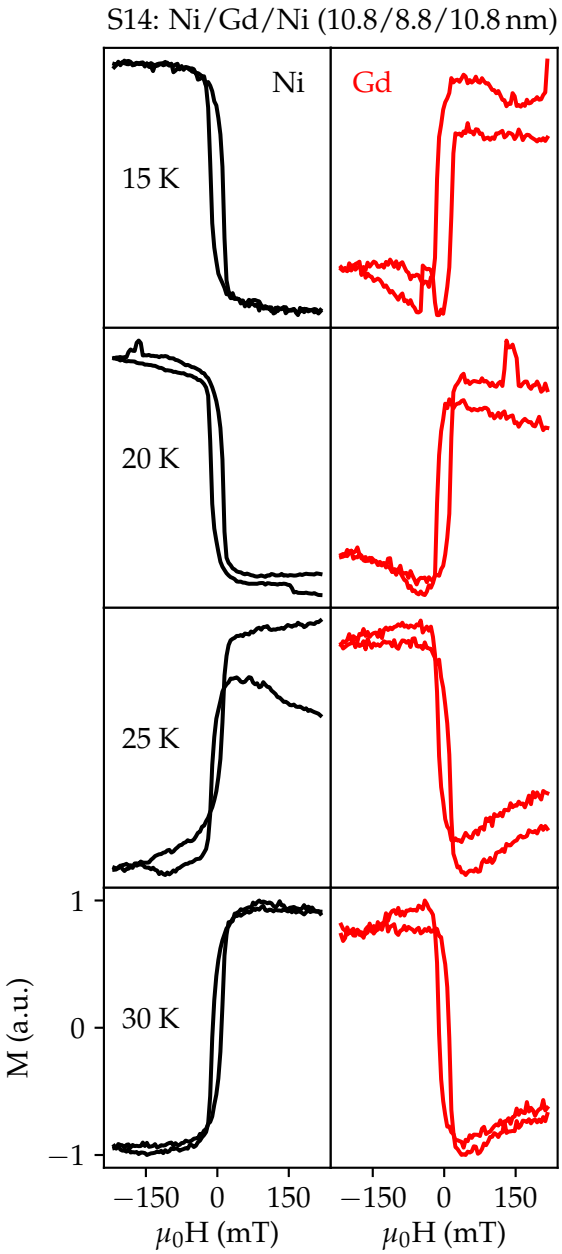

Figure B.7

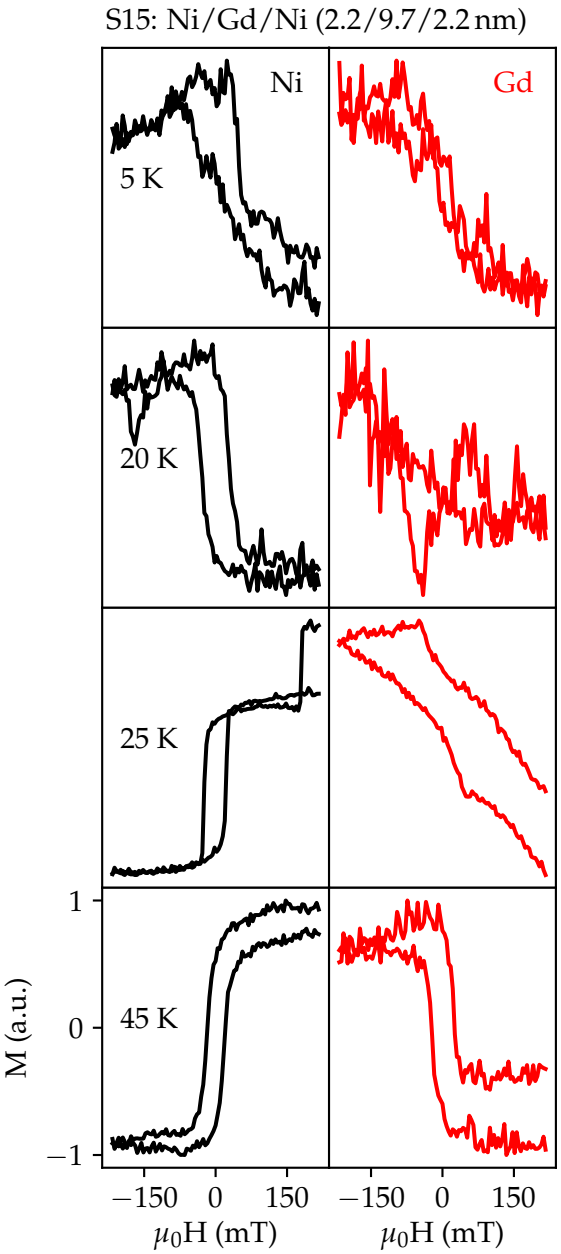

Figure B.8

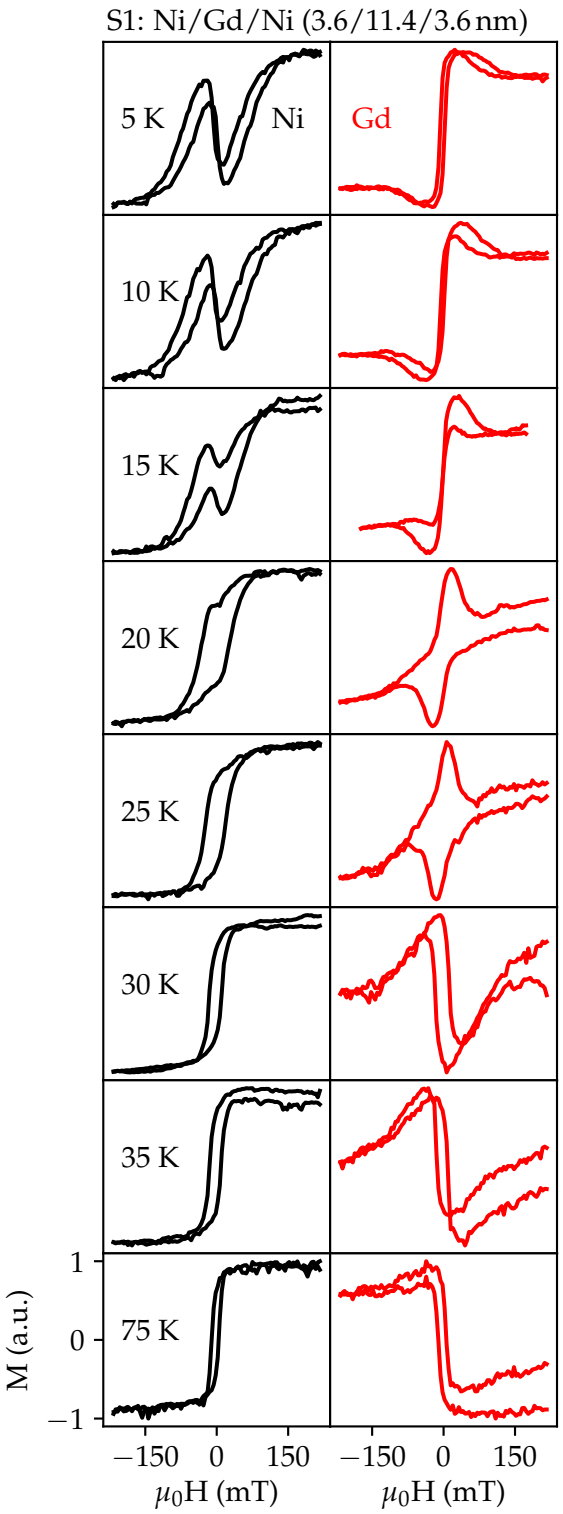

Figure B.9

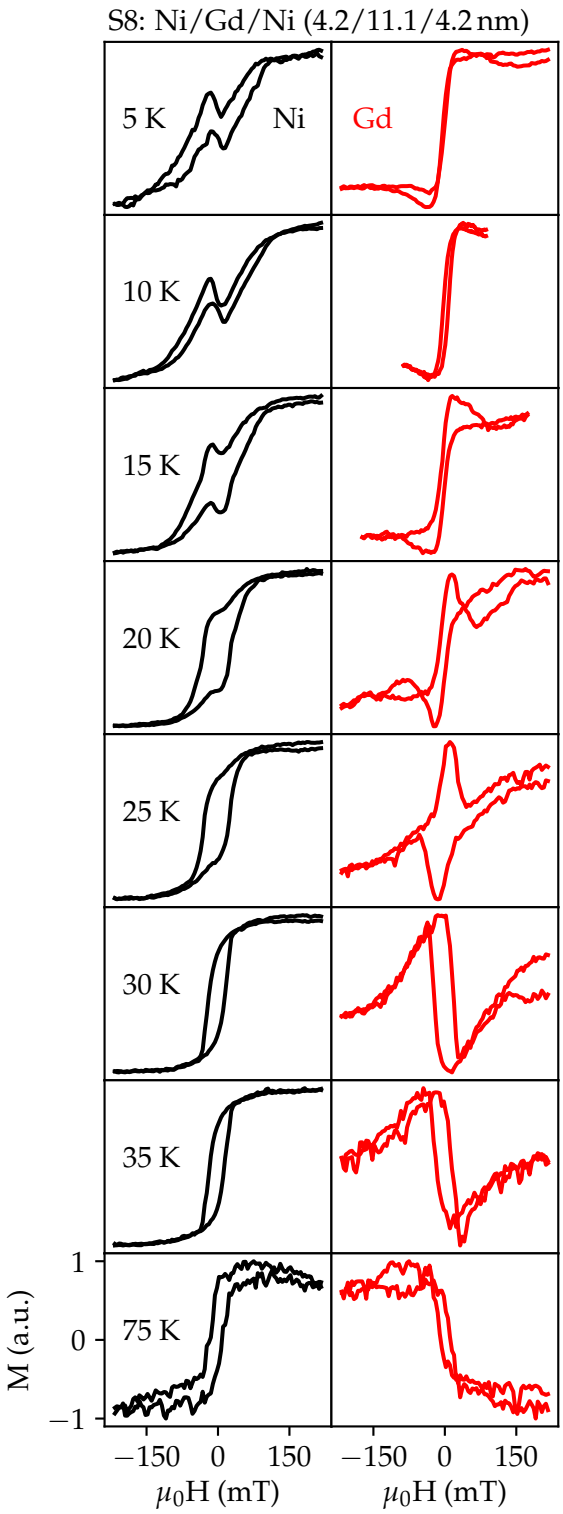

Figure B.10

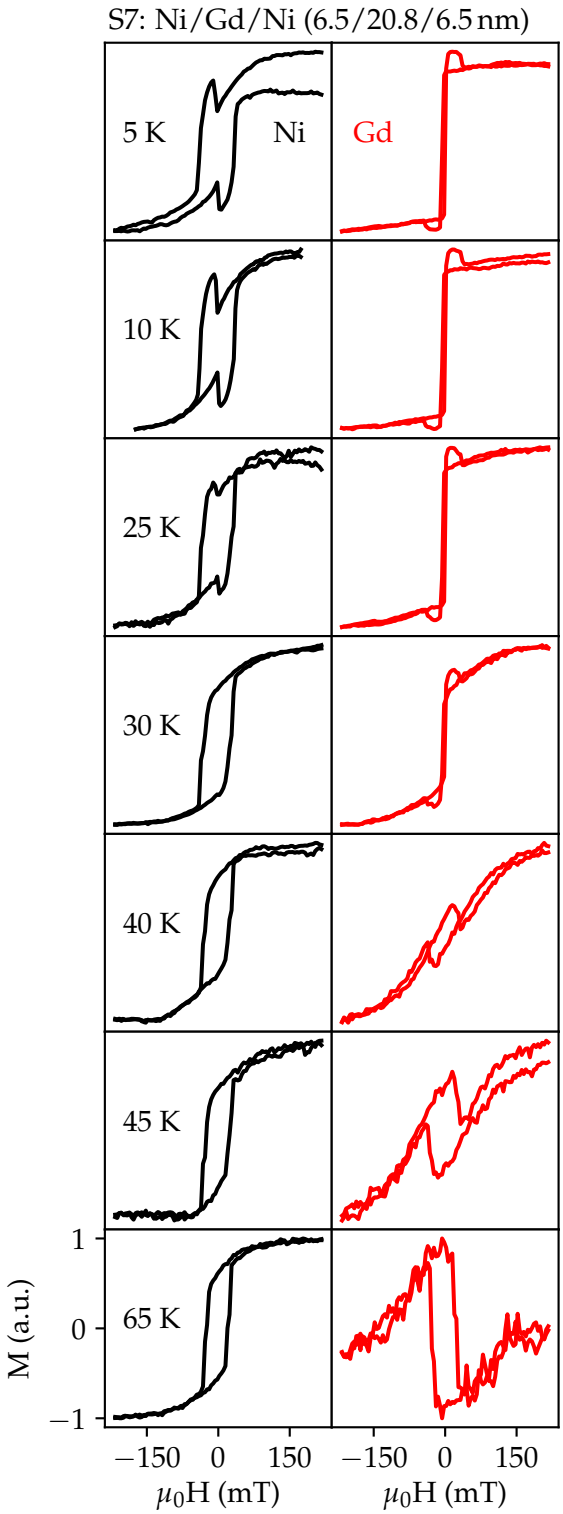
S7: Ni/Gd/Ni (6.5/20.8/6.5 nm)
5 K
Ni
Gd
10 K
25 K
30 K
40 K
45 K
65 K
M (a.u.)
1
0
−1
−150
0
150
−150
0
150
μ_0H (mT)
μ_0H (mT)

Figure B.11

Appendix C

Properties of Gd and Ni

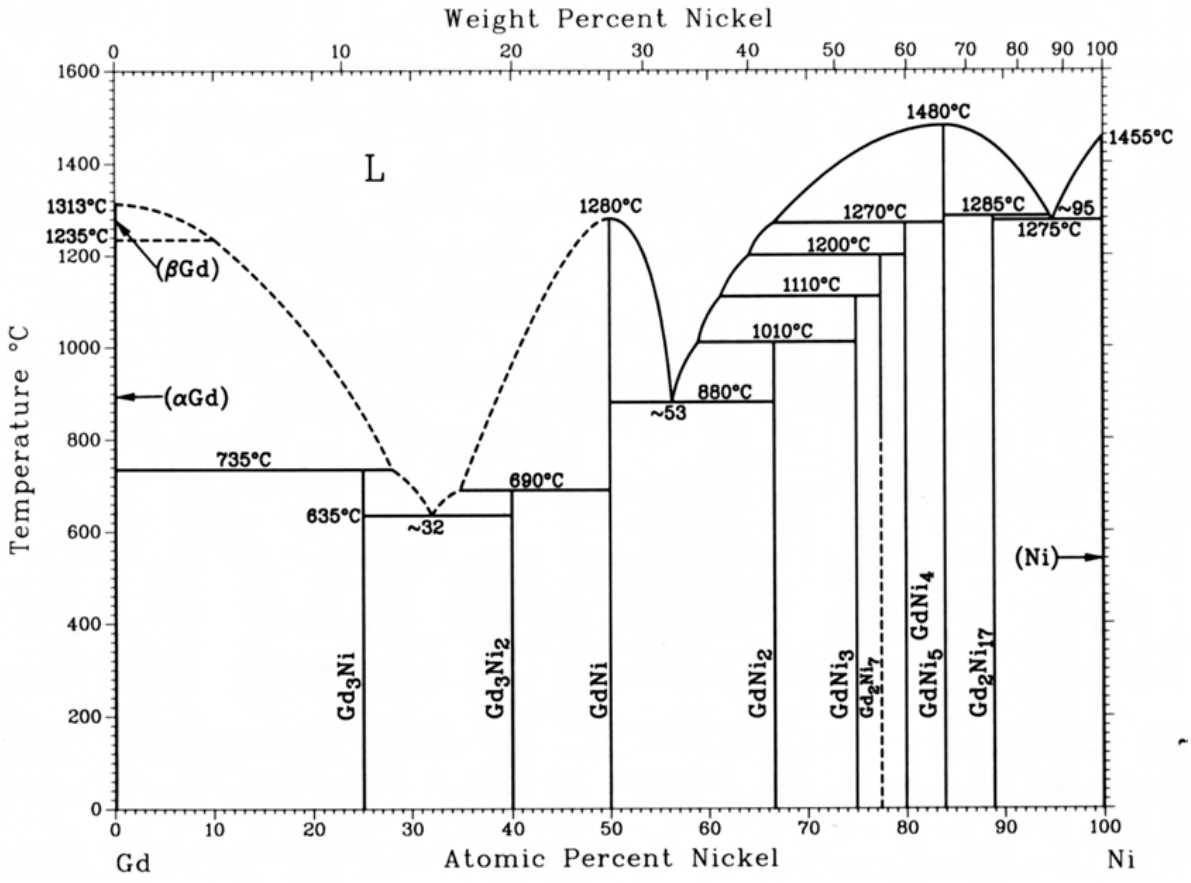

Figure C.1: Phase diagram of the Ni-Gd binary alloy system. From 149. All Ni/Gd films in this research were deposited at room temperature or below, and were not annealed.

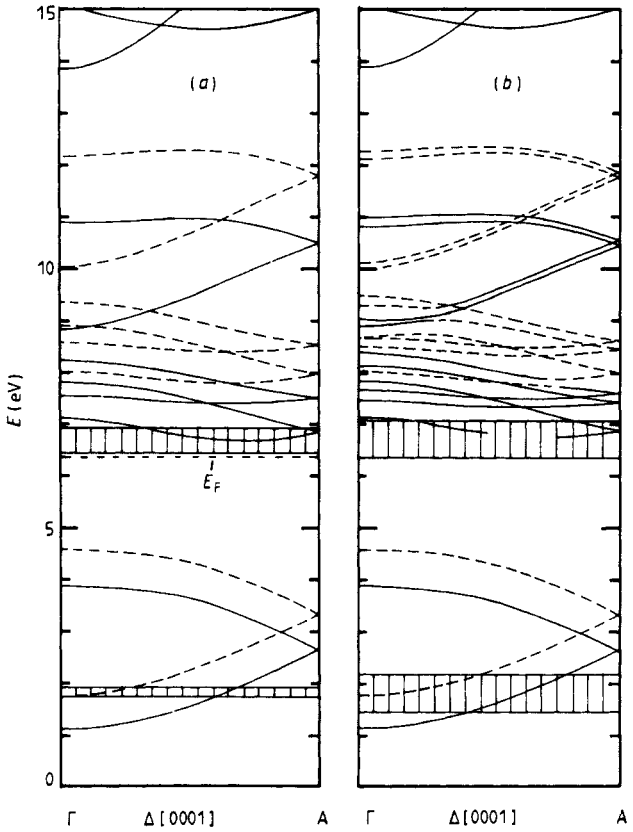

Figure C.2: Band structure of Gd. From Ref 147.

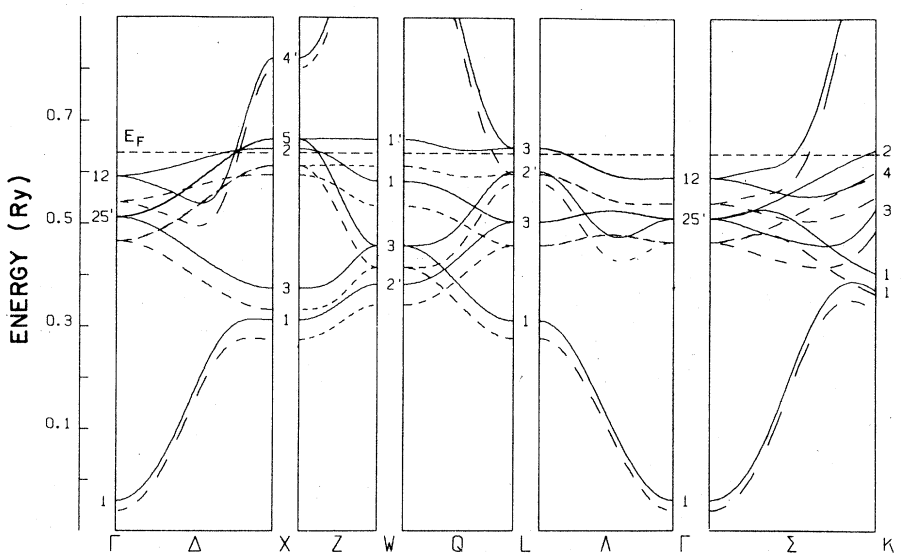

Figure C.3: Band structure of Ni. From Ref 148.

Bibliography

[1] N. Krishnamurthy and C. K. Gupta. *Extractive Metallurgy of Rare Earths*. CRC Press, 2004.

[2] J. Stöhr and H. C. Siegmann. *Magnetism: From Fundamentals to Nanoscale Dynamics*. Springer Series in Solid-State Sciences. Springer, 2006.

[3] S. Blundell. *Magnetism in condensed matter*. Oxford University Press, 2003.

[4] B. P. Cowan. *Topics in Statistical Mechanics*. Imperial College Press advanced physics texts. Imperial College Press, 2005.

[5] R. M. Eisberg and Resnick. *Quantum Physics: of Atoms, Molecules, Solids, Nuclei and Particles*. Wiley India Pvt. Limited, 2006.

[6] E. M. Purcell. *Electricity and Magnetism*. Electricity and Magnetism. Cambridge University Press, 2013.

[7] N. Banerjee. *Nonlinear Giant Magnetoresistance in Dual Spin Valves*. PhD thesis, University of Cambridge, September 2011.

[8] R. Elliott. *Magnetic Properties of Rare Earth Metals*. Springer US, 2013.

[9] M. A. Ruderman and C. Kittel. Indirect exchange coupling of nuclear magnetic moments by conduction electrons. *Phys. Rev.*, 96:99–102, Oct 1954.

[10] T. Kasuya. A theory of metallic ferro- and antiferromagnetism on zener's model. *Progress of Theoretical Physics*, 16(1):45–57, 1956.

[11] K. Yosida. Magnetic properties of cu-mn alloys. *Phys. Rev.*, 106:893–898, Jun 1957.

[12] C. Kittel. Indirect exchange interactions in metals. volume 22 of *Solid State Physics*, pages 1 – 26. Academic Press, 1969.

[13] J. Jensen and A. R. Mackintosh. *Rare earth magnetism*. Clarendon Oxford, 1991.

[14] CF Majkrzak, J Kwo, M Hong, Y Yafet, Doon Gibbs, CL Chien, and Jakob Bohr. Magnetic rare earth superlattices. *Advances in Physics*, 40(2):99–189, 1991.

[15] D. A. Jehan, D. F. McMorrow, R. A. Cowley, and G. J. McIntyre. The magnetic structure of holmium in an applied magnetic field. *J. Magn. Magn. Mater.*, 104-107:1523–1524, 1992.

[16] C. H. Snyder. *Microwave magnetic resonance and absorption in holmium single crystals*. PhD thesis, Rice University, Houston, May 1969.

[17] J. Jensen. Theory of commensurable magnetic structures in holmium. *Phys. Rev. B*, 54:4021–4032, Aug 1996.

[18] W. C. Koehler, J. W. Cable, M. K. Wilkinson, and E. O. Wollan. Magnetic structures of holmium. I. The virgin state. *Phys. Rev.*, 151:414–424, Nov 1966.

[19] W. C. Koehler, J. W. Cable, H. R. Child, M. K. Wilkinson, and E. O. Wollan. Magnetic structures of holmium. II. The magnetization process. *Phys. Rev.*, 158:450–461, Jun 1967.

[20] S. Bates, C. Patterson, G. J. McIntyre, S. B. Palmer, A. Mayer, R. A. Cowley, and R. Melville. The magnetic structure of holmium. II. *Journal of Physics C: Solid State Physics*, 21(22):4125, 1988.

[21] R. A. Cowley and S. Bates. The magnetic structure of holmium. I. *Journal of Physics C: Solid State Physics*, 21(22):4113, 1988.

[22] N. A. Spaldin. *Magnetic materials: fundamentals and applications*. Cambridge University Press, 2010.

[23] J. Nogués and I. K. Schuller. Exchange bias. *Journal of Magnetism and Magnetic Materials*, 192(2):203–232, Feb 1999.

[24] P. Grünberg, R. Schreiber, Y. Pang, M. B. Brodsky, and H. Sowers. Layered magnetic structures: Evidence for antiferromagnetic coupling of fe layers across cr interlayers. *Phys. Rev. Lett.*, 57:2442–2445, Nov 1986.

[25] S. S. P. Parkin, N. More, and K. P. Roche. Oscillations in exchange coupling and magnetoresistance in metallic superlattice structures: Co/ru, co/cr, and fe/cr. *Phys. Rev. Lett.*, 64:2304–2307, May 1990.

[26] D. Weller, S. F. Alvarado, W. Gudat, K. Schröder, and M. Campagna. Observation of surface-enhanced magnetic order and magnetic surface reconstruction on Gd(0001). *Phys. Rev. Lett.*, 54:1555–1558, Apr 1985.

[27] M. Taborelli, R. Allenspach, G. Boffa, and M. Landolt. Magnetic coupling of surface adlayers: Gd on Fe(100). *Phys. Rev. Lett.*, 56:2869–2872, Jun 1986.

[28] R. E. Camley. Surface spin reorientation in thin Gd films on Fe in an applied magnetic field. *Phys. Rev. B*, 35:3608–3611, Mar 1987.

[29] R. E. Camley. Properties of magnetic superlattices with antiferromagnetic interfacial coupling: Magnetization, susceptibility, and compensation points. *Phys. Rev. B*, 39:12316–12319, Jun 1989.

[30] L. T. Baczewski, R. Kalinowski, and A. Wawro. Magnetization and anisotropy in Fe/Gd multilayers. *J. Magn. Magn. Mater.*, 177–181, Part 2(0):1305 – 1307, 1998. International Conference on Magnetism (Part II).

[31] D. Haskel, G. Srajer, J. C. Lang, J. Pollmann, C. S. Nelson, J. S. Jiang, and S. D. Bader. Enhanced interfacial magnetic coupling of Gd/Fe multilayers. *Phys. Rev. Lett.*, 87:207201, Oct 2001.

[32] A. Koizumi, M. Takagaki, M. Suzuki, N. Kawamura, and N. Sakai. Anomalous magnetic hysteresis of Gd and Fe moments in a Gd/Fe multilayer measured by hard x-ray magnetic circular dichroism. *Phys. Rev. B*, 61:R14909–R14912, Jun 2000.

[33] A. Pogorily, E. Shypil, and C. Alexander. A study of magnetization in exchange-coupled FM/Gd bilayers. *Journal of Magnetism and Magnetic Materials*, 286(Supplement C):493 – 496, 2005. Proceedings of the 5th International Symposium on Metallic Multilayers.

[34] B. B. Van Aken, J. L. Prieto, and N. D. Mathur. Ground state and constrained domain walls in Gd/Fe multilayers. *Journal of Applied Physics*, 97(6):063904, 2005.

[35] D. Haskel, G. Srajer, Y. Choi, D. R. Lee, J. C. Lang, J. Meersschaut, J. S. Jiang, and S. D. Bader. Nature of inhomogeneous magnetic state in artificial fe/gd ferrimagnetic multilayers. *Phys. Rev. B*, 67:180406, May 2003.

[36] J. L. Prieto, B. B. van Aken, G. Burnell, C. Bell, J. E. Evetts, N. Mathur, and M. G. Blamire. Transport properties of sharp antiferromagnetic boundaries in gd/fe multilayers. *Phys. Rev. B*, 69:054436, Feb 2004.

[37] A. Barth, F. Treubel, M. Marszałek, W. Evenson, O. Hellwig, C. Broschel, M. Albrecht, and G. Schatz. Magnetic coupling in Gd/Ni bilayers. *J. Phys.: Condens. Matter*, 20:395232, 2008.

[38] A. Barth. *Magnetic and structural properties of the Gd/Ni-bilayer-system*. PhD thesis, Universistät Konstanz, July 2007.

[39] M. Cyrot. Ginzburg-landau theory for superconductors. *Reports on Progress in Physics*, 36(2):103, 1973.

[40] J. Bardeen, L. N. Cooper, and J. R. Schrieffer. Theory of superconductivity. *Phys. Rev.*, 108:1175–1204, Dec 1957.

[41] L. N. Cooper. Bound electron pairs in a degenerate Fermi gas. *Phys. Rev.*, 104:1189–1190, Nov 1956.

[42] J. F. Annett. *Superconductivity, Superfluids and Condensates*. Oxford Master Series in Physics. OUP Oxford, 2004.

[43] J. C. Cuevas, J. Hammer, J. Kopu, J. K. Viljas, and M. Eschrig. Proximity effect and multiple Andreev reflections in diffusive superconductor–normal-metal–superconductor junctions. *Physical Review B*, 73(18):184505, 2006.

[44] P. G. De Gennes. Coupling between ferromagnets through a superconducting layer. *Physics Letters*, 23(1):10–11, 1966.

[45] P. G. De Gennes. Boundary effects in superconductors. *Reviews of Modern Physics*, 36(1):225, 1964.

[46] P. G. De Gennes and E. Guyon. Superconductivity in "normal" metals. *Physics Letters*, 3(4):168–169, 1963.

[47] I. F. Lyuksyutov and V. L. Pokrovsky. Ferromagnet–superconductor hybrids. *Advances in Physics*, 54(1):67–136, 2005.

[48] P. Fulde and R. A. Ferrell. Superconductivity in a strong spin-exchange field. *Phys. Rev.*, 135:A550–A563, Aug 1964.

[49] A. I. Larkin and Yu. N. Ovchinnikov. Inhomogeneous state of superconductors. *Sov. Phys. JETP.*, 20:762, 1965.

[50] A. I. Buzdin. Proximity effects in superconductor-ferromagnet heterostructures. *Rev. Mod. Phys.*, 77:935–976, Sep 2005.

[51] F. S. Bergeret, A. F. Volkov, and K. B. Efetov. Manifestation of triplet superconductivity in superconductor-ferromagnet structures. *Phys. Rev. B*, 68:064513, Aug 2003.

[52] F. S. Bergeret, A. F. Volkov, and K. B. Efetov. Odd triplet superconductivity and related phenomena in superconductor-ferromagnet structures. *Rev. Mod. Phys.*, 77:1321–1373, Nov 2005.

[53] F. S. Bergeret, A. F. Volkov, and K. B. Efetov. Long-range proximity effects in superconductor-ferromagnet structures. *Phys. Rev. Lett.*, 86:4096–4099, Apr 2001.

[54] A. Kadigrobov, R. I. Shekhter, and M. Jonson. Quantum spin fluctuations as a source of long-range proximity effects in diffusive ferromagnet-super conductor structures. *EPL (Europhysics Letters)*, 54(3):394, 2001.

[55] M. Eschrig. Spin-polarized supercurrents for spintronics. *Physics Today*, 64(1):43–49, 2011.

[56] M. Houzet and A. I. Buzdin. Long range triplet Josephson effect through a ferromagnetic trilayer. *Phys. Rev. B*, 76:060504, Aug 2007.

[57] M. Sigrist and T. M. Rice. Paramagnetic effect in high Tc superconductors - a hint for d-wave superconductivity. *Journal of the Physical Society of Japan*, 61(12):4283–4286, 1992.

[58] A. I. Buzdin, M. Yu Kupriyanov, and B. Vujičić. The oscillation of the critical temperature of S/F multylayers. *Physica C: Superconductivity*, 185:2025–2026, 1991.

[59] Z. Radović, M. Ledvij, L. Dobrosavljević-Grujić, A. I. Buzdin, and J. R. Clem. Transition temperatures of superconductor-ferromagnet superlattices. *Physical Review B*, 44(2):759, 1991.

[60] J. J. Hauser, H. C. Theuerer, and N. R. Werthamer. Proximity effects between superconducting and magnetic films. *Physical Review*, 142(1):118, 1966.

[61] L. H. Greene, W. L. Feldmann, J. M. Rowell, B. Batlogg, E. M. Gyorgy, W. P. Lowe, and D. B. McWhan. Structural, magnetic and superconducting properties of rare earth/superconductor multilayer films. *Superlattices and Microstructures*, 1(5):407–415, 1985.

[62] B. Y. Jin and J. B. Ketterson. Artificial metallic superlattices. *Advances in Physics*, 38(3):189–366, 1989.

[63] J. S. Jiang, D. Davidović, D. H. Reich, and C. L. Chien. Oscillatory superconducting transition temperature in Nb/Gd multilayers. *Phys. Rev. Lett.*, 74:314–317, Jan 1995.

[64] I. C. Moraru, W. P. Pratt, and N. O. Birge. Observation of standard spin-switch effects in ferromagnet/superconductor/ferromagnet trilayers with a strong ferromagnet. *Phys. Rev. B*, 74:220507, Dec 2006.

[65] A. Potenza and C. H. Marrows. Superconductor-ferromagnet CuNi/Nb/-CuNi trilayers as superconducting spin-valve core structures. *Phys. Rev. B*, 71:180503, May 2005.

[66] A. Singh, C. Sürgers, and H. v. Löhneysen. Superconducting spin switch with perpendicular magnetic anisotropy. *Phys. Rev. B*, 75:024513, Jan 2007.

[67] A. Yu. Rusanov, S. Habraken, and J. Aarts. Inverse spin switch effects in ferromagnet-superconductor-ferromagnet trilayers with strong ferromagnets. *Phys. Rev. B*, 73:060505, Feb 2006.

[68] Ya. V. Fominov, A. A. Golubov, T. Yu. Karminskaya, M. Yu. Kupriyanov, R. G. Deminov, and L. R. Tagirov. Superconducting triplet spin valve. *JETP Letters*, 91(6):308–313, Mar 2010.

[69] G. Nowak, H. Zabel, K. Westerholt, I. Garifullin, M. Marcellini, A. Liebig, and B. Hjörvarsson. Superconducting spin valves based on epitaxial Fe/V superlattices. *Phys. Rev. B*, 78:134520, Oct 2008.

[70] A. A. Jara, C. Safranski, I. N. Krivorotov, C-T. Wu, A. N. Malmi-Kakkada, O. T. Valls, and K. Halterman. Angular dependence of superconductivity in superconductor/spin-valve heterostructures. *Physical Review B*, 89(18):184502, 2014.

[71] R. S. Keizer, S. T. B. Goennenwein, T. M. Klapwijk, G. X. Miao, G. Xiao, and A. Gupta. A spin triplet supercurrent through the half-metallic ferromagnet CrO_2. *Nature*, 439(7078):825–827, Feb 2006.

[72] C. Klose, Trupti S. Khaire, Y. Wang, W. P. Pratt, N. O. Birge, B. J. McMorran, T. P. Ginley, J. A. Borchers, B. J. Kirby, B. B. Maranville, and J. Unguris. Optimization of spin-triplet supercurrent in ferromagnetic Josephson junctions. *Phys. Rev. Lett.*, 108:127002, Mar 2012.

[73] I. Sosnin, H. Cho, V. T. Petrashov, and A. F. Volkov. Superconducting phase coherent electron transport in proximity conical ferromagnets. *Phys. Rev. Lett.*, 96:157002, Apr 2006.

[74] J. W. A. Robinson, J. D. S. Witt, and M. G. Blamire. Controlled injection of spin-triplet supercurrents into a strong ferromagnet. *Science*, 329(5987):59–61, 2010.

[75] Y. Gu, J. W. A. Robinson, M. Bianchetti, N. A. Stelmashenko, D. Astill, F. M. Grosche, J. L. MacManus-Driscoll, and M. G. Blamire. Magnetic state controllable critical temperature in epitaxial Ho/Nb bilayers. *APL Materials*, 2(4):046103, 2014.

[76] Y. Gu, G. B. Halász, J. W. A. Robinson, and M. G. Blamire. Large superconducting spin valve effect and ultrasmall exchange splitting in epitaxial rare-earth-niobium trilayers. *Phys. Rev. Lett.*, 115:067201, Aug 2015.

[77] J. L. Prieto, M. G. Blamire, and J. E. Evetts. Magnetoresistance in a constricted domain wall. *Phys. Rev. Lett.*, 90:027201, Jan 2003.

[78] J. W. A. Robinson, F. Chiodi, M. Egilmez, G. B. Halász, and M. G. Blamire. Supercurrent enhancement in Bloch domain walls. *Sci. Rep.*, 2:699, Mar 2012.

[79] R. E. Somekh and Z. H. Barber. Uhv sputter deposition with a research-scale dc magnetron. *Journal of Physics E: Scientific Instruments*, 21(11):1029, 1988.

[80] D. A. Glocker and S. I. Shah. *Handbook of thin film process technology*. IOP, 1997.

[81] Stephen A Campbell. *The science and engineering of microelectronic fabrication*. Oxford University Press, USA, 1996.

[82] S. Swann. Magnetron sputtering. *Physics in Technology*, 19(2):67, 1988.

[83] F. Treubel. *Ferrimagnetismus im Zweischichtsystem Gd/Ni*. PhD thesis, Universität Konstanz, 2005.

[84] B. D. Cullity and J. W. Weymouth. Elements of x-ray diffraction. *American Journal of Physics*, 25(6):394–395, 1957.

[85] W. L. Bragg. The diffraction of short electromagnetic waves by a crystal. *Proc. Camb. Philos. Soc.*, 17:43–57, 1913.

[86] M. Sardela. *Practical Materials Characterization*. Springer New York, 2014.

[87] N. Ashcroft and N. Mermin. *Solid State Physics*. Brooks Cole, 1976.

[88] J. Stöhr and Y. Wu. X-ray magnetic circular dichroism: Basic concepts and theory for 3d transition metal atoms. In *New Directions in Research with Third-Generation Soft X-Ray Synchrotron Radiation Sources*. Springer Netherlands, 1994.

[89] T. Funk, A. Deb, S. J. George, H. Wang, and S. P. Cramer. X-ray magnetic circular dichroism—a high energy probe of magnetic properties. *Coordination Chemistry Reviews*, 249(1):3–30, 2005.

[90] R. Carr and S. Lidia. The adjustable phase planar helical undulator. *SLAC-PUB*, (6337), 1993.

[91] S. Bonetti, R. Kukreja, Z. Chen, D. Spoddig, K. Ollefs, C. Schöppner, R. Meckenstock, A. Ney, J. Pinto, R. Houanche, J. Frisch, J. Stöhr, H. A. Dürr, and H. Ohldag. Microwave soft x-ray microscopy for nanoscale magnetization dynamics in the 5-10 GHz frequency range. *Review of Scientific Instruments*, 86(9), 2015.

[92] S. Kasap and P. Capper. *Springer handbook of electronic and photonic materials*. Springer, 2017.

[93] A. Korkin and D. J Lockwood. *Nanoscale Applications for Information and Energy Systems*. Springer Science & Business Media, 2012.

[94] S. Foner. Versatile and sensitive vibrating-sample magnetometer. *Review of Scientific Instruments*, 30(7):548–557, 1959.

[95] R. E. Camley and D. R. Tilley. Phase transitions in magnetic superlattices. *Phys. Rev. B*, 37:3413–3421, Mar 1988.

[96] O. F. K. McGrath, N. Ryzhanova, C. Lacroix, D. Givord, C. Fermon, C. Miramond, G. Saux, S. Young, and A. Vedyayev. Observation and interpretation of a partial Gd twisted spin state in an epitaxial Gd/Fe bilayer. *Phys. Rev. B*, 54:6088–6091, Sep 1996.

[97] K. Takanashi, Y. Kamiguchi, H. Fujimori, and M. Motokawa. Magnetization and magnetoresistance of Fe/Gd ferrimagnetic multilayer films. *J. Phys. Soc. Jpn.*, 61(10):3721–3731, 1992.

[98] T. D. C. Higgs, S. Bonetti, H. Ohldag, N. Banerjee, X. L. Wang, A. J. Rosenberg, Z. Cai, J. H. Zhao, K. A. Moler, and J. W. A. Robinson. Magnetic coupling at rare earth ferromagnet/transition metal ferromagnet interfaces: A comprehensive study of Gd/Ni. *Scientific Reports*, 6(30092), 2016.

[99] R. Skomski. *Simple models of magnetism*. Oxford University Press on Demand, 2008.

[100] D. Mauri, H. C. Siegmann, P. S. Bagus, and E. Kay. Simple model for thin ferromagnetic films exchange coupled to an antiferromagnetic substrate. *Journal of Applied Physics*, 62(7):3047–3049, 1987.

[101] S. Chikazumi and C. D. Graham. *Physics of Ferromagnetism*. International Series of Monographs on Physics. Clarendon Press, 1997.

[102] U. Hartmann. Origin of Brown's coercive paradox in perfect ferromagnetic crystals. *Phys. Rev. B*, 36:2331–2332, Aug 1987.

[103] W. F. Brown. Virtues and weaknesses of the domain concept. *Rev. Mod. Phys.*, 17:15–19, Jan 1945.

[104] B. Balasubramanian, P. Mukherjee, R. Skomski, P. Manchanda, B. Das, and D. J. Sellmyer. Magnetic nanostructuring and overcoming Brown's paradox to realize extraordinary high-temperature energy products. *Sci. Rep.*, 4, 2014.

[105] A. Aharoni. Theoretical search for domain nucleation. *Rev. Mod. Phys.*, 34:227–238, Apr 1962.

[106] J. Inoue, H. Itoh, S. Mitani, and K. Takanashi. Numerical study of magnetoresistance for currents perpendicular to planes in spring ferromagnets. *Phys. Rev. B*, 68:094418, Sep 2003.

[107] J. Inoue. A theory of biquadratic exchange coupling in magnetic multilayers. *Journal of Magnetism and Magnetic Materials*, 136(3):233 – 237, 1994.

[108] B. Dieny. Giant magnetoresistance in spin-valve multilayers. *Journal of Magnetism and Magnetic Materials*, 136(3):335 – 359, 1994.

[109] B. D. Schrag, A. Anguelouch, S. Ingvarsson, Gang Xiao, Yu Lu, P. L. Trouilloud, A. Gupta, R. A. Wanner, W. J. Gallagher, P. M. Rice, and S. S. P. Parkin. Néel "orange-peel" coupling in magnetic tunneling junction devices. *Applied Physics Letters*, 77(15):2373–2375, 2000.

[110] Ya V. Fominov, N. M. Chtchelkatchev, and A. A. Golubov. Critical temperature of superconductor/ferromagnet bilayers. *Journal of Experimental and Theoretical Physics Letters*, 74(2):96–99, 2001.

[111] S. Oh, D. Youm, and M. R. Beasley. A superconductive magnetoresistive memory element using controlled exchange interaction. *Applied physics letters*, 71(16):2376–2378, 1997.

[112] B. L. Rhodes, S. Legvold, and F. H. Spedding. Magnetic properties of holmium and thulium metals. *Phys. Rev.*, 109:1547–1550, Mar 1958.

[113] D. L. Strandburg, S. Legvold, and F. H. Spedding. Electrical and magnetic properties of holmium single crystals. *Phys. Rev.*, 127:2046–2051, Sep 1962.

[114] A. Di Bernardo, S. Diesch, Y. Gu, J. Linder, G. Divitini, C. Ducati, E. Scheer, M. G. Blamire, and J. W. A. Robinson. Signature of magnetic-dependent gapless odd frequency states at superconductor/ferromagnet interfaces. *Nature communications*, 6, 2015.

[115] I. T. M. Usman, K. A. Yates, J. D. Moore, K. Morrison, V. K. Pecharsky, K. A. Gschneidner, T. Verhagen, J. Aarts, V. I. Zverev, J. W. A. Robinson, J. D. S. Witt, M. G. Blamire, and L. F. Cohen. Evidence for spin mixing in holmium thin film and crystal samples. *Phys. Rev. B*, 83:144518, Apr 2011.

[116] M. Alidoust and J. Linder. Spin-triplet supercurrent through inhomogeneous ferromagnetic trilayers. *Phys. Rev. B*, 82:224504, Dec 2010.

[117] G. B. Halász, M. G. Blamire, and J. W. A. Robinson. Magnetic-coupling-dependent spin-triplet supercurrents in helimagnet/ferromagnet Josephson junctions. *Phys. Rev. B*, 84:024517, Jul 2011.

[118] C-T. Wu, O. T. Valls, and K. Halterman. Proximity effects in conical-ferromagnet/superconductor bilayers. *Phys. Rev. B*, 86:184517, Nov 2012.

[119] C. Bell, R. Loloee, G. Burnell, and M. G. Blamire. Characteristics of strong ferromagnetic Josephson junctions with epitaxial barriers. *Phys. Rev. B*, 71:180501, May 2005.

[120] J. W. A. Robinson, S. Piano, G. Burnell, C. Bell, and M. G. Blamire. Critical current oscillations in strong ferromagnetic π junctions. *Phys. Rev. Lett.*, 97:177003, Oct 2006.

[121] C. Bell, G. Burnell, D-J. Kang, R. H. Hadfield, M. J. Kappers, and M. G. Blamire. Fabrication of nanoscale heterostructure devices with a focused ion beam microscope. *Nanotechnology*, 14(6):630, 2003.

[122] C. H. Marrows and B. J. Hickey. New directions in spintronics. *Philosophical Transactions of the Royal Society A: Mathematical, Physical and Engineering Sciences*, 369(1948):3027–3036, 2011.

[123] J. W. A. Robinson, G. B. Halász, A. I. Buzdin, and M. G. Blamire. Enhanced supercurrents in Josephson junctions containing nonparallel ferromagnetic domains. *Phys. Rev. Lett.*, 104:207001, May 2010.

[124] E. A. Demler, G. B. Arnold, and M. R. Beasley. Superconducting proximity effects in magnetic metals. *Phys. Rev. B*, 55:15174–15182, Jun 1997.

[125] T. S. Khaire, M. A. Khasawneh, W. P. Pratt, and N. O. Birge. Observation of spin-triplet superconductivity in Co-based Josephson junctions. *Phys. Rev. Lett.*, 104:137002, Mar 2010.

[126] J. Linder, T. Yokoyama, A. Sudbø, and M. Eschrig. Pairing symmetry conversion by spin-active interfaces in magnetic normal-metal/superconductor junctions. *Phys. Rev. Lett.*, 102:107008, Mar 2009.

[127] M. Eschrig and T. Lofwander. Triplet supercurrents in clean and disordered half-metallic ferromagnets. *Nature Physics*, 4(2):138–143, 2008.

[128] M. Houzet and A. I. Buzdin. Theory of domain-wall superconductivity in superconductor/ferromagnet bilayers. *Phys. Rev. B*, 74:214507, Dec 2006.

[129] A. Yu. Aladyshkin, A. I. Buzdin, A. A. Fraerman, A. S. Mel'nikov, D. A. Ryzhov, and A. V. Sokolov. Domain-wall superconductivity in hybrid superconductor-ferromagnet structures. *Phys. Rev. B*, 68:184508, Nov 2003.

[130] A. I. Buzdin and A. S. Mel'nikov. Domain wall superconductivity in ferromagnetic superconductors. *Phys. Rev. B*, 67:020503, Jan 2003.

[131] M. G. Blamire, C. B. Smiet, N. Banerjee, and J. W. A. Robinson. Field modulation of the critical current in magnetic Josephson junctions. *Superconductor Science and Technology*, 26(5):055017, 2013.

[132] F. Chiodi, J. D. S. Witt, R. G. J. Smits, L. Qu, G. B. Halász, C.-T. Wu, O. T. Valls, K. Halterman, J. W. A. Robinson, and M. G. Blamire. Supra-oscillatory critical temperature dependence of nb-ho bilayers. *EPL (Europhysics Letters)*, 101(3):37002, 2013.

[133] J. D. S. Witt, J. W. A. Robinson, and M. G. Blamire. Josephson junctions incorporating a conical magnetic holmium interlayer. *Phys. Rev. B*, 85:184526, May 2012.

[134] J. P. Andrés, L. Chico, J. Colino, and J. M. Riveiro. Magnetic behavior of sputtered Gd/Co multilayers. *Phys. Rev. B*, 66:094424, Sep 2002.

[135] A. Razouk, M. Sahlaoui, and M. Sajieddine. Monte carlo study of magnetism of the Fe/Gd multilayers: Dependence on the layers thickness and interface morphology. *ISRN Nanotechnology*, 2012:736341, 2012.

[136] V. T. Petrashov, I. A. Sosnin, I. Cox, A. Parsons, and C. Troadec. Giant mutual proximity effects in ferromagnetic/superconducting nanostructures. *Phys. Rev. Lett.*, 83:3281–3284, Oct 1999.

[137] E. Schachinger, M. Prohammer, E. Seidl, and H. W. Weber. Anisotropy effects in the upper critical field of niobium: Theory and experiment. *Physica C Superconductivity*, 153:247–248, June 1988.

[138] N. Banerjee, C. B. Smiet, R. G. J. Smits, A. Ozaeta, F. S. Bergeret, M. G. Blamire, and J. W. A. Robinson. Evidence for spin selectivity of triplet pairs in superconducting spin valves. *Nature Communications*, 5, Jan 2014.

[139] G. Bochi, C. A. Ballentine, H. E. Inglefield, C. V. Thompson, R. C. O'Handley, H. J. Hug, B. Stiefel, A. Moser, and H.-J. Güntherodt. Perpendicular magnetic anisotropy, domains, and misfit strain in epitaxial ni/$cu_{1-x}ni_x$/cu/si (001) thin films. *Phys. Rev. B*, 52:7311–7321, Sep 1995.

[140] C. Hammond. *The Basics of Crystallography and Diffraction*. International Union of Crystallography texts on crystallography. OUP Oxford, 2009.

[141] B. D. Josephson. Coupled superconductors. *Rev. Mod. Phys.*, 36:216–220, Jan 1964.

[142] I. A. Campbell. Indirect exchange for rare earths in metals. *Journal of Physics F: Metal Physics*, 2(3):L47, 1972.

[143] S. D. Barrett and S. S. Dhesi. *The structure of rare-earth metal surfaces*. World Scientific, 2001.

[144] K. H. J. Buschow and F. R. Boer. *Physics of magnetism and magnetic materials*, volume 92. Springer, 2003.

[145] S. Oh, D. Youm, and M. R. Beasley. A superconductive magnetoresistive memory element using controlled exchange interaction. *Applied Physics Letters*, 71(16):2376–2378, 1997.

[146] J. W. A. Robinson. *Zero to π Oscillations in Superconductor - Ferromagnetic Junctions*. PhD thesis, University of Cambridge, 2007.

[147] B. Ackermann, R. Feder, and E. Tamura. Fully relativistic band structure of ferromagnetic Fe and Gd. *Journal of Physics F: Metal Physics*, 14(9):L173, 1984.

[148] J. R. Anderson, D. A. Papaconstantopoulos, L. L. Boyer, and J. E. Schirber. Spin-polarized band-structure calculations for Ni. *Phys. Rev. B*, 20:3172–3185, Oct 1979.

[149] T. B. Massalski and H. Okamoto. *Binary Alloy Phase Diagrams*. Number v. 1 in Ac-Ag to Ca-Zn. ASM International, 1990.

[150] Ya V. Fominov, A. A. Golubov, and M. Yu. Kupriyanov. Triplet proximity effect in FSF trilayers. *Journal of Experimental and Theoretical Physics Letters*, 77(9):510–515, 2003.

[151] A. Potenza and C. H. Marrows. Superconductor-ferromagnet CuNi/Nb/-CuNi trilayers as superconducting spin-valve core structures. *Physical Review B*, 71(18):180503, 2005.

[152] J. Linder, M. Zareyan, and A. Sudbø. Proximity effect in ferromagnet/superconductor hybrids: From diffusive to ballistic motion. *Physical Review B*, 79(6):064514, 2009.

[153] D. A. Ivanov and Y. V. Fominov. Minigap in superconductor-ferromagnet junctions with inhomogeneous magnetization. *Physical Review B*, 73(21):214524, 2006.

[154] B. Lv. Spin triplet Andreev reflection induced by interface spin-orbit coupling in half-metal/superconductor junctions. *The European Physical Journal B*, 83(4):493–497, Oct 2011.

[155] I. Margaris, V. Paltoglou, M. Alexandrakis, and N. Flytzanis. A diagrammatic approach to triplet supercurrents in ferromagnetic Josephson junctions. *The European Physical Journal B*, 88(6):145, Jun 2015.

[156] A. Bill, J. de Rojas, T. E. Baker, and A. Richie-Halford. Properties of magnetic-superconducting proximity systems. *Journal of Superconductivity and Novel Magnetism*, 25(7):2177–2182, Oct 2012.

[157] W. L. McMillan. Tunneling model of the superconducting proximity effect. *Physical Review*, 175(2):537, 1968.

[158] H. Homma, C. S. L. Chun, G-G. Zheng, and I. K. Schuller. Interaction of superconductivity and itinerant-electron magnetism: Critical fields of Ni/V superlattices. *Physical Review B*, 33(5):3562, 1986.

[159] L. Gor'kov and V. Kresin. Giant magnetic effects and oscillations in antiferromagnetic Josephson weak links. *Applied Physics Letters*, 78(23):3657–3659, 2001.

[160] M. Velez, M. C. Cyrille, S. Kim, J. L. Vicent, and I. K. Schuller. Enhancement of superconductivity by decreased magnetic spin-flip scattering: Nonmonotonic Tc dependence with enhanced magnetic ordering. *Physical Review B*, 59(22):14659, 1999.

[161] M. Eschrig, T. Löfwander, T. Champel, J. C. Cuevas, J. Kopu, and G. Schön. Symmetries of pairing correlations in superconductor–ferromagnet nanostructures. *Journal of Low Temperature Physics*, 147(3-4):457–476, 2007.

[162] J. Y. Gu, J. Kusnadi, and C-Y. You. Proximity effect in a superconductor/exchange-spring-magnet hybrid system. *Physical Review B*, 81(21):214435, 2010.

[163] C. Bell. *Nanoscale Josephson devices*. PhD thesis, University of Cambridge, 2003.

[164] J. A. Simpson, D. F. McMorrow, R. A. Cowley, and D. A. Jehan. The low-temperature magnetic structure of holmium. *Journal of magnetism and magnetic materials*, 140:751–752, 1995.

[165] M. J. Pechan and C. Stassis. Magnetic structure of holmium. *Journal of applied physics*, 55(6):1900–1902, 1984.

[166] I. A. Krivosheev, A. A. Nezhivoi, B. A. Nikol'skii, A. N. Ponomarev, V. N. Duginov, V. G. Ol'shevskii, and V. Yu Pomyakushin. Investigation of the magnetic structure of holmium by the muonic method. *Journal of Experimental and Theoretical Physics Letters*, 65(1):81–85, 1997.